Design of a 2-Phase Xenon Time Projection Chamber for Electron Drift Length Measurements

Johannes Schulz

Diplomarbeit

Institut für Kernphysik
Mathematisch-Naturwissenschaftliche Fakultät
Westfälische Wilhelms-Universität Münster

Dezember 2011

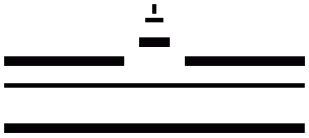

Referent: Prof. Dr. C. Weinheimer

Korreferent: Prof. Dr. J. Wessels

"Oohhh, dark matter. We better bring a flash light!"

— Rajesh Koothrappali, The Big Bang Theory

Contents

1 Introduction

One of the most fundamental questions in astrophysics today is the nature of dark matter (DM). Since evidences from astronomical observations give many hints to its existence, but just a few about its character, many predictions have been made and a broad variety of theories tries to explain what dark matter is. None of these theories have been verified because no convincing experimental detection of DM has been reported so far. Therefore, an increasing number of experiments focuses on DM search. Most of them are looking for a special candidate, the Weakly Interacting Massive Particle (WIMP), which is a well motivated candidate from a theoretical point of view.

One of these DM-experiments is the XENON Dark Matter Project operating a detector called XENON100. This detector is searching WIMPs by looking for nuclear recoil signals in a 2-phase Time Projection Chamber (TPC) containing about 60 kg of liquid xenon. The combination of xenon's properties as a detector material and the TPC concept, which provides some unique detector features, has allowed XENON100 to become the most sensitive experiment to the WIMP-nucleon cross section.

The next generation DM detector, XENON1T, will contain xenon on the ton scale. Xenon purity, which is already a technical challenge for the XENON100 experiment, will become much more critical for a larger detector volume. Therefore, the requirements on purity are extremely high since purity is mandatory to operate such a big detector volume. The contribution of Münster's XENON group to the XENON1T operation is the construction of a gas system including a purification unit, and the design of a krypton distillation column.

Both devices have to be monitored during the R&D phase. For this task, a small dual phase TPC that is integrated in Münster's xenon purification system has been designed, constructed, assembled and tested in the context of this thesis.

The results of these processes are presented after a general introduction to dark matter with evidences and candidates, an illustration of the most popular experiments in this field including their results, and details about xenon as a detector material combined with the TPC-technique.

2

Dark Matter

In the 1930s, there were the first signs for a different mass distribution in the universe than astronomers believed before. By observing the motion of galaxies in the Coma cluster, Fritz Zwicky calculated their masses and compared them to the ones calculated by the number and the brightness of the galaxies [Zwi37]. He found out that the motion based calculation gives about 400 times more mass than the calculation due to the visible galaxies. With this result, he inferred some optically non observable matter, called "dark matter", which provides the mass needed to explain the motion of galaxies near the cluster edges.

2.1. Evidences for Dark Matter

After Zwicky's discovery, many other indications for a missing mass in the universe were found by astronomical observations. The most important ones: rotation curves of galaxies, gravitational lensing, and the findings from exploring the cosmic microwave background are illustrated in the following sections.

2.1.1. Rotation Curves of Galaxies

With the improvement of spectrograph technology, observations similar to Zwicky's with much higher resolution were possible. It allows measurements of the rotational curves of spiral galaxies, where the orbital velocity of stars is measured as a function of their distance from the galactic center. The major part of luminous matter is focused in the center of the galaxy and stars in the outer spiral arms should move around this center like the planets around the sun. Therefore, a Keplerian-like orbital velocity of

$$v(r) \sim \frac{1}{\sqrt{r}} \tag{2.1}$$

would be expected at least for large radii r. In fact, the velocities do not show such behavior but stay nearly constant even far away from the center as shown in figure 2.1. The constant rotation velocities lead to the conclusion that most of the matter, in fact more than 95%, has to be in the galactic halo. This is not consistent with the classic

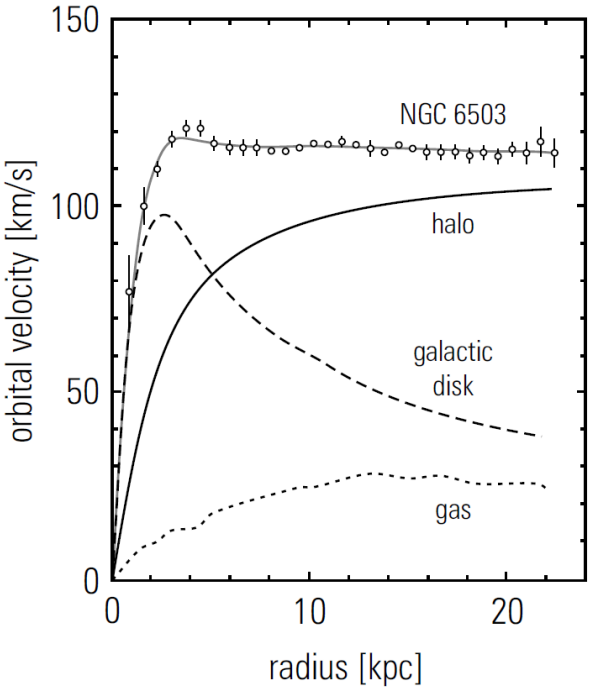

Figure 2.1.: *Rotational curves of the spiral galaxy NGC 6503. The observed velocity values are fitted with a mass contribution (gray line) made up by the galactic disk, the gas, and the halo. Figure taken from [Gru05].*

astronomical knowledge from observations of visible matter and it agrees with Zwicky's postulation of a new, invisible kind of matter.

2.1.2. Gravitational Lensing

In addition to the analysis of galaxy rotations, there is another observed phenomenon indicating dark matter existence: gravitational lensing. As predicted by Albert Einstein in his General Theory of Relativity, light is deflected under the influence of gravitational fields. This has been observed in so called gravitational lenses. A gravitational lens is in principle a collection of massive objects in the universe, where a great amount of matter lays between a luminous object like a galaxy and the observer. Light emitted under such angle that it would not reach the observer in case of geometric optics, is bent around the massive object in between and appears visible for the observer. The observer is able to see a so called Einstein ring which consists of multiple images of the light source appearing on a ring around the massive object. Figure 2.2 shows the principle of gravitational lensing in a two dimensional plain.

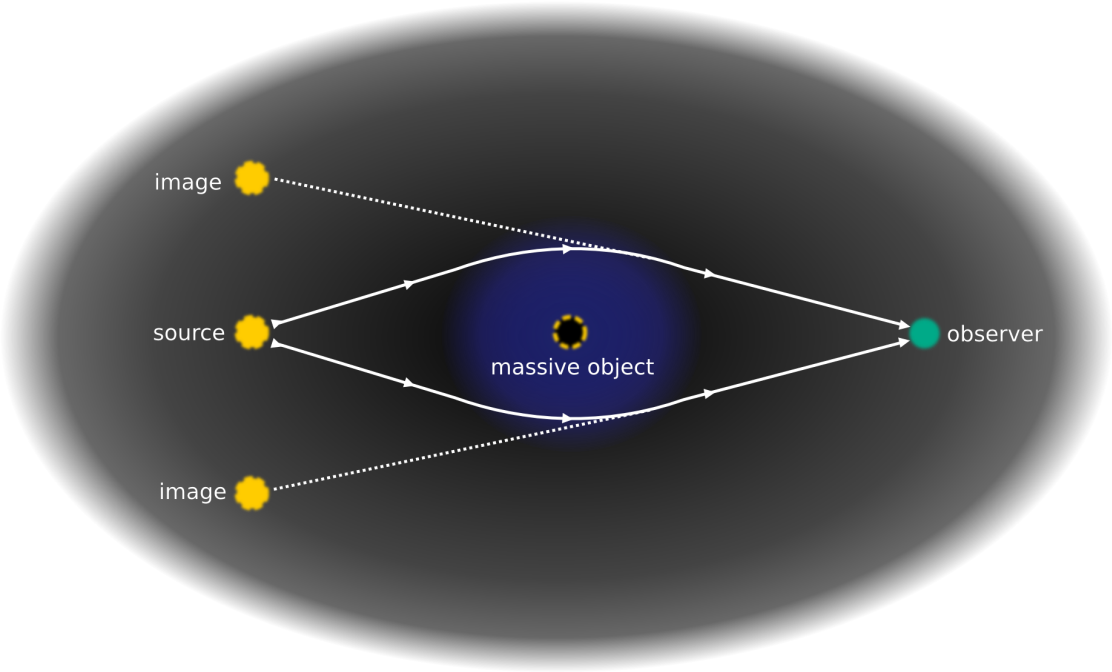

Figure 2.2.: *In this basic sketch the principle of gravitational lensing is shown. Light from a source that lies behind a massive object is deflected and reaches the observer, who will see several images of the source under different angles as an Einstein ring.*

By rotating the sketch around its horizontal axis, the images would form an Einstein ring. If the massive object is a galaxy cluster, it is possible to calculate the mass of the cluster out of the bending of the light. In parallel, the mass of the luminous matter in the cluster can be calculated out of x-ray measurements. The comparison of the determined masses shows that the values are not identical. This is a strong indication for the existence of dark matter.

A related and even stronger hint is the so called "Bullet cluster". The Bullet cluster is a system of two single galaxy clusters which collided about 150 million years ago. The collision affected the constituent parts differently when the galaxies moved through each other. The stars and planets interacted just gravitationally crossing each other nearly unaffected. The diffuse hot gas, which should be the main part of the matter in classical models, interacts electromagnetically causing the molecules to slow down more and to fall behind the stars and planets. In this case, the above mentioned gravitational lensing measurements for the mass distributions show the following: The main part of mass is in the region of the stars and planets, see green curvature in figure 2.3. The hot

gas, shown by the color-coded areas on the right panel, is clearly (with $8\,\sigma$) displaced between the two mass centers [Clo06]. This is classically not understandable, but it can be explained with the presence of dark matter. The dark matter interacts like stars and planets only gravitationally giving no obvious reason why the collision should have a big effect on it. One would expect the main part of the matter still in the region of the stars. This explanation suits well the observations. This is the reason why the bullet cluster gives a strong evidence for dark matter existence. Additionally, it should be mentioned that the bullet cluster is no special case. Other cluster collisions with the same characteristics in mass distribution have also been observed.

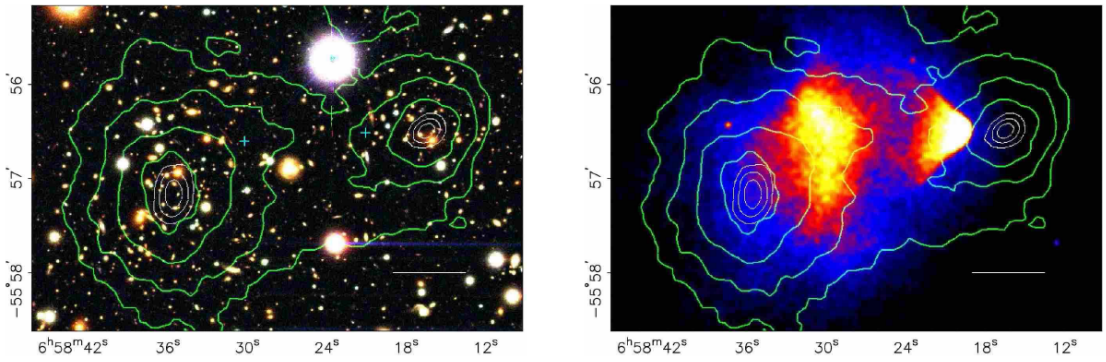

Figure 2.3.: *Shown in the left panel is a color image from the Magellan images of the merging cluster 1E0657558, with the white bar indicating 200 kpc at the distance of the cluster. In the right panel is a 500 ks Chandra image of the cluster. Shown in green contours in both panels are the weak gravitational lensing κ reconstruction with the outer contour level at $\kappa = 0.16$ and increasing in steps of 0.07. The white contours show the errors on the positions of the κ peaks and correspond to 68.3 %, 95.5 %, and 99.7 % confidence levels. The blue +s show the location of the centers used to measure the masses of the plasma clouds. Figure and caption taken from [Clo06].*

2.1.3. Cosmic Microwave Background

All these evidences lead to the fact that the existence of dark matter is well established today. Most of the astronomers and astroparticle physicists believe that our universe contains by far more dark than luminous matter and the Wilkinson Microwave Anisotropy Probe (WMAP) gave the proof by measuring the cosmic microwave background (CMB). The cosmic microwave background is background radiation consisting of photons from the early universe, which is almost perfectly isotropic. The spectral distribution is the

most accurate blackbody spectrum ever measured and it gives a body temperature of 2.73 K. The origin of this radiation can be explained with one stage in the development of the universe. In the early universe, the energy density and the temperature were very high. Hence, all atoms were ionized. The plasma was so dense that light could not propagate because it was absorbed immediately. With the expansion of the universe, it cooled down and the ionized atoms recombined. The photons then decoupled from the atoms propagating freely through the transparent universe and continue to do so today. The relic photons were redshifted by the expansion of the universe and they are measurable with microwave wavelength today.
With a precise measurement of the CMB, it is possible to see small fluctuations in the radiation of different directions. These fluctuations contain a lot of information about the matter density distribution and therefore the energy density at the point of time when light propagation became possible.
Analyzing these temperature and polarization fluctuations in terms of multipole components leads to a power spectrum. In figure 2.4, the seven-year WMAP temperature power spectrum is shown together with data from ACBAR[1] and QUaD[2]. From this, the total matter density and the baryonic matter density can be determined by a fitting procedure and under the assumption of certain cosmological models, for details see [Kom11]. The analysis of the seven year WMAP data from cosmic microwave background observations gives values for the content of the universe. The actual calculated values are: $(4.5 \pm 0.3)\%$ baryonic matter, $(22.2 \pm 2.6)\%$ dark matter, and $(73.0 \pm 2.9)\%$ dark energy [Jar11], see also figure 2.5. The dark matter density is calculated as the difference between the total matter component and the baryonic matter component. Therefore, the remarkable statement of **non-baryonic** dark matter can be made.

2.2. Dark Matter Candidates

There is a variety of dark matter candidates postulated by theorists and it is up to the experimental physicists to test the models by trying to detect dark matter and explore its nature. The experiment, this thesis is contributing to, is looking for one of these dark matter candidates, the Weakly Interacting Massive Particle (WIMP). In the following section, the WIMP and the connected theoretical model called Supersymmetry will be briefly presented.

[1] Arcminute Cosmology Bolometer Array Receiver
[2] Q and U Extragalactic Sub-mm Telescope at the Degree Angular Scale Interferometer

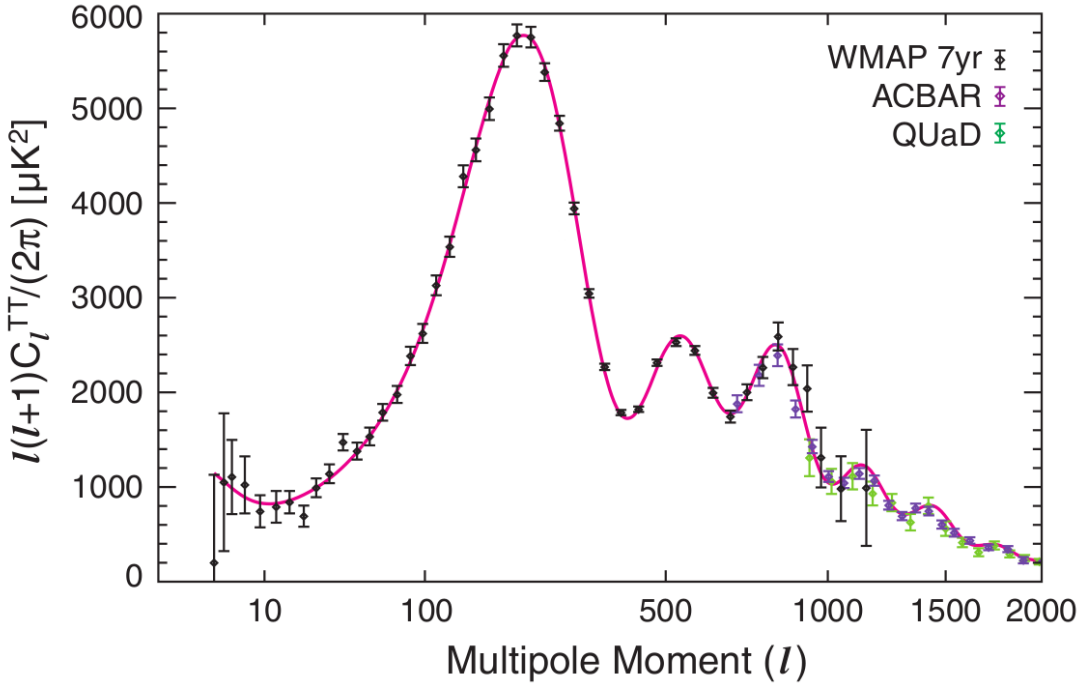

Figure 2.4.: *WMAP seven-year temperature power spectrum, together with data from ACBAR[1] and QUaD[2]. The red line shows the fit for WMAP data concerning a flat Lambda-Cold Dark Matter (ΛCDM)-model. Figure taken from [Kom11].*

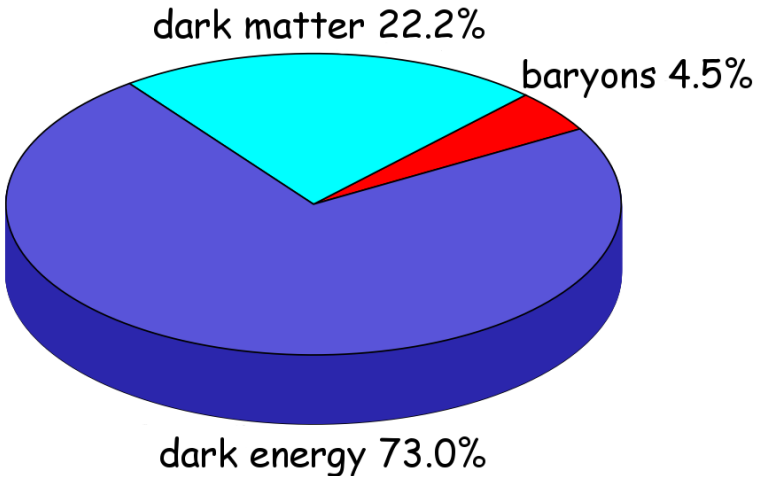

Figure 2.5.: *WMAP results showing the energy content of the universe. The actual values are* $(4.5 \pm 0.3)\%$ *baryonic matter,* $(22.2 \pm 2.6)\%$ *dark matter, and* $(73.0 \pm 2.9)\%$ *dark energy [Jar11].*

2.2.1. Supersymmetry

The Standard Model (SM) of particle physics is a well established theory with great success describing the electromagnetic, weak, and strong nuclear interactions. Nevertheless, there are phenomena which cannot be described properly with the SM. The concepts of dark matter and dark energy predicted by cosmologists cannot be described concerning the SM. The same accounts for a neutrino mass different from zero, found by investigating the neutrino oscillation. Not only observations point to physics beyond the SM, but also theorists are unsatisfied with a few theoretical issues. One problem is for example that the Higgs boson is expected to be much lighter than the Planck mass. This is called the hierarchy problem and it requires a lot of fine tuning in parameters to explain it within the SM. Another example is the unrealized unification of all forces at high energies which is tried to be achieved by formulating new theories where an extension of the SM is needed.
There are several interpretations of these and many other aspects which are in conflict with the SM. One of the most common is that the SM is a special case of a more fundamental theory just valid for low energies. One candidate for this fundamental theory is Supersymmetry (SUSY) [Ber04].
The basic idea of SUSY is to add a supersymmetric partner to every particle in the Standard Model. Bosons would have a supersymmetric fermion partner and fermions a supersymmetric boson partner. In the case of an exact symmetry, all quantum numbers except for the spin would be the same for a pair of SUSY partners, including mass. Because of the fact that no supersymmetric particle has been detected in colliders, SUSY must be a broken symmetry to allow SUSY particles to have a higher mass. A broken SUSY provides naturally the frame for the broken weak symmetry. To realize that an additional Higgs field is introduced for a total of two Higgs doublets [Eds97]. All SM particles and their supersymmetric partners are shown in table 2.1. In case of SUSY, one can define an additive quantum number: R-parity. It is +1 for each particle and -1 for each SUSY partner and it is a conserved quantity. This is the reason why the decay of the lightest supersymmertric particle (LSP) into standard particles is not possible. It is a likely dark matter candidate because it remains stable on a cosmological timescale.

2.2.2. The WIMP

With the new particles introduced by SUSY, many potential candidates for the LSP are proposed. Following the arguments of Ellis et al. [Ell83] the neutralino is the best dark

Table 2.1.: *Particles of the supersymmetric standard model. Table taken from [Ber04].*

Standard Model particles and fields		Supersymmetric partners			
		Interaction eigenstates		Mass eigenstates	
Symbol	Name	Symbol	Name	Symbol	Name
$q = d, c, b, u, s, t$	quark	$\tilde{q}_L$, $\tilde{q}_R$	squark	$\tilde{q}_1$, $\tilde{q}_2$	squark
$l = e, \mu, \tau$	lepton	$\tilde{l}_L$, $\tilde{l}_R$	slepton	$\tilde{l}_1$, $\tilde{l}_2$	slepton
$\nu = \nu_e, \nu_\mu, \nu_\tau$	neutrino	$\tilde{\nu}$	sneutrino	$\tilde{\nu}$	sneutrino
g	gluon	$\tilde{g}$	gluino	$\tilde{g}$	gluino
$W^\pm$	W-boson	$\tilde{W}^\pm$	wino	$\tilde{\chi}^\pm_{1,2}$	chargino
H^-	Higgs boson	$\tilde{H}^-_1$	higgsino		
H^+	Higgs boson	$\tilde{H}^+_2$	higgsino		
B	B-field	$\tilde{B}$	bino	$\tilde{\chi}^0_{1,2,3,4}$	neutralino
W^3	W^3-field	$\tilde{W}^3$	wino		
H^0_1	Higgs boson	$\tilde{H}^0_1$	higgsino		
H^0_2	Higgs boson	$\tilde{H}^0_2$	higgsino		
H^0_3	Higgs boson				

matter candidate among these particles. As shown in table 2.1, the neutralino is a linear combination of two higgsinos and two superpartners of gauge fields, the bino and the wino. Further it is assumed that the neutralino is a majorana particle, so it is its own antiparticle, and it is weak-scale interacting, which gives the name WIMP. With these assumptions, today's dark matter distribution can be explained in the following way:
In the early universe when the temperature of the universe was higher than the mass of the heaviest particle, all particles of the SUSY standard model were coexisting in thermal equilibrium. With the expansion and therefore cooling of the universe, there was not enough energy to produce the heavy supersymmetric particle-antiparticle pairs any more and the remaining ones decayed cascading down to the lightest supersymmetric particle (LSP). On the other hand, the density of particles became smaller and smaller with the expansion of the universe. The particles did not find each other anymore and the annihilation process stopped with some WIMPs remaining. The amount of remaining WIMPs depends on the cross section of the annihilation, which is schematically shown in Figure 2.6, for a more detailed overview see [Jun96]. Due to their weak scale interaction, WIMPs can be directly detected by scattering on a nucleus of ordinary matter. In addition to that, there are indirect detection techniques trying to observe signals from dark matter annihilation. The topic of indirect searches will not be further presented in this thesis. Instead, the focus is on direct detection techniques.

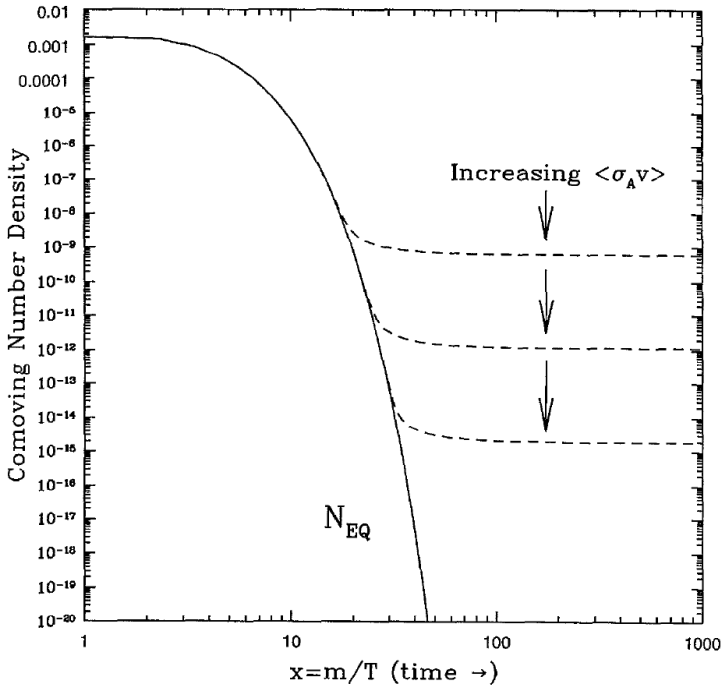

Figure 2.6.: *Shown here is the comoving density of WIMPs in the early universe. The dashed lines are actual abundances for different annihilation cross sections (arrows indicate increasing cross sections) and the solid line is the abundance in equilibrium. Figure taken from [Kol89]*

2.3. Experiments for Dark Matter Search

The WIMP hypotheses explained in section 2.2.2 is the most promising theory in today's dark matter research community. Therefore, a lot of experiments try to test the theory and characterize the particles by direct detection. All of them are located in underground laboratories to minimize the cosmic ray background. The basic principle of operation is the detection of interactions between WIMPs and detector material.

2.3.1. Interaction Rate

A wimp can interact with a target nucleus in two ways. In the spin dependent interactions, a WIMP is spin coupling to a nucleus. In the spin independent interaction, it couples coherently to the nucleus. As a linear combination of superpartners to SM bosons, the WIMP has a spin 1/2 and is therefore a fermion. The coupling, as it occurs in nature, is still under investigation.

The general differential interaction rate can be calculated from

$$\frac{dR}{dQ} = \frac{2\rho_0}{m_\chi} \int_{v_{min}}^{v_{esc}} \frac{d\sigma}{dq^2} v f(v) dv, \tag{2.2}$$

where $Q = q^2/2m_N$ is the recoil energy with q as the norm of the momentum transfer, m_N is the nucleus' mass, $\rho_0 = 0.3\,\mathrm{GeV/cm^3}$ is the central value of the dark matter density in the local halo, and m_χ is the WIMP mass. Furthermore, $v_{min} = (m_N Q/2{m_r}^2)^{1/2}$ is the minimal WIMP velocity necessary to create a nuclear recoil with energy Q, m_r is the reduced mass of the WIMP nucleus system, $v_{esc} = 544\,\mathrm{km/s}$ is the velocity a WIMP needs to escape the Milky Way, v is the speed and $f(v)$ the speed distribution of the WIMPs, and $\frac{d\sigma}{dq^2}$ is the differential cross section [Bro10]. As mentioned above, the interaction of a WIMP may depend on the spin and therefore different cross sections would be the consequence. In this thesis, just the spin independent coupling and interaction rate will be discussed in more detail.
For the coherent scattering of a WIMP and a nucleus ,the differential cross section can be written as

$$\frac{d\sigma}{dq^2} = \frac{\sigma_0}{4m_r^2 v^2} F^2(Q), \tag{2.3}$$

where σ_0 is the nuclear scattering cross section at zero momentum transfer and $F^2(Q)$ is the nuclear form factor. In the common literature, the Helm form factor

$$F(Q) = \frac{3j_1(qR_1)}{qR_1} e^{-qs} \tag{2.4}$$

is used [Hel56],[Lew96], where $q = \sqrt{2Qm_N}$, $R_1 = \sqrt{R^2 - 5s^2}$, $R = 1.2A^{1/3}\,\mathrm{fm}$ with the atomic mass number A, $s = 1\,\mathrm{fm}$, and $j_1(x)$ is a spherical Bessel function,

$$j_1(x) = \frac{sinx}{x^2} - \frac{cosx}{x}. \tag{2.5}$$

For further calculations, it is necessary to choose a speed distribution, normally a Maxwellian one [Bro10]. This gives with respect to the relative motion of the earth to the Dark Matter distribution v_e and the escape velocity for WIMPs v_{esc}:

$$\begin{aligned} \int_{v_{min}}^{v_{esc}} \frac{f(v)}{v} dv = \frac{2}{v_0\sqrt{\pi}} \frac{k_0}{k1} \times \\ \left[\frac{\sqrt{\pi} v_0}{4v_e} \left(\mathrm{erf}\left(\frac{v_{min} + v_e}{v_0} \right) - \mathrm{erf}\left(\frac{v_{min} - v_e}{v_0} \right) \right) - \exp\left(-\frac{v_{esc}^2}{v_0^2} \right) \right]. \end{aligned} \tag{2.6}$$

$v_0 = 220\,\mathrm{km/s}$ is here the velocity of the sun around the center of the Milky Way and

$$\mathrm{erf}(a) = \frac{2}{\sqrt{\pi}} \int_0^a e^{-b^2} db \tag{2.7}$$

is the Gaussian error function. From [Lew96], the following formula for k_1 is taken

$$k_1 = k_0 \left[\mathrm{erf}\left(\frac{v_{esc}}{v_0}\right) - \frac{2v_{esc}}{\sqrt{\pi} v_0} \exp\left(-\frac{v_{esc}^2}{v_0^2}\right)\right] \quad \text{with} \quad k_0 = (\pi v_0^2)^{3/2}. \tag{2.8}$$

If it is assumed that the WIMP coupling to proton and to neutron is the same for coherent scattering, the cross section can be written as function of the proton cross section

$$\sigma_0 = Z^2 \left(\frac{m_r}{m_p}\right)^2 \sigma_p + (A-Z)^2 \left(\frac{m_r}{m_n}\right)^2 \sigma_n \approx A^2 \left(\frac{m_r}{m_p}\right)^2 \sigma_p, \tag{2.9}$$

where Z is the atomic number, A is the atomic mass number, and m_p and m_n are the masses of proton and neutron. Finally, the differential cross section rate for spin independent interactions can be calculated from

$$\begin{aligned} \frac{dR}{dQ} = \frac{\sigma_p \rho_0 A^2}{\sqrt{\pi} v_0 m_\chi m_p^2} F^2(Q) \frac{k_0}{k_1} \times \\ \left[\frac{\sqrt{\pi} v_0}{4 v_e} \left(\mathrm{erf}\left(\frac{v_{min} + v_e}{v_0}\right) - \mathrm{erf}\left(\frac{v_{min} - v_e}{v_0}\right)\right) - \exp\left(-\frac{v_{esc}^2}{v_0^2}\right)\right]. \end{aligned} \tag{2.10}$$

With formula 2.10, it is now possible to determine the differential interaction rates for various detector materials. In figure 2.7 this is shown for four common detector materials xenon, germanium, argon, and silicon, where the WIMP mass is assumed to be $m_\chi = 100\,\mathrm{GeV}$ scattering with a cross section of $\sigma_p = 10^{-44}\,\mathrm{cm}^2$. Summing up, it becomes clear that heavy target nuclei are operating at a high rate for low energy recoils, whereas the form factor suppression leads to a low sensitivity for high recoil energies. For light detector materials, the situation is vice versa, therefore the detector material for dark matter search should be chosen carefully.

2.3.2. Detection Technologies

The signals produced by the interactions depend on the detector material: thermal excitation, scintillation light, and ionization are commonly used. In figure 2.8, it is

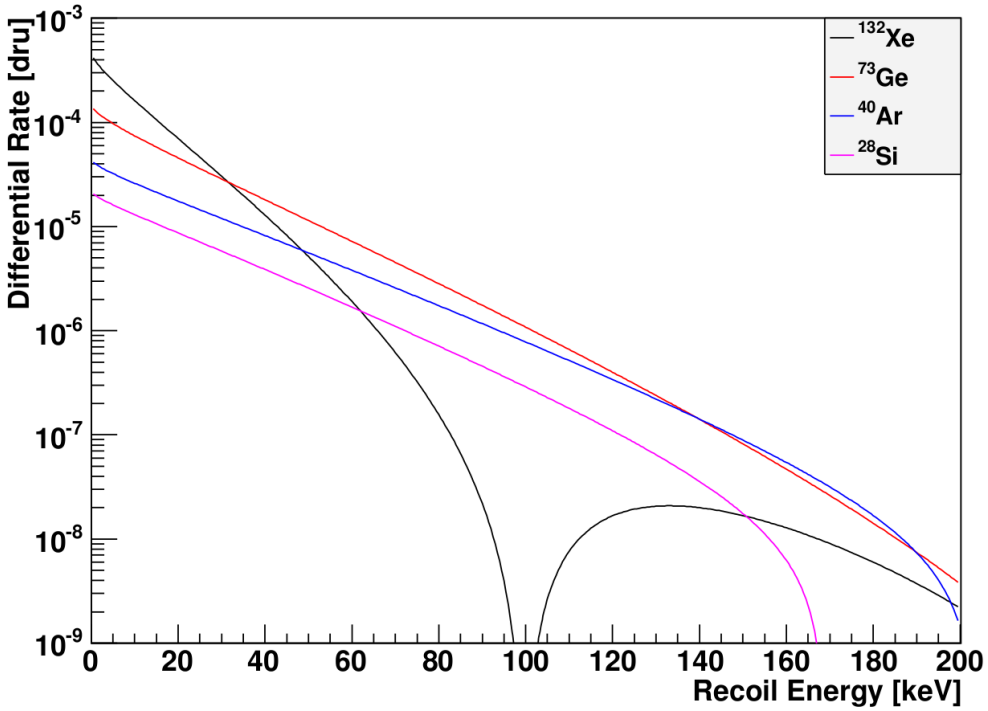

Figure 2.7.: *Spin independent differential scattering rate for WIMPs with a mass of* 100 GeV *and a cross section of* $10^{-44}\,\mathrm{cm}^2$ *as function of the recoil energy for different detector materials. Clearly visible is the drop caused by the form factor suppression on heavy targets like xenon. Figure taken from [Bro10].*

shown which of the well-known experiments is sensitive to what kind of interaction signal. Most of them are looking for two of the three signals to distinguish between WIMP and background events.
One experiment of each group will be introduced briefly in this section.

The DAMA/LIBRA Experiment

The group of experiments DAMA/LIBRA belongs to is just sensitive to one interaction signal, the scintillation light. The DAMA/LIBRA experiment is located at the Gran Sasso National Laboratory in Italy and uses about 250 kg of highly radiopure NaI(Tl) crystals as a detector material. They have 25 crystal scintillators arranged in a 5×5 matrix, each connected to two low background photomultiplier tubes (PMTs). The crystals and the PMTs are housed in a ultra-high purity copper box, which is surrounded by many layers of different shielding material for background reduction. For further

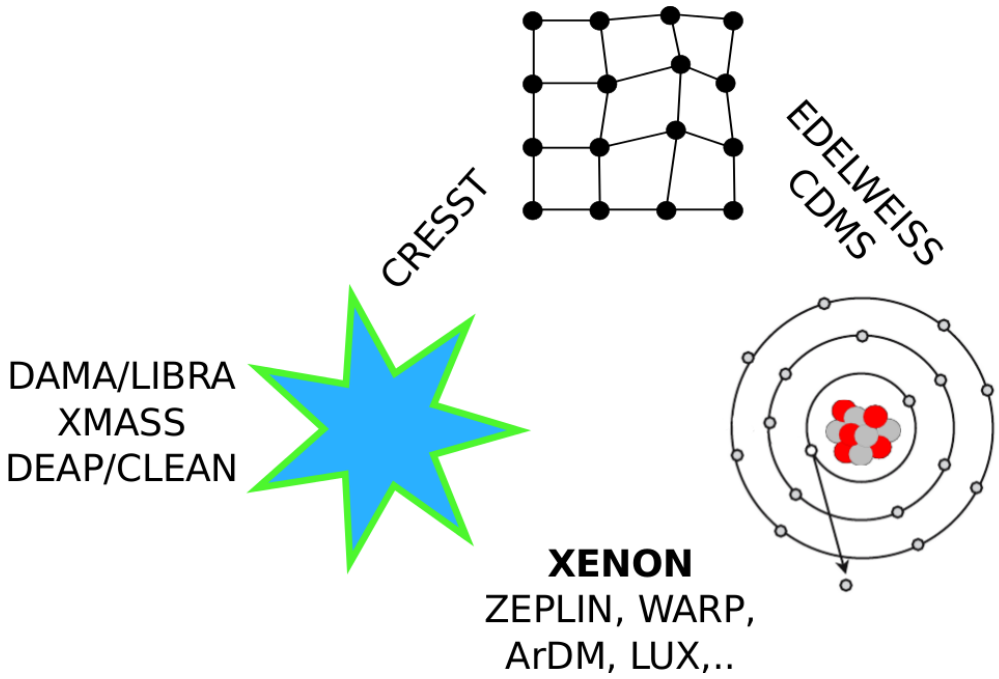

Figure 2.8.: *In this schema, the most popular Dark Matter experiments are shown sorted by their detection principle. The three symbols stand for thermal excitation (top), ionization (right), and scintillation (left). Experiments listed between two symbols use these two techniques (e.g. XENON). Experiments listed one side of a symbol are just sensitive to these kind of detection mechanism (e.g. DAMA/LIBRA).*

background rejection, two coincidence conditions are required. First, all events are dismissed where just one PMT of the two connected to a crystal sees a signal because these are most likely noise events. Second, all events where more than one crystal reports a signal (multi-hits) are rejected because the WIMPs are not expected to interact twice in such a small volume. An event is recorded when both PMTs of one single crystal see a signal (single-events) [Ber08].

The DAMA/LIBRA collaboration collected data with an exposure of 1.17 ton $\times$ year and claimed to see dark matter by observing an annual modulation of the detected signals with 8.9 σ C.L., shown in figure 2.9. They interpret their results in the context of the so called dark matter wind. The earth is moving around the sun, while the sun is moving around the center of the Milky Way, so the dark matter wind should blow more intensely when sun and earth are moving in the same direction, see equation 2.6. That would lead to an annual modulation on top of a basic signal. The interpretation that the annual modulation observed by DAMA/LIBRA is due to dark matter is highly

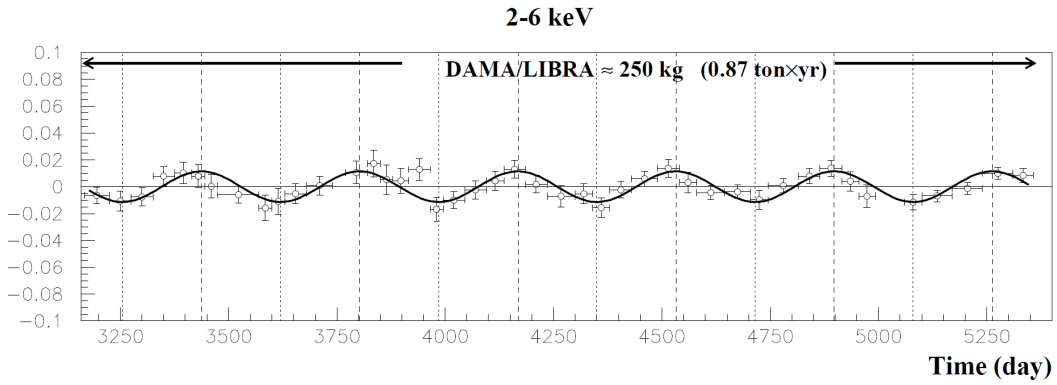

Figure 2.9.: *Residual rate of single-event scintillation signals measured by DAMA/LIBRA. The dashed vertical lines show the expected time of maximal event rate, the dotted lines show the expected time of minimal event rate due to dark matter. Figure taken from [Ber10].*

controversial. The critics argue that it is not possible to find out which particle was involved in the interactions DAMA/LIBRA detected, so the modulation could be due to some background. In the mean time, the areas in the phase space for WIMP-nucleon cross section and the WIMP mass predicted by DAMA/LIBRA have been ruled out by the results of many other experiments, such as XENON100 and the CDMS-Experiment, see figure 2.10 at the end of the section.

The Cryogenic Rare Event Search with Superconducting Thermometers (CRESST-II) Experiment

The CRESST-II Experiment, which is also located at the Gran Sasso National Laboratory, differs in design to DAMA/LIBRA in a way that it should be able to distinguish different kinds of particles interacting in the detector. Eight detector modules of $CaWO_4$ crystals are operated with a two channel read out. As shown in figure 2.8, one channel is for phonon signals caused by lattice excitations, the other one is for light signals produced by scintillation light. With these two signal types, it is possible to distinguish between WIMP and background events in the following way. The measurement of the lattice excitation gives a very precise value of the energy deposition in the detector. Since the ratio of scintillation light to energy deposition depends on the kind of interaction, event-by-event background discrimination becomes possible.

For lattice excitation measurements, a very sensitive transition edge sensor (TES) is

used. A TES consists of a small amount of superconducting material, cooled down just below the critical temperature (µK) where the resistance varies strongly with temperature T. If then phonons couple to material, the temperature will increase above the critical temperature leading to a clearly measurable change in resistance. In addition to that, a small amount of the energy deposit in the crystal is converted into scintillation light, which is separately detected by silicon-sapphire light absorbers combined with a second TES. The single detector modules are housed in reflecting foil and shielded from background mainly with copper, lead, and polyethylene layers complemented with a muon veto [Ang11].
The CRESST-II experiment operated with an exposure of 730 kg × day and observed 67 events in their accepted recoil energy region where just $29.4^{+8.6}_{-7.7}$ background events had been expected. This gives a significance larger than $4\,\sigma$ that the detected events are not due to the expected background [Ang11]. But this is similar to the DAMA/LIBRA results, since the published areas in the phase space diagram are ruled out by other experiments, which makes the critics again suggest that the signal comes from an unknown background.

The Cryogenic Dark Matter Search Experiment (CDMS II)

The CDMS II experiment located in Soudan Underground Laboratory (2090 m.w.e.)[3] belongs to a different group of experiments, also searching dark matter by observing two signal channels. It is not feasible to detect scintillation light, but it can detect the ionization induced by a WIMP-nucleus recoil, and as CRESST, it is sensitive to lattice excitation. The ionization is detected by drifting the charges in an electric field carefully through the crystal to the surface, where they are collected. The event-by-event background reduction is even better than in CRESST because in addition to the discrimination by the ratio of ionization energy to phonon energy, a fiducial volume is defined. This is done by the rise time of the phonon signal which gives information about the distance from the event position to the surface. By defining a region of interest inside the crystals, surface events due to background can be discriminated.
The actual setup consists of 19 germanium and 11 silicon detectors stacked in five towers cooled down to 50 mK. Around the detector, there is a passive lead and polyethylene shielding and a muon veto. For Dark Matter search, only the 19 germanium detectors are used combined with the silicon ones to veto multiple detector hits. With an expo-

[3] m.w.e.: meter water equivalent for cosmic ray shielding purposes

sure of 612 kg × day, two possible dark matter events were detected by the CDMS II experiment, which are still consistent with an expected background of (0.9 ± 0.2) events [Ahm10]. Therefore, the result excludes the parameter space associated with possible low-mass WIMP signals from the DAMA/LIBRA experiment. Furthermore, most of the parameter space region given by the CoGeNT experiment can be excluded, see figure 2.10. In addition, it confirms the cross section limits set by the XENON100 experiment in 2010.

The XENON100 Experiment

The third way of combining the detection channels is the combination of ionization and scintillation. One of the experiments operating a detector that is sensitive to these two signals, is the XENON Dark Matter Project. It is located at the Gran Sasso National Laboratory as well as CRESST and DAMA. In contrast to the discussed experiments above, it uses no solid detector material for the dark matter detection, but liquid xenon. WIMPs interacting with the xenon atoms produce scintillation light and ionization products, which can be collected separately. This is done in a detector called XENON100 which is a dual phase Time Projection Chamber (TPC). The properties of xenon as a detector material, the functional principle of a 2-phase TPC, and the results of the XENON dark matter search are presented in the following chapter.
With anticipation of the XENON results, the discussion of the actual knowledge about dark matter interactions can be concluded before the detailed discussion of XENON research. As shown in figure 2.10, XENON100 is currently the most sensitive experiment to the spin independent WIMP-nucleon cross section. It excludes nearly all regions of claimed dark matter detections by DAMA/LIBRA and CoGeNT as well as a fair part of the theoretically favored parameter space predicted for WIMPS by Trotta et al. [Tro08] and Buchmueller et al. [Buc11].

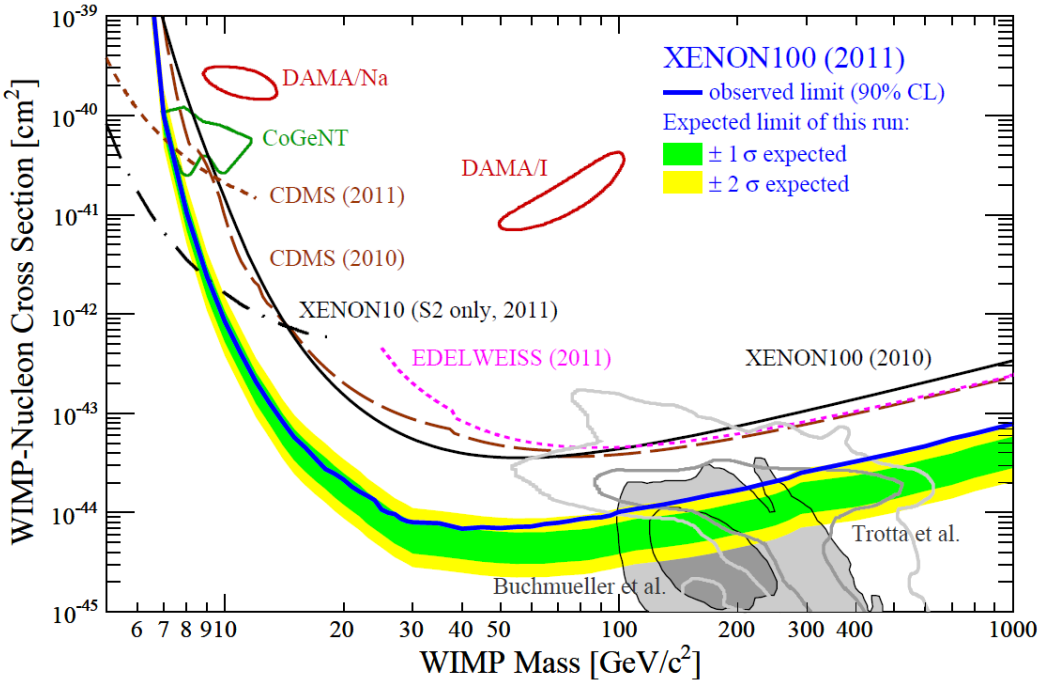

Figure 2.10.: *Phase space diagram of WIMP-nucleon spin independent scattering with theoretical predictions (gray areas), as well as exclusion curves from current DM experiments (90 % C.L.). For the XENON100 experiment, the green and yellow bands indicate the expected sensitivity for the run without background signals. The area above the curves, or outside the closed contours is excluded by the respective experiment. Remarkable is the challenging situation between DAMA/LIBRA and CoGeNT claiming DM detection on the one hand and CDMSII and XENON100 excluding the claimed phase space on the other hand. Figure taken from [Apr11].*

3

The XENON Dark Matter Project

In the current phase of the project, the XENON Dark Matter Collaboration operates the XENON100 detector, which is at the moment leading in case of sensitivity to dark matter recoils as shown in figure 2.10. XENON100 is the successor of the XENON10 detector which was the first experiment that used a dual phase xenon Time Projection Chamber (TPC) for dark matter search. Because of strong constraints on the WIMP cross section given by XENON10 as published in 2007, it was decided to build a detector containing about a factor of ten more xenon to gain sensitivity. The same is going to happen for the XENON100 detector, when it reaches its limits of sensitivity. The next stage of the XENON Dark Matter Project is already planed and will be assembled soon. It is a one ton liquid xenon detector called XENON1T, which will be capable to investigate the phase space of the WIMP-nucleon cross section more than one order of magnitude below the actual limits.

The TPC detector technique will be explained in detail in this section. The properties of xenon as a detector material for dark matter search are presented before hand to convey the physical background.

3.1. Properties of Liquid Xenon Related to Dark Matter Search

The properties of liquid xenon (LXe) meet several demands for a dark matter detector medium because of its large mass number. The expected rates for low energy recoils have been already calculated in section 2.3.1. The other main aspects which are high gamma cross sections, easy handling, low radioactivity, and two channel readout are summarized in the following.

3.1.1. Density and Self-Shielding

The high atomic number of 54 and a liquid density of about $3\,\mathrm{g/cm^3}$ provide good self-shielding properties for γ-radiation. Known from the Beer-Lambert law, the intensity

I_γ of γ-radiation penetrating a material decreases with the depth of penetration l like

$$I_\gamma(l) = I_{\gamma,0} \exp\left(-\left(\frac{\mu}{\rho}\right) \cdot \rho\, l\right), \tag{3.1}$$

where $I_{\gamma,0}$ is the original intensity, ρ is the density of the material and (μ/ρ) is the mass attenuation coefficient. This coefficient (μ/ρ) depends on the energy of the γ-ray as shown in figure 3.1. For low energetic γ-rays, a LXe target is self-shielding because they do not penetrate deeply into the volume. This characteristic is used in background reduction as it is explained in section 3.2.4.

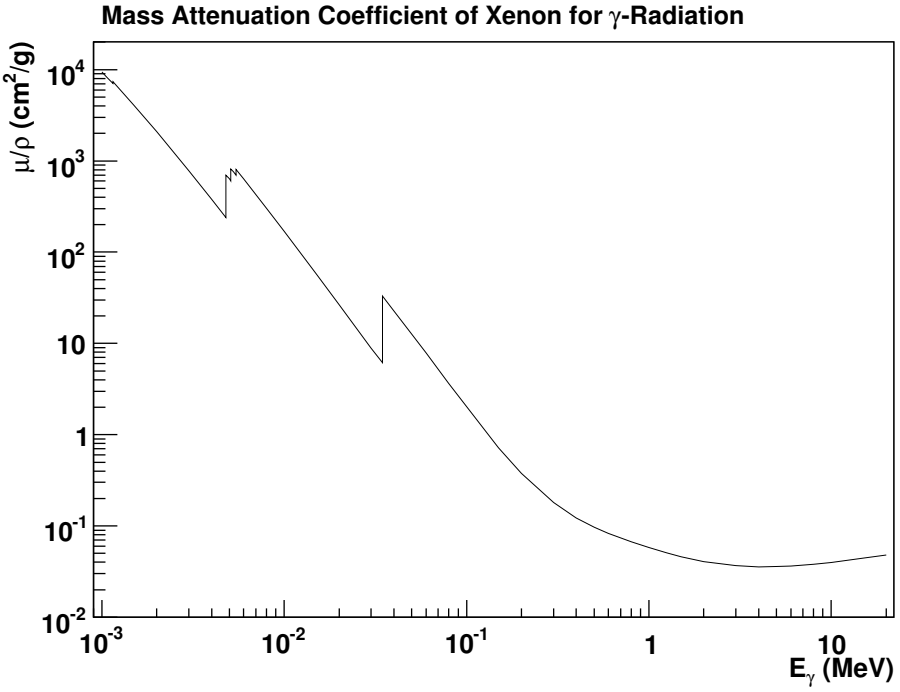

Figure 3.1.: *Mass attenuation coefficient of gammas in LXe as function of their energies. Low energetic gammas are absorbed shortly after the surface of a target volume. Data taken from [NIST].*

3.1.2. Handling

For the save and stable operation of a detector containing an amount of liquid noble gas in the 10 - 100 kg range or even on the tons scale, the cryogenics have to be considered. In case of xenon, the demands on the cryogenic system are technically unproblematic

because under a pressure of 2 bar it gets liquid at 177.88 K, which is easy reachable by conventional cryocoolers. The temperature range to operate the detector is then about 16.5 K, down to 161.4 K, where the xenon starts to freeze out. With a lower pressure of about 1 bar, the melting point is almost the same, but the boiling point is at 164.82 K [NIST]. A higher pressure leads to an even higher liquefaction temperature, but also stresses the detector hardware, especially the PMTs. A good compromise is the operation around 2 bar.
These pressure and temperature requirements are much easier to handle than the ones for a cryogenic bolometer working at mK temperatures.

3.1.3. Radioactivity

Xenon can be made extremely radiopure because all of the naturally existing isotopes listed below are stable. The Isotopes ^{124}Xe, ^{134}Xe, and ^{136}Xe are candidates for double β-decay, but none of these decays has been observed so far. Natural xenon is composed of roughly half even and half odd isotopes, which allows the detection of spin dependent and spin independent interactions as discussed in section 2.3.1 and can be used to determine the character of the interaction by measuring only with even or odd isotopes. A bigger

Table 3.1.: *Xenon isotopes and their natural abundance. Data taken from from [Apr09].*

^{124}Xe (0.09%)	^{126}Xe (0.09%)	^{128}Xe (1.92%)	^{129}Xe (26.44%)	^{130}Xe (4.08%)
^{131}Xe (21.18%)	^{132}Xe (26.89%)	^{134}Xe (10.44%)	^{136}Xe (8.87%)	

problem are contaminations with radioactive isotopes of other elements such as ^{85}Kr as well as ^{222}Rn and its decay products. Especially the ^{85}Kr is problematic because it undergoes a β-decay with a half life of 10.756 years and an end point energy of 687.4 keV [NDS91]. Therefore, it has to be actively removed because of its long half life time. In commercially available ultra pure xenon, the amount of krypton is in the order of a few parts per billion (ppb), whereas the ratio of ^{85}Kr/Kr is about 10^{-11}. Nevertheless, it is necessary to remove the Krypton content to a lower level in the order of parts per trillion (ppt) for dark matter search. Otherwise the ^{85}Kr decays would limit the maximal sensitivity of the detector by causing background events.
The removal itself can be done by a cryogenic fractionating column, where xenon and krypton get separated. Like in a normal distillation process the two elements can be separated in a distillation tower due to their different boiling points.

3.1.4. Two Channel Read Out

When exposed to radiation, xenon gives scintillation light and ionization. By observing the light and the charge signal, it becomes possible to determine the energy and the type of the particle as well as location and time of the interaction. This feature is unique for liquid xenon and liquid argon compared to other noble liquids [Apr09] and offers therefore two detection channels as already outlined in figure 2.8.

Scintillation Process

The scintillation light has its origin in an excited dimer Xe_2^*, which can be produced in two different processes by radiation. One involves exited xenon atoms Xe^* (eq. 3.2), the other one has xenon ions Xe^+ as an initial condition (eq. 3.3). According to [Apr09] and [Kub78], the processes can be explained by the following reaction equations.
In one case, directly exited xenon atoms are producing just scintillation light,

$$\begin{aligned} Xe^* + Xe &\rightarrow Xe_2^* \\ Xe_2^* &\rightarrow 2Xe + h\nu \end{aligned} \tag{3.2}$$

while in the other, primary ionized xenon atoms undergo a multi-stage reaction

$$\begin{aligned} Xe^+ + Xe &\rightarrow Xe_2^+ \\ Xe_2^+ + e^- &\rightarrow Xe^{**} + Xe \\ Xe^{**} &\rightarrow Xe^* + heat \\ Xe^* + Xe &\rightarrow Xe_2^* \\ Xe_2^* &\rightarrow 2Xe + h\nu \end{aligned} \tag{3.3}$$

where heat is produced as well.
Due to the fact that the scintillation light is emitted by an excited dimer, the other xenon atoms do not absorb the light and it can propagate through the liquid. The wavelength of the emitted photons is about 178 nm, which is directly detectable by UV sensitive photomultiplier tubes (see chapter 6) arranged around the target.

Ionization Process

The ionization of xenon atoms is not only the start point of one scintillation light production as mentioned in equation 3.3, but also the origin of the charge signal.
The energy deposition of radiation is distributed to ionization and excitation of xenon atoms supplemented by free electrons getting sub-excitation level kinetic energy. Concerning these three processes, the average of the required energy to produce one electron-ion pair (W-value) in liquid xenon is W= (15.6 ± 0.3) eV [Tak75]. Compared to the one of liquid argon, which is W= (23.6 ± 0.3) eV [Tak75], it is significantly smaller giving a much larger ionization yield.
In the presence of an electric field, recombination of the ionization products is suppressed. The electrons are separated from the ions and drift along the field lines. A signal from this electron cloud can be collected and analyzed as it will be explained in section 3.2.2.

With the combined read out of the scintillation and the ionization signal a very efficient background discrimination becomes possible because the ratio of energy deposited in scintillation and energy deposited in ionization depends on the kind of radiation (see section 3.2.4).

3.2. Time Projection Chamber

An established tool to detect the scintillation and the ionization signals is a dual phase xenon Time Projection Chamber.

3.2.1. Basic Design of a TPC

The typical TPC design for liquid xenon dark matter detectors consists of a cylindrical volume covered with polytetrafluoroethylene (PTFE) due to its high reflectivity for 178 nm light. The top and bottom of the volume are equipped with PMT arrays for scintillation light detection. The liquid xenon (LXe) is filled up to a certain level below the top PMTs and the gap is filled with xenon gas. To collect ionization products, an electric field is applied in two stages: one from just over the bottom PMTs to right below the xenon surface, which is the drift field; the other one directly continues up to slightly above the surface, which is the extraction field. With this simplified TPC model, the working principle is explained in the following. A much more detailed description of the

components and specific design aspects is discussed in chapter 4 using the example of the TPC built in context of this thesis.

3.2.2. Working Principle of a TPC

Figure 3.2 shows the basic working principle of the dual phase TPC.

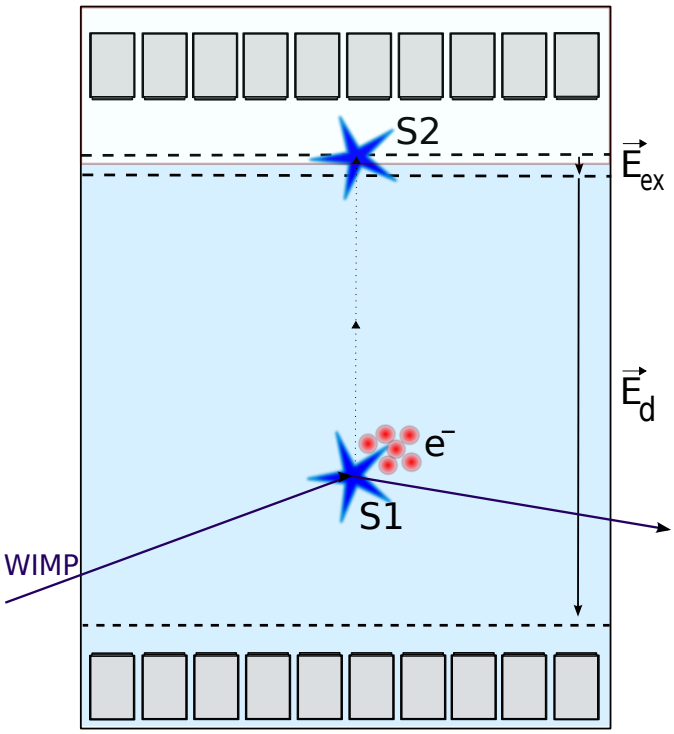

Figure 3.2.: *Scheme of the TPC working principle. WIMPs hitting Xe-atoms produce electrons and scintillation light (S_1) in the liquid. The electrons are forced by an electric field ($\vec{E}_d$) to drift towards the surface, where they are extracted and accelerated causing scintillation light (S_2) in the gas by the extraction field ($\vec{E}_{ex}$). The scintillation signals can be detected by arrays of PMTs at the bottom and top of the TPC. The signals of the top PMTs give the x- and y-coordinate of the recoil event, the time between the first and the second light pulse gives the z-coordinate allowing a 3D localization of the interaction.*

Incoming particles hit Xe-atoms producing prompt scintillation light (S_1) and charges in the liquid as discussed in 3.1.4. The S_1 signal is mostly collected by the bottom PMTs due to total internal reflection ($n_{UV} = 1.67$) at the liquid surface. The free electrons are drifted by the electric drift field $\vec{E}_d$ of about 1 kV/cm towards the surface. The

electrons are extracted and accelerated by the much higher extraction field $\vec{E}_{ex}$ of more than 10 kV/cm causing proportional scintillation light in the gas (S_2). The fraction of electrons extracted depends on the field strength for lower fields and saturates above 10 kV/cm as shown in figure 3.3 [Apr09]. The S_2 signals appear very close to the top PMT array, which is of fundamental importance for the event position reconstruction as shown in the following.

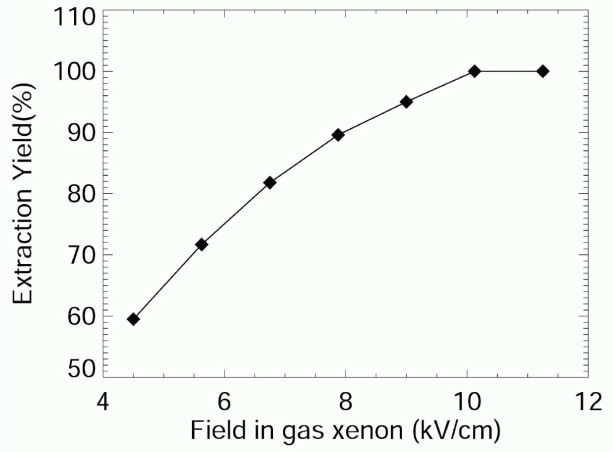

Figure 3.3.: *Electron extraction yield from liquid to gaseous xenon plotted versus the electric field strength. Above a field strength of 10 kV, all electrons are extracted from the liquid phase. Figure taken from [Apr09].*

3.2.3. 3D Position Reconstruction

The knowledge of the event position is of substantial importance for background reduction, as it will be shown in section 3.2.4. The three dimensional reconstruction of the interaction place is one feature of a TPC and can be divided into two parts. One part is the determination of the position in the (x,y)-plane, the other is the determination of the z-position along the detector axis.

The x-,y-coordinates can be calculated out of the S_2 signal pattern on the PMT array on top of the detector. Usually, algorithms trained by simulation data are used for this task obtaining a position resolution of a few millimeter. The reconstruction of the z-position is much easier because it only requires a precise measurement of the time between the peaks of the S_1 and S_2 signals. In a constant electric field of 1 kV/cm, the electrons drift with about 2 mm/µs [Apr09]. The z-position of the interaction is then the drift velocity times the drift time and has a resolution of a few millimeter as well.

3.2.4. Background Discrimination

A dual phase TPC offers two different possibilities of background discrimination which are combined for the use as dark matter detector. First, the excellent self-shielding properties of LXe are used to define a fiducial volume in the center of the detector. Events outside this active area are supposed to be surface background and can be rejected. The size of the fiducial volume can be determined by calibration measurements. In the second step, detected signals in the fiducial volume are analyzed in more detail to determine the origin of the interaction process. This method makes use of the difference in the ratio of the two scintillation signals for nuclear and electron recoils. Electron recoils initiated by gammas show a much higher ratio than nuclear recoils produced by WIMP scattering leading to $(S_2/S_1)_\gamma \gg (S_2/S_1)_{\mathrm{WIMP}}$. In addition, the energy deposited in the detector by nuclear recoils can be used as an supplemental criterion. Interactions releasing too much energy can be rejected because WIMPs should just deposit a small amount of energy in the detector. Very small signals have to be rejected as well because they cannot be distinguished from electronic noise. Therefore, an energy window has to be chosen. For XENON100, it is for example (8.4 - 44.6) keV [Apr11].

3.3. XENON100

As mentioned in the introduction of this chapter and to complete the presentation of the experiment technologies from section 2.3.2, the XENON100 detector is presented briefly in the following.

As it is incumbent for a dark matter experiment, XENON100 is installed underground in the Gran Sasso National Laboratory to reduce background caused by cosmic rays. For further passive background suppression, different layers of highly pure copper, polyethylene, lead, and water are installed around the actual detector. To avoid the infiltration of gaseous radioactive isotope into the detector surrounding, all gaps between the shielding and the detector vessel are flown with pure nitrogen to suppress radon decays to a rate lower than $1\,\mathrm{Bq/m^3}$.

Inside these barriers, the XENON100 dual phase TPC is mounted. It has a diameter and a height of 30 cm containing a total target mass of 62 kg LXe. Surrounding the inner target, 99 kg LXe are used as an active scintillator veto monitored by PMTs and optically separated from the inner volume by PTFE reflectors which is visible on figure 3.4. It is seen in figure 3.5 that not all of the target mass is defined as region of interest,

but only the innermost 48 kg are fiducial target. Monitored with 178 high quantum efficiency UV PMTs (see section 6), 98 in the top, 80 in the bottom array, a position reconstruction with 2 -3 mm accuracy in each direction is possible. The active veto is equipped with 64 additional PMTs, see figure 3.4.

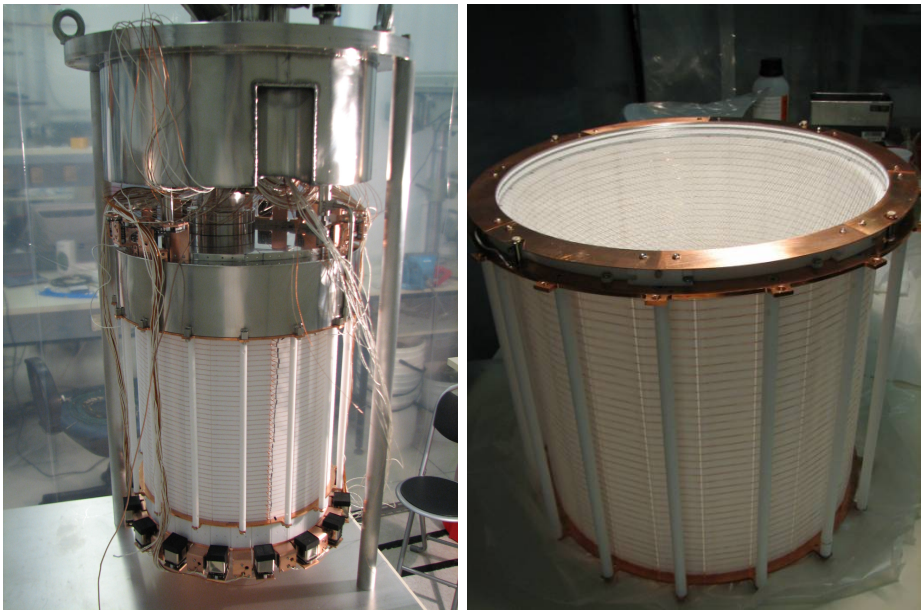

Figure 3.4.: *On the left-hand picture, the hole XENON100 detector setup is shown as it is inside the vacuum cryostat. The white structure is the PTFE reflector surrounding the actual TPC. Visible as well are the veto PMTs covered with black protector caps at the bottom. On the right-hand picture, a close-up of the single reflection and field case is shown. Barely visible are the meshes on top of the drift chamber.*

The presently published data on XENON dark matter search was acquired in the first half of 2010. It gives the todays most stringent limits on dark matter interactions. In figure 3.5, the distribution of all events (gray dots) in the XENON100 TPC during 100.9 days of life time is shown. The black dots mark events within the accepted energy range for nuclear recoils, the blue line indicates the edge of the fiducial volume. Clearly visible is the concentration of nuclear recoils due to the background radiation at the surface of the detector. After the application of all cuts, three possible WIMP candidates are left (red dots), which are in agreement with a background expectation of (1.8 ± 0.6) events. In conclusion, there is no dark matter found and another part of the phase space of WIMP-nucleon spin independent scattering can be excluded (see figure 2.10). In addition, all

experiments claiming to see dark matter signals can be challenged with the new limits on WIMP-nucleon cross sections [Apr11].

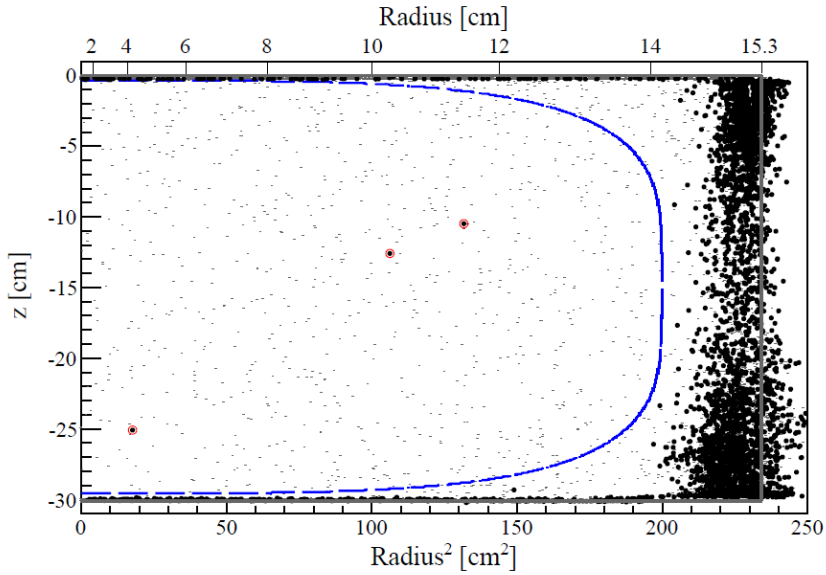

Figure 3.5.: *Distribution of all events (gray dots) recorded during XENON100 run8 with 100.9 days of life time. The black dots mark events within the accepted energy range for nuclear recoils. Three events (red dots) are not rejected by the fiducial cut, which is indicated by the blue line. This number is comparable with the expected relict background of* (1.8 ± 0.6) events. *Figure taken from [Apr11].*

3.4. XENON1T

At a certain point, the maximal sensitivity of XENON100 will be reached. The detector was designed for a sensitivity to WIMP-nucleon cross sections down to $2 \times 10^{-45}\,\mathrm{cm}^2$ for $100\,\mathrm{GeV/c}^2$ WIMP masses. At lower cross sections, the XENON100 detector is dominated by backgrounds and a bigger volume is necessary to reach even higher sensitivities. The XENON Dark Matter Project will continue the research with a next generation detector operating on the ton-scale, called XENON1T.

XENON1T is designed to operate with a total target mass of 2.4 tons and a TPC with one meter diameter and one meter height. Similar to XENON100, only a fraction of one ton LXe will be used as fiducial mass and a 400 kg active veto will be installed. With an exposure of 1 ton $\times$ year and a factor 100 background reduction compared to XENON100,

a sensitivity to spin independent cross sections of $5 \times 10^{-47}\,\mathrm{cm}^2$ for $100\,\mathrm{GeV/c}^2$ WIMPs is expected [Apr10].
To operate XENON1T, drift lengths of about a meter are required making high demands on purification.

3.5. Purity of Liquid Xenon

A main aspect of this thesis' motivation is to deal with the subjects of electron drift length and xenon purification for XENON1T. The purity of xenon plays a key role for TPC operation and has to be controlled at all times. Every time the vacuum is broken, impurities are remaining on the surfaces after pumping down the vessel. While filling in xenon, they outgas mixing into the xenon, and it is necessary to clean it. Not just at the beginning of a new duty cycle, but also during operation, impurities are attaining permanently to the liquid. Outgassing from the liquid containment and all other materials inside the cryostat contributes to the level of foreign particles. A minimization of the initial as well as removal of the diffusing impurities can be done by a continuous cleaning process outside the detector.
The main problem are electronegative molecules capturing free electrons. As described in section 3.2.2, the charges are drifted in an electric field causing a delayed scintillation signal after extraction. In order to drift small ionization signals over a distance of one meter, as it is necessary for XENON1T, the amount of electronegative impurities has to be very low as shown by Aprile and Doke in [Apr09]. Otherwise, the electrons would react with these impurities S forming negative ions which are not mobile any more.

$$e^- + S \rightarrow S^- \tag{3.4}$$

This charge accretion has an influence on the electron concentration $\langle e \rangle$ given by

$$\frac{d\langle e \rangle}{dt} = k_s \langle e \rangle \langle S \rangle, \tag{3.5}$$

where $\langle S \rangle$ is the impurity concentration in mol/l and k_s the attachment rate constant in l/(mol s), which depends on the field and the kind of impurity and is related to the attachment cross section. By solving the differential equation, one finds

$$\langle e(t) \rangle = e(0) \exp(-k_s \langle S \rangle t) \tag{3.6}$$

for the time dependent electron concentration and

$$\tau = (k_s \langle S \rangle)^{-1} \tag{3.7}$$

as the so called electron life time. With knowledge of the electron drift velocity v_d, it is possible to calculate the attenuation length in LXe:

$$\lambda_{att} = v_d \tau \tag{3.8}$$

As already mentioned, k_s depends on the field strength. In LXe, the typical electronegative impurities can be classified by their k_s correlated or anti-correlated with the electric field strength E. In figure 3.6, the electron attachment rate constants for three different impurities (SF_6, N_2O, and O_2) as a function of the drift field strength are shown.

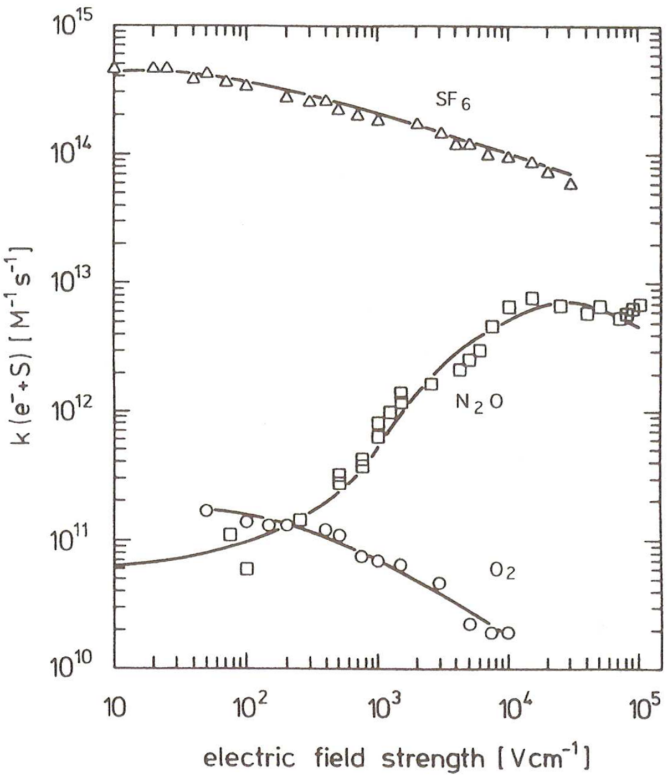

Figure 3.6.: *Electron attachment rate constants in LXe (T=165K) for different impurities (SF_6, N_2O and O_2) as a function of the electric field strength. Figure taken from [Bak76].*

SF_6 and O_2 have a k_s anti-correlated with E, whereas the k_s for N_2O shows a correlated behavior. Usually, the composition of impurities is not expected to be known in detail, therefore the concentrations are expressed in equivalent oxygen.
Considering the formulas in section 3.2.2 and 3.5 and the figures 3.6 and 3.7, a rough example estimation can be made to find the attenuation length at a certain purity level. A SAES PS4-MT50 heated getter, as used in Münster's XENON lab, has an outlet amount of <1 ppb O_2 for noble gases, which is of the order of $\langle S \rangle = 2.2 \times 10^{-8}$ mol/l for LXe. The normal design value for the drift field strength in a TPC is around 1 kV/cm leading to a drift velocity of about $2{\times}10^5$ cm/s as shown in figure 3.7.

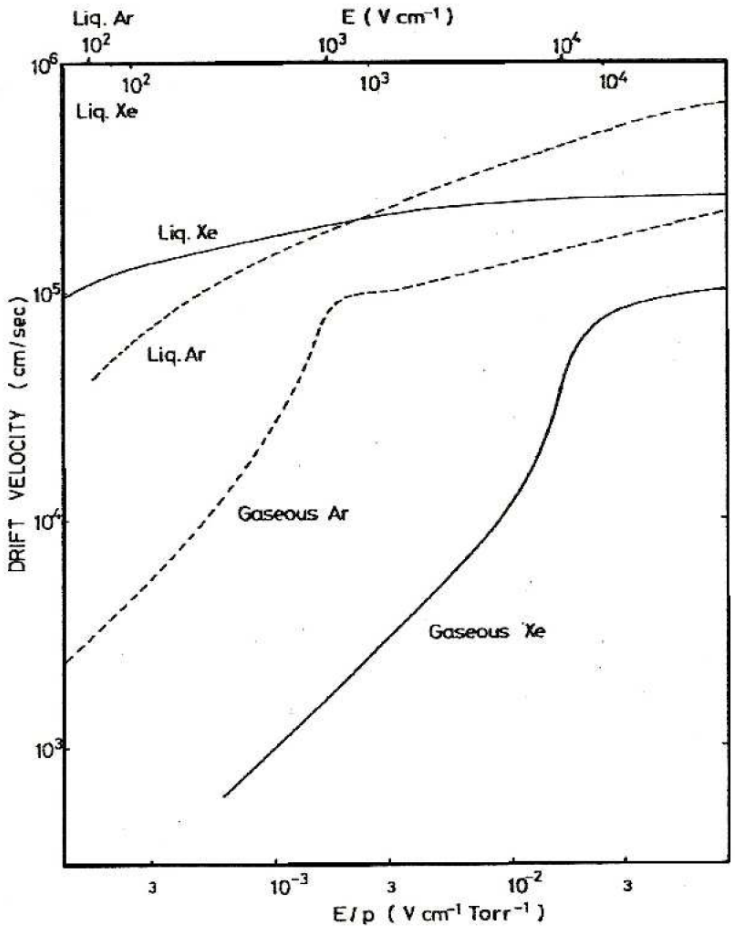

Figure 3.7.: *Electron drift velocity in Xe and Ar (both gaseous and liquid) as a function of the electric field strength on the top x-axis, and as a function of the electric field divided by the pressure on the bottom x-axis. Figure taken from [Apr09].*

A value for $k_s = 5 \times 10^{10}\,(\mathrm{M\ s})^{-1} = 5 \times 10^{10}\,\mathrm{l/(mol\ s)}$ can be obtained from figure 3.6 for O_2. The attenuation length is then

$$\lambda_{att} = \frac{2 \times 10^3\,\mathrm{m/s}}{5 \times 10^{10}\,\mathrm{l/(mol\ s)} \cdot 2.2 \times 10^{-8}\,\mathrm{mol/l}} = 2\,\mathrm{m}.$$

In addition to that, it is possible to calculate the ratio of electron concentrations before and after a drift of 1 m at this purity level like

$$\frac{\langle e(1m)\rangle}{\langle e(0m)\rangle} = \exp\left(-\frac{5 \times 10^{10}\,\mathrm{l/(mol\ s)} \cdot 2.2 \times 10^{-8}\,\mathrm{mol/l} \cdot 1\,\mathrm{m}}{2 \times 10^3\,\mathrm{m/s}}\right) = 0.58\,.$$

Only 58% of the electrons produced in an interaction at the bottom of the XENON1T TPC would actually reach the surface. Therefore, the level of impurities should be significantly smaller than 1 ppb oxygen equivalent to increase this ratio.

The measurement of contaminations in the xenon on sub-ppb level is not trivial which makes the calculation of λ_{att} difficult. There is a different, more elegant possibility to determine the electron life time and the drift length and that is by drifting the electrons and measuring the attenuation.
In a TPC, the drift time (dt) of an electron can be detected with high resolution. With calibration data, it is possible to ascertain the electron drift life time. Therefore, the values of the S_2 signals are plotted depending on their drift time. Using an exponential function for the fit, it gives the time dependent electron concentration and the electron drift life time, which is directly linked to the position dependent electron concentration by the drift velocity.
This method offers the possibility to determine the attenuation length in the detector on the fly and allows its measurement without xenon extraction. In addition, a small TPC can be utilized to demonstrate the performance of long drifts and is very useful as a monitoring tool in the context of LXe purification research and development.

4

The Münster Time Projection Chamber

In the context of this thesis, a small TPC was designed and built in Münster. One of the main requests was to construct a device to monitor the purity of xenon by electron drift length measurements in Münster's XENON lab. The purification will be performed by a SAES PS4-MT50 heated getter using a zirconium alloy for impurity filtering. Combining getter and TPC will result in a powerful test stand for purity related R&D. Another important demand on the system is to enable the quantification of krypton removal efficiency achieved with a distillation column. The basic procedure is to enrich xenon with a well known amount of ^{83m}Kr and measure its activity before and after passing the column. The ratio of activities gives then information of the reduction efficiency of krypton in general, which is essential for further developments on the column.
These two points, development of a gas system including a purification cycle and construction of a krypton removing distillation column, are the main contributions of Münster's XENON group to the XENON1T project.
A side aspect for the TPC design was to build a detector which is able to reconstruct the interaction position in three dimensions. To monitor purity and krypton removal efficiencies, a device with just z-position sensitivity would be sufficient, but with a basic structure, similar to the one in XENON1T, a much broader variety of R&D becomes possible at a small detector setup. In addition to that, a fully developed TPC is a powerful tool for other applications, such as medical imaging.
The main aspects of designing, constructing, and assembling of the Münster TPC are presented in the following.

4.1. Basic Design

Two basic parameters were fixed at the beginning of the design process. The first is a minimal drift length of 100 mm, which is desired to perform attenuation length measurements over a certain distance. The second is the number of one-square-inch PMTs,

which was set to 14 total. By using two times seven PMTs arranged in a 2 - 3 - 2 array, good circular surface coverage can be achieved. Additionally, an analogous design to XENON100 and XENON1T was favored to profit from already developed technologies and to be able to project research results back onto the experiment. All further design steps are consistent with these basics.

The level of radioactivity introduced to the system played a key role for the material selection. Since the Münster TPC will be used as a testbed for XENON1T components, all parts were selected with the same low radioactivity requirements. In addition to that, the number of different materials was kept as low as possible. Therefore, the TPC consists of three main materials which are stainless steel, PTFE (Teflon) and copper. Some parts of the electric installation are made of different materials because of commercial availability reasons, but they were chosen in the context of low radioactivity and high purity as well.
Another aspect of crucial importance for the selection of parts and materials was purity. In case of the liquid containment, leaks are the dominant topic which gives high demands on tightness of the TPC housing. Basically, the constraints are the same as for ultra high vacuum (UHV) systems. To achieve an extremely low leak rate of $< 1 \times 10^{-10}$ mbar l/s, it was decided to use ConFlat (CF) vacuum components for the vessel. As an industrial standard, not every arbitrary size of these parts exist. The available element, which suits the given demands best, is a stainless steel tube of 150 mm diameter and 334 mm length with a CF160 flange on both ends. Considering the problems regarding impurities, it was decided to use stainless steel type 316L due to its higher surface quality and lower outgassing rates. This is the default and all major steel parts installed in the cryostat are made of 316 or 316L type steels.

A 334 mm long housing tube gives enough space to perform significantly longer drifts than required. Therefore, a drift length of 150 - 170 mm was used in the ongoing design studies of the inner TPC structure. The inner diameter of the PTFE reflector, which marks the edge of the LXe volume, was initialized to 80 mm allowing first active mass estimations. Using 170 mm as its height and 80 mm as its diameter, the TPC would contain about 2.56 kg liquid xenon.
All these aspects led to a good basic orientation making further design steps possible starting with the electric field, which is the central aspect of the whole design process.

4.2. Electric Field Design

The electric field, maintained between steel meshes, is similar to the one in a parallel plate capacitor. It is homogeneous in the central region, but at the edges the field lines are bent and have to be formed if straight drifts are required. An approved technique to shape the field is placing annular electrodes between the two planes around the cylindrical drift volume. Each ring is on a different potential maintained by a resistor chain. The distances between the rings are constant and therefore the voltage differences as well. An overview of the field cage components as well as of the simulations made to find the optimal arrangement of these parts is given in the following.

4.2.1. Initial Layout

As a consequence of the high purity demands and due to their commercial availability, ConFlat copper gaskets have been a good option as electrode material. These rings are made out of oxygen free high conductivity copper (OFHC) for the use in UHV setups. The smallest gaskets in the CF production line with at least 80 mm inner diameter are the CF100 rings. They have an inner diameter of 101.8 mm, an outer diameter of 120.5 mm, and a thickness of 2 mm. Aspects of PMT surface coverage do not allow a 100 mm diameter TPC, which requires a spacer inside the rings. In addition to purity, there are two further requirements to the material of this brace. First, it should have a very similar dielectric constant to LXe ($\epsilon_r = 1.88$ [CRC06]) to avoid discontinuities in the equipotential lines of the field. Second, a high reflectivity for the scintillation light of xenon at 178 nm is desirable. The best candidate is PTFE with $\epsilon_r = 2.1$ [CRC06] and a high reflectivity. PTFE can be produced with high purity and fulfills all material requirements for the spacing. As additional advantage, a spacer covers the walls without gaps and copper surfaces since it is made out of a single cylinder. There is also a more homogeneous drift field in the LXe because field inhomogeneities appear next to the rings and are abated mainly inside the spacer. Furthermore, Teflon has a dielectric strength of about 20 kV/mm [CRC06] being an outstanding isolator. This property enables its use as a holding structure material for the high voltage components like the meshes, the field shaping rings, and the PMTs. All these possible applications were the reason to use PTFE on a larger-scale. It was decided to build a Teflon structure where other components are integrated and which is filling up nearly the whole liquid containment around the TPC to avoid dead volume. In this bodywork, all other components are integrated. For assembling purposes, the PTFE structure consists of slices which are

stacked together with all technical installations integrated in between.

4.2.2. Meshes

The meshes are the essential parts in the drift field generation and three meshes are necessary to maintain the drift and the extraction field. In standard configuration, the bottom mesh is set to negative potential (cathode), the central mesh is at ground potential, and the top mesh is on positive potential (anode). To protect the PMT from high field regions, two additional screening meshes were installed between high voltage components and the PMT surfaces. The meshes are made by etching out of stainless steel sheets with a thickness of 125 µm making the handling challenging. To support the meshes and to facilitate the electrical contacting, the meshes have to be welded onto steel rings.
For a first welding test, a square mesh with 2.54 mm pitch, 125 µm thickness, and 125 µm wire diameter was used (see figure 4.1). The typical welding technique to fix such a mesh on a stainless steel ring with one or two millimeter thickness is spot welding. In the test, a few wires were welded onto a 2 mm thick ring to connect both parts electrically and mechanically. The test failed due to uneven expansion of the mesh and the frame causing deformations of the mesh as shown in figure 4.1.

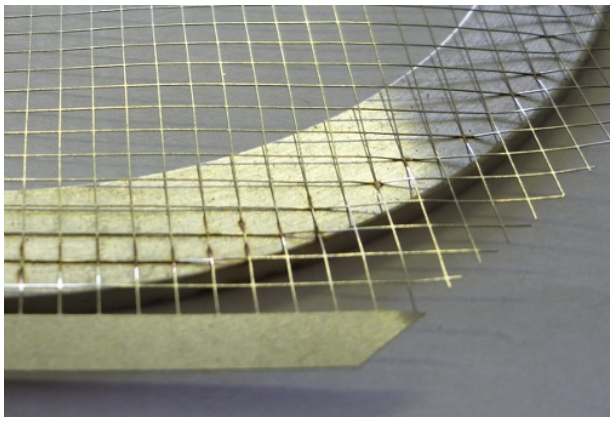

Figure 4.1.: *Squared mesh with 2.54 mm pitch, 125 µm thickness, and 125 µm wire diameter made of stainless steel welded on a steel ring. The test failed due to deformation of the mesh and broken wires. In the front of the picture, the frame is visible.*

In a second attempt, the frame of the mesh was welded on the ring and not the single wires. This worked perfectly fine. Concerning the results, custom made meshes were designed for the Münster TPC. The mesh parameters are 2.62 mm pitch, 150 µm thickness,

and 150 µm wire diameter. With an outer frame diameter of 115 mm and 5 mm frame width, they fit perfectly onto steel rings with CF100 size (inner diameter: 101.8 mm, outer diameter: 120.5 mm, thickness: 2 mm). Each mesh was fixed to a ring with 8 welding spots giving excellent connections. Figure 4.2 shows one round frame mesh welded on a steel ring to test the improvement.

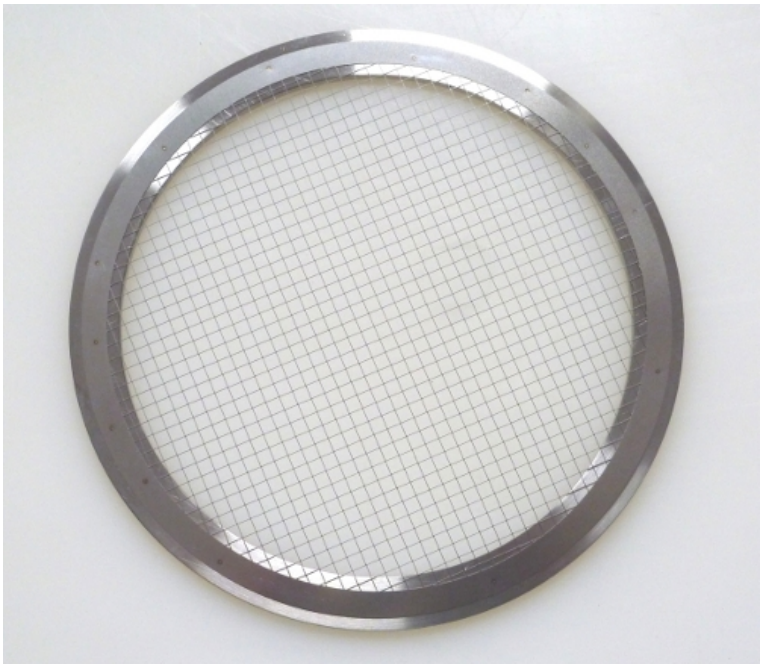

Figure 4.2.: *Custom made mesh for the Münster TPC welded on a stainless steel ring for test purposes. This connection can be created with little effort, but high quality.*

For the actual formation of rings and meshes to a field cage, two different simulations were made. One is dealing with the issues of spark discharging caused by high potentials on the cathode. The other one gives input for the general drift field design.

4.2.3. Cathode Simulations

In the XENON100 detector, it is not possible to apply more than −16 kV on the cathode without spark discharging, which is caused by the high electric field strength between the cathode and the bottom guard mesh. This is a limiting factor for the drift field strength and should be considered for the design of the Münster setup. Therefore, a simulation was implemented to determine the maximal field strength in the XENON100 detector at a stable run with −16 kV applied.

For the simulations, the Comsol Multiphysics software was used, which is based on the finite element method[1]. To simplify the model, symmetry conditions were exploited by modeling one unit cell of the mesh with one wire junction at the center of the cell and imposing periodic boundary conditions. The dimensions of the cell are set in a way that many of these cells next to each other would build up the mesh structure again. A simulation was performed with the XENON100 geometry yielding a field strength at the cathode mesh of 45 kV/cm. This provides an upper bound for the field strength for stable operation in the Münster TPC.
In the Münster setup, which is designed for 170 mm drift length, a voltage of at least −17 kV has to be applied onto the cathode to reach this field strength. For R&D, it would be interesting to be able to apply an even higher voltage. Therefore, further similar simulations were implemented to optimize the spacing concerning field strength and dead volume issues.
Further simulations were performed to optimize the design of the Muenster TPC, implementing the mesh geometry with 2.62 mm pitch, 150 µm thickness, and 150 µm wire diameter. In a distance of 3 mm below the screening mesh, a 1 mm thick quartz plate is simulated as the PMT window. A few boundary conditions are applied to this geometry: a uniform −19 kV potential 10 mm above the cathode, a uniform potential of −800 V on the photocathode under the quartz plane, a potential of −20 kV on the cathode, a potential of −800 V on the screening mesh, and symmetry on the side walls of the cell. The spacing between the cathode and the screening mesh was varied in the simulations to find the minimal distance without local fields of more than 45 kV/cm. The final simulation results are shown in figure 4.3. The distance between the two meshes is 19 mm in this case and the maximal local field strength is about 40 kV/cm. This is 5 kV/cm lower than the required value providing a safety margin.

4.2.4. Drift Field Simulations

The field shaping electrode structure was also simulated to optimize the design. The Comsol Multiphysics software was employed for these simulations again. This field simulation can be greatly simplified by exploiting the axial symmetry of the TPC, where the field can be calculated in two dimensions. This is not completely correct because the used meshes have a quadratic lattice structure (see section 4.2.2), but for the simulations, they are handled as single wires with the correct diameter and pitch. Therefore, it

[1] http://www.comsol.com/products/multiphysics/

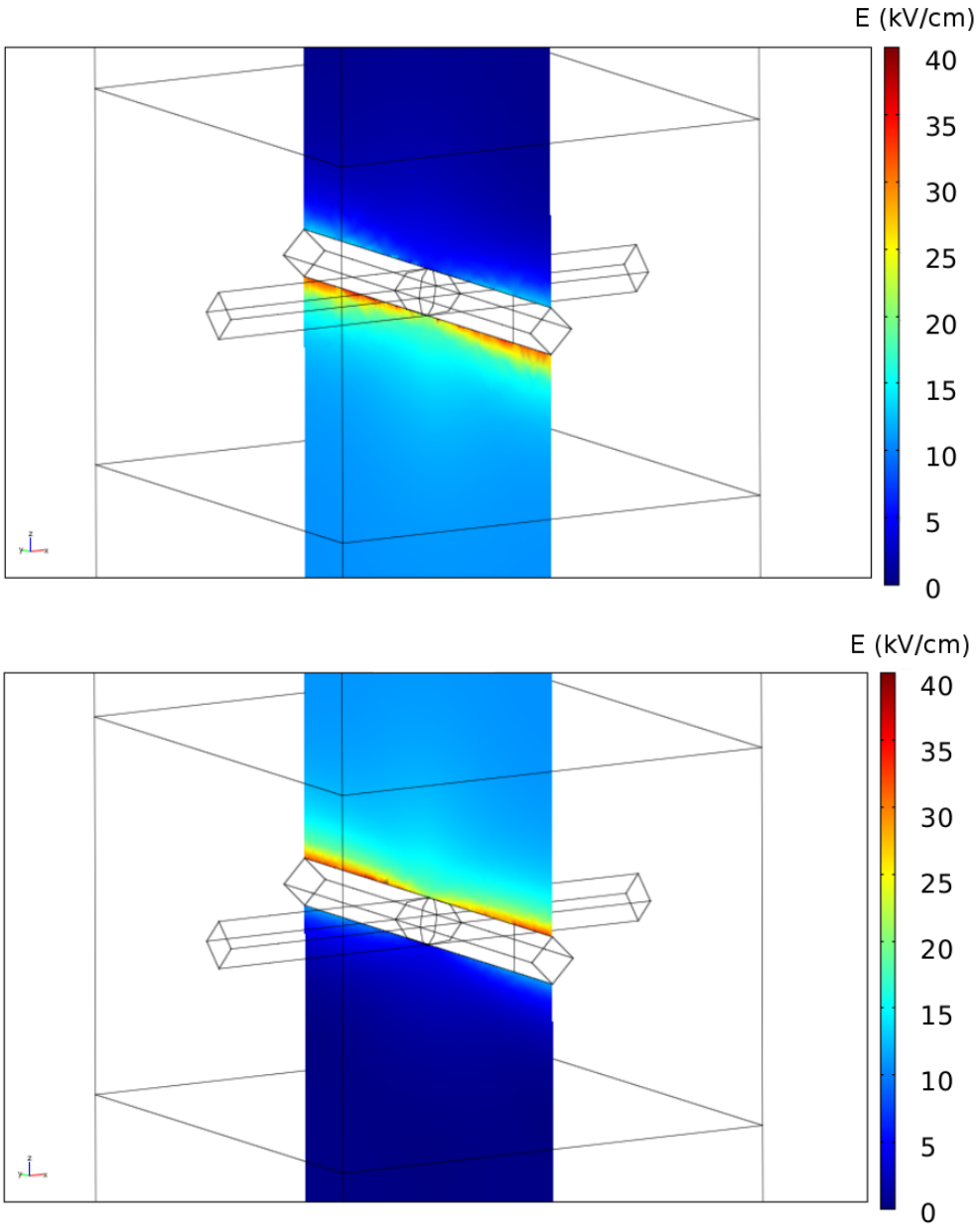

Figure 4.3.: *Simulation of the electric fields near the cathode (above) and the bottom screening mesh (below). With a distance of 19 mm in between and an applied voltage of* $-20\,\mathrm{kV}$*, the maximal field strength is expected to be 40 kV/cm, which is below the required maximum of 45 kV/cm.*

provides still a good guidance in case of field design.
The meshes and the field shaping rings are implemented correctly in size as well as the TPC volume and the steel cryostat. Further installations like PMTs, wires, resistors, and other internals are not considered. The Teflon structure does not consist of single slices, but is just handled as one piece. A visualization of the simulation setup is shown as an overview in figure 4.4, where two display modes are combined to one picture. On the left side, the electric potential inside the cryostat is shown as a surface plot. On the right side, the potential is displayed by iso-potential lines, which stand perpendicular to the electric field lines. The inner rectangle describes the TPC volume filled with LXe up to a point between the central mesh and the anode, as it is desired for proper operation. Above the liquid level, gaseous xenon is put in the simulation to complete the TPC implementation.
For the calculation of the fields, the electrodes are set to different electric potentials. The bottom mesh is set to ground for screening purposes and to the cathode, the next higher mesh, $-17\,\mathrm{kV}$ are applied. The spacing between these two meshes is 19 mm as discussed in section 4.2.3. In the actual realized design, the ring supporting the cathode mesh is broader than the other rings and has an inner diameter of 90 mm. This way the PTFE cylinder can be placed on top of it. Due to its different shape, the ring influences the field lines a bit, but as shown the impact is small (see figure 4.7).
Starting with the cathode, the above field cage is composed by 12 field shaping rings set to a continuously decreasing potential with steps of $(-17/13)\,\mathrm{kV}$. On top of this cage, three meshes are stacked, which consist of a ground mesh (gate mesh) separating the drift field and the extraction field region, an anode mesh producing the extraction field, and again a screening mesh. The spacing between these three meshes is 5 mm and the gap between the top screening electrode and the end of the TPC volume is 3 mm. By applying a voltage of $+5\,\mathrm{kV}$ to the anode, the extraction field has a strength of $10\,\mathrm{kV/cm}$ and the electron extraction yield is 100% (see figure 3.3).
To find the final layout, a basic investigation was made to test the field design for the best compromise between homogeneity of the field and space issues. Simulations using just two planes to create the drift field are implemented for that. By changing the number of shaping rings and therefore their distance, the minimum number of rings can be found as shown in figure 4.5. The plot is again showing iso-potential lines inside the TPC and in addition to that, drift lines of electrons are shown in black which follow the electric field lines. By this visualization method, a setup with 12 rings was identified to give

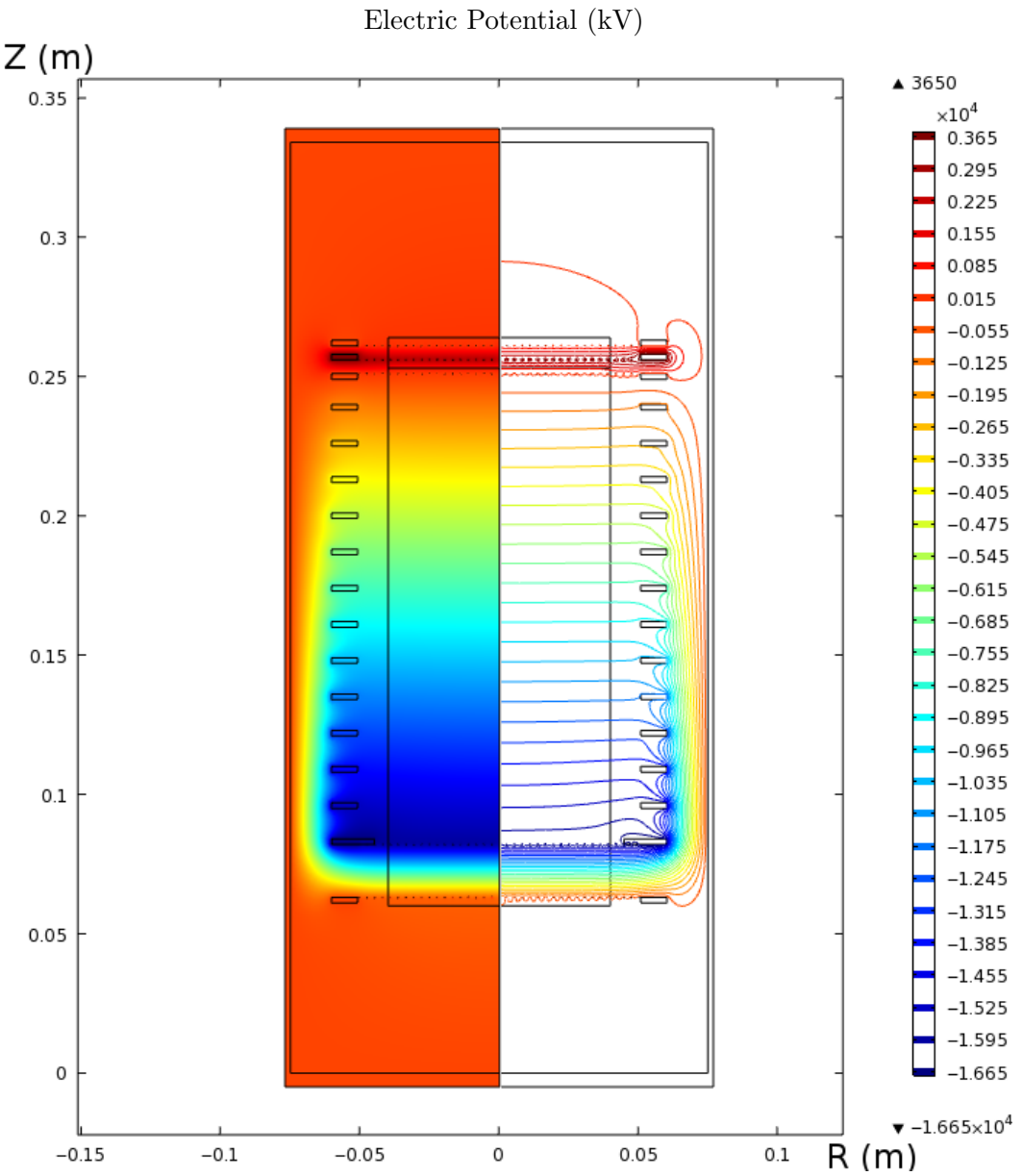

Figure 4.4.: *Overview of the electric potentials inside the TPC cryostat. On the left side of the picture, a surface plot is visible. On the right side, the corresponding contour lines are shown.*

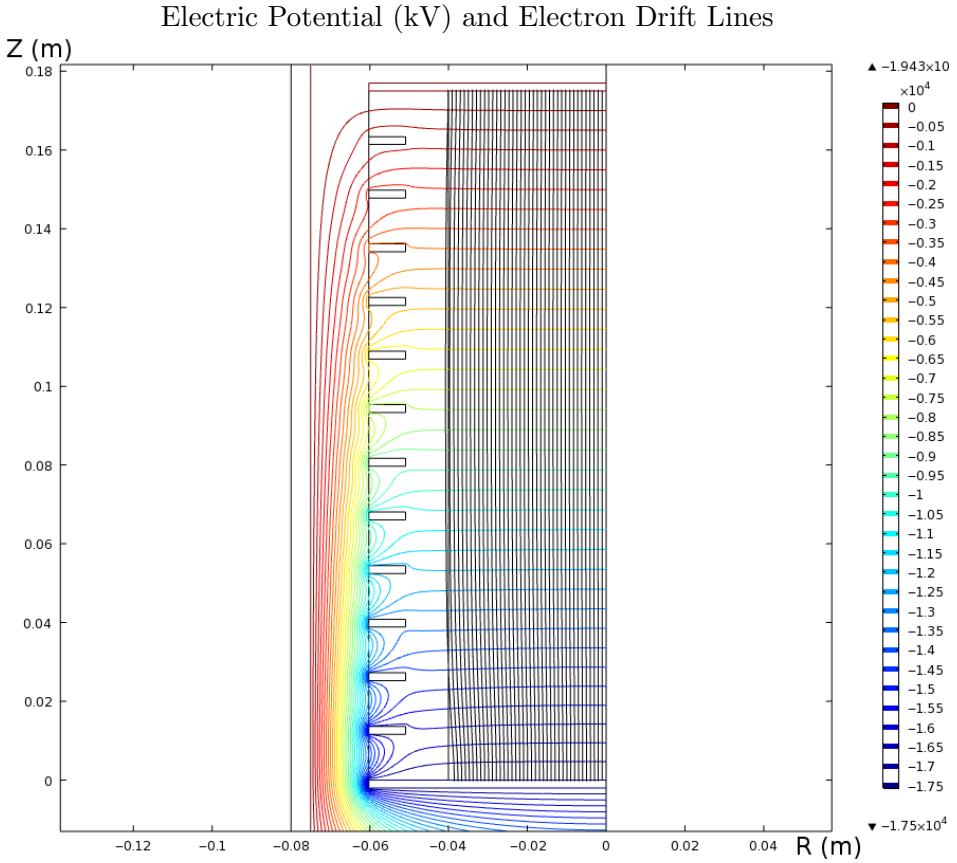

Figure 4.5.: *Simulation to find the minimum number of field shaping rings with a simplified geometry. By implementing two planes instead of the meshes and varying the number of shaping electrodes, the best compromise between field homogeneity and space issues was identified. The homogeneity of the field is thereby indicated by the black electron drift lines.*

a reasonably homogeneous field and 13 mm assembling space for the resistors between each ring. With further simulations, it can be shown that the iso-potential lines are deformed around the cathode due to the influence of the field below. For the real setup, a different curvature of the drift lines near the edges is calculated. Figure 4.6 gives an impression of the real drift lines which show a bending in the cathode area towards the middle axis, clearly visible in the left hand side plot (also see figure 4.7 (left)). The field created under the cathode is much higher than above and leaks through the mesh adding up vectorial with the field there. This has limited influence which affects mainly drifts starting in the area around the TPC bottom edges. In principle, corrections to the

position reconstruction algorithm can be applied to account for the non-uniform drift for events in this region. On the right hand side of figure 4.6, the electron drift lines are shown with a different starting point in z. These drift lines are not affected by the field deformation near the bottom edges of the TPC and show therefore an excellent straight behavior.

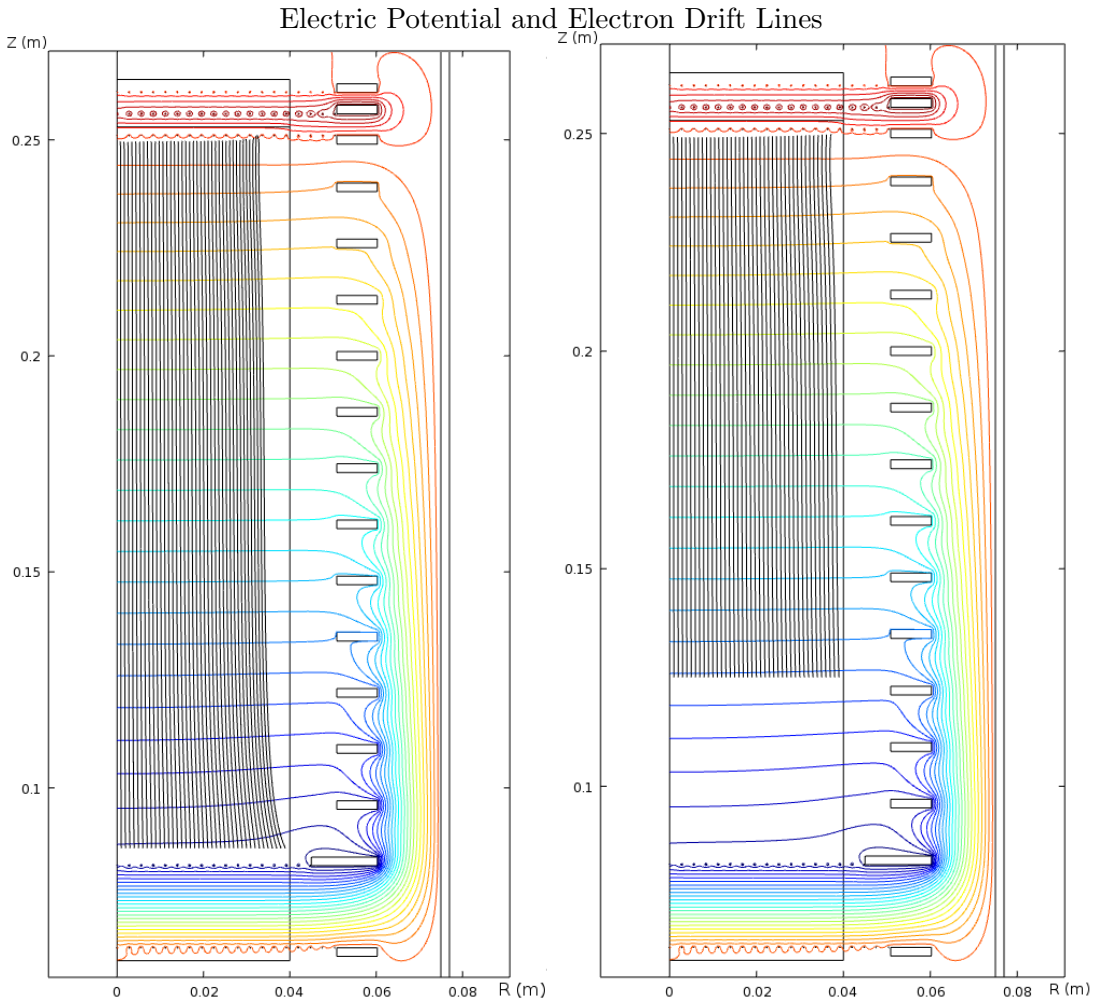

Figure 4.6.: *Simulations of the electron drift lines in the Münster TPC. On the left hand side, the drift lines of electrons starting right next to the cathode mesh are shown. Drift lines starting near the bottom edge of the TPC are deformed and bent towards the cylindric axis. On the right hand side, the drift lines start at a higher position in z and the field inhomogeneities in the corner have no influence on the drifts, which therefore show a straight line. The color scale for the iso-potential lines is the same as shown in figure 4.4.*

As already mentioned, a broader ring supporting the cathode, which is fixed underneath, produces small deformations of the field. To determine these deformations, the realized design can be compared to the situation where the mesh sits on top of the ring and its size has therefore no impact on the field above. Figure 4.7 shows how these two designs look like in the simulation with a zoom into the cathode area. Because of the very

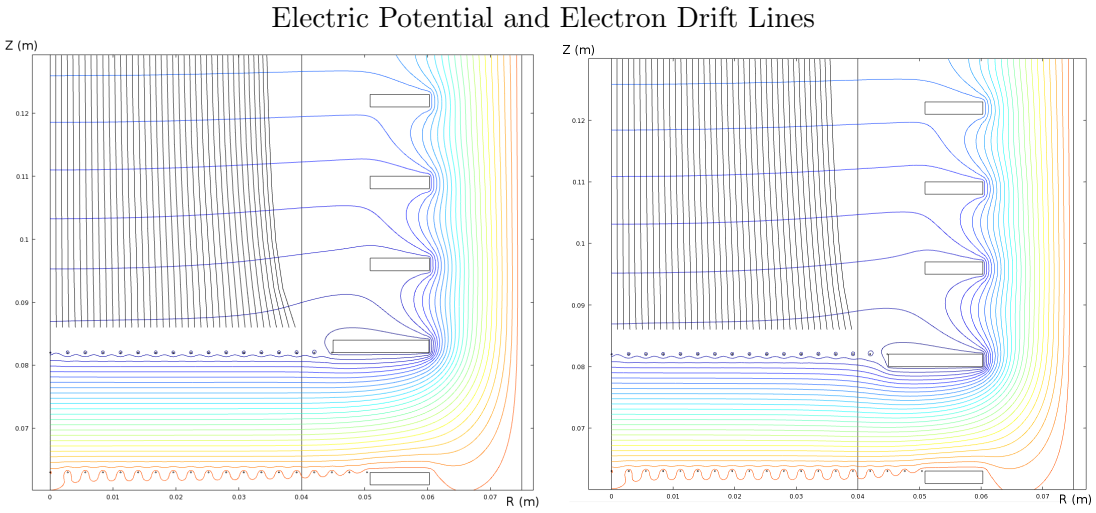

Figure 4.7.: *Close-ups of the cathode region with two different mesh orientations. On the left hand side, the mesh is fixed underneath the ring. On the right hand side, the mesh sits on top of the ring. Indicated by the black drift lines, a slightly stronger bending shows up in the left plot, but its impact is very small and only influences electron drifts starting very close to the ring. The color scale for the iso-potential lines is the same as shown in figure 4.4.*

small impact on the bending compared to the effects caused by field leakage through the cathode mesh, its influence can be neglected.

4.2.5. Resistor Chain

The voltage applied for the drift field has to decrease stepwise with each field shaping ring. It starts at the cathode going up to the ground mesh. A resistor chain is installed in the TPC as a voltage divider consisting of 13 steps. The resistors are high voltage thick-film resistors made by Vishay (model HTS 523). They have a resistance of 1 GΩ and their limiting element voltage is 5 kV. With these resistors, the chain offers a large dynamic range allowing for cathode operation up to −65 kV. For higher reliability, two redundant chains are integrated into the system. In case of the failure of an electric

contact at one of the resistors, the drift field can still be applied. If one connection breaks, the field will be slightly deformed, but general operation will nevertheless be possible without direct opening of the system.
To fulfill the low radioactivity requirement, the amount of solder used for electrical connections must be minimized. For the Münster TPC, the only connections where solder is used are on the PMT bases and the temperature sensors. All other contacts are using different techniques like crimp barrels or plugs. For the resistor chain, a very elegant way was found to connect the rings and the resistor wires. Four holes are drilled in every ring at the rim and female plugs consistent with the diameter of the resistor's lead wires are inserted. To avoid residual gases being trapped, which could lead to electronegative impurity in the xenon, each plug hole has a small vent hole. The final version of the contact is shown in figure 4.8.

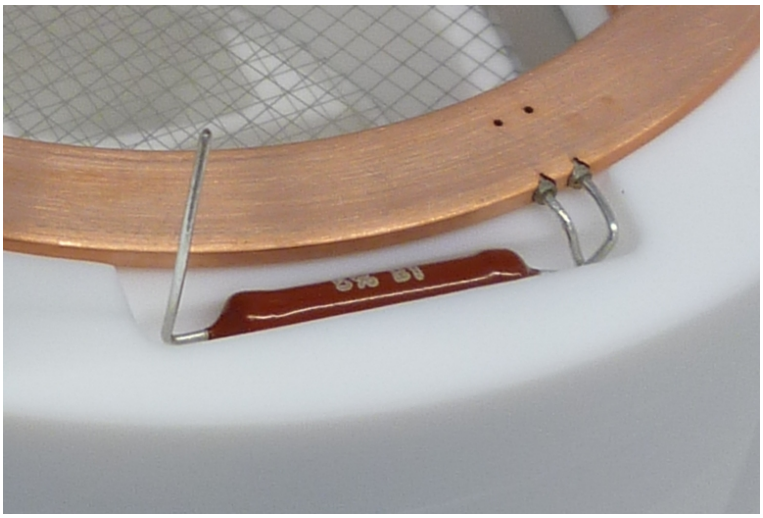

Figure 4.8.: *Electrical contact of a field shaping ring and two resistors as realized in the Münster TPC. Both resistors are connected with female plugs. Also visible are the two small vent holes.*

A temperature test was performed on the resistors and the connections to ensure proper operation at low temperature and stability through the heating cooling process. In this test, one resistor connected with two plugs was put into liquid nitrogen together with a PT100 temperature sensor. The resistor was dipped in and pulled out of the liquid a few times. The test was carried out with two Fluke 8508A multimeters, one for the resistance measurement itself and one for PT100 readout.
The resistance is about 3% higher at liquid nitrogen temperature than at room tempera-

ture, which is still smaller than the resistance tolerance of 5% given by the manufacturer. The resistance does not vary in time, it is reproducible, and it drops back to the original value with increasing temperature. During the measurement, the resistor was pulled out of the liquid and heated up a few times. All parts, resistor as well as the electric contacts, do not show failures in terms of cold operation or temperature changes, therefore it was decided to go for this solution. The same plug connection is used to connect the resistors to the steel mesh frames.

4.3. Level and Temperature Sensors

Level Sensors

The LXe surface has to be enclosed between the gate mesh and the anode for TPC operation. Due to their small spacing of 5 mm, a very accurate sensor is needed to maintain this level. In addition, it is necessary to make sure that the liquid surface is parallel to the meshes, which requires at least three level sensors. A common technique for level monitoring is a capacitor that changes its capacitance filled with liquid instead of gas because of the different dielectric constants. For the Münster TPC, three cylindrical capacitors were constructed with full TPC height coverage. They can be used to monitor the level between the meshes as well as to monitor the filling and recuperating process. The level sensors were made out of a 6 mm stainless steel tube with 1 mm wall thickness and a 3 mm steel rod. They have an active length of 294 mm and a 1 mm slit over the full length to avoid capillary action. For the electrical contact, a small steel plate with a hole is welded to each tube and rod. The isolation is realized with two polyether ether ketone (PEEK) spacers, one mounted at each end. The top end of the sensor is visible in figure 4.9.
For a cylindrical capacitor, the change in capacity ΔC with filling height l can be calculated to

$$\Delta C = 2\pi\epsilon_0\Delta\epsilon_r \frac{l}{ln(\frac{R_2}{R_1})}, \tag{4.1}$$

where $\Delta\epsilon_r$ is the difference between the dielectric constants of the gas and the liquid and R_1 and R_2 are the diameter of the rod and the inner diameter of the tube. For xenon with $\Delta\epsilon_r = 0.879$ [CRC06], the value for $\Delta C/l$ is expected to be

$$\frac{\Delta C}{l} = 2\pi\Delta\epsilon_r\epsilon_0 \cdot \frac{1}{0.288} = 0.170\,\mathrm{pF/mm}. \tag{4.2}$$

This value is valid for a complete cylindrical capacitor, therefore the used sensors are expected to have a slightly different value due to the slit in the tube. A test measurement with liquid nitrogen was performed where the sensor was stepwise pulled out of the liquid and after 14 cm, it was dipped into it again. The total capacity of the sensor and the wires was recorded every centimeter showing a capacity change of $(0.0786 \pm 0.0008)\,\mathrm{pF/mm}$ whereas $0.090\,\mathrm{pF/mm}$ is expected by calculations ($\Delta\epsilon_r = 0.467$ [CRC06]), see figure 4.9. A first measurement with xenon showed a value of about $0.176\,\mathrm{pF/mm}$, but this has to be investigated further. Nevertheless, the test shows that the level meters are basically working as expected. The readout is done by a measurement of the discharging

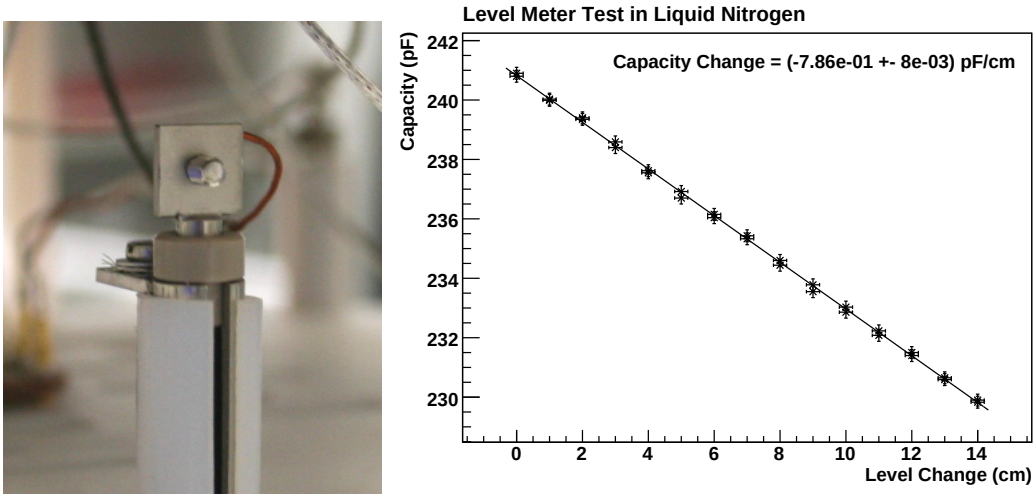

Figure 4.9.: *On the left hand side, the top end of the level sensor with wires is visible. For reasons of isolation, it is wrapped in a PTFE tube. The wires are attached with small screws to the steel plates. On the right hand side, the result of a test measurement with liquid N_2 is shown. The level sensor was stepwise pulled out of the liquid and after 14 cm, it was dipped into it again. The total capacity of the sensor and the wires was recorded every centimeter and is plotted against the level change.*

time over an exactly known resistor. A micro controller, named ATMega328, produced by Amtel, which sits on an Arduino board, is used for this. In the provisional setup, three measurements are made and the single values are compared to see if one value has a deviation greater than 3 measuring steps (0.114 pF) to the other two. If this is not the case, the average over all capacities will be displayed. If one of the values has a greater deviation, this value will be rejected and the average over the other two will be displayed and if all of them are deviating, the entire measurement will be rejected. In

addition to the output on a display, a voltage proportional to the capacitance is given out to the control system. The time between data taking is one second which gives a sufficient temporal resolution. In the next step, the number of single measurements will be increased to about 100, which will lead to much lower fluctuations.
To charge the capacitor, a positive voltage is applied onto the rod. The outer tube is kept on ground potential avoiding dipole radiation.

Temperature Sensors

Two sensors are used to monitor the temperature inside the TPC cryostat, one in the gas phase and one in the liquid xenon at the bottom of the cryostat. The sensors are PT1000 resistance thermometers connected to a four-wire Kelvin connection, in this case a Lakeshore Cryogenic Temperature Controller model 336.

4.4. PTFE Structure

The initial layout of the TPC, as presented in section 4.2.1, uses PTFE for the main part of the bodywork. This is realized by a stack of differently shaped Teflon slices. The stack can be subdivided in four parts, which are the two holding structures for the top and the bottom PMT arrays, the support structure of the TPC itself, and the inner reflection cylinder. Figure 4.10 shows the stack of slices as a photograph and a sectional view from the mechanical drawing. The meshes and PMTs are integrated in four PTFE parts on top and four at the bottom, which are all unique. Two times seven separated cavities are used to hold the PMTs and isolate them electrically. They are arranged with a gap of 2.3 mm between each PMT due to manufacturing reasons. This gives a photocathode coverage on top and bottom of 56%, which is high enough to meet the demands of 3D position reconstruction and light collection.
Between the top and bottom structure, 13 ring like slices are responsible for housing the electrodes and the resistor chains. Figure 4.11 shows an overview of how the different parts like wires, sensors, resistors, electrodes, and holding rods are integrated into the PTFE. The grooves are machined at the outer face to maximize their distance to the high voltage electrodes. For isolation purposes, all structures going along the TPC in a groove are covered with PTFE tubes. The anode and the cathode high voltage line are not guided in an outer groove, but they are directed through holes in the Teflon slices. This provides more isolator material around the copper lines which are sheathed with a

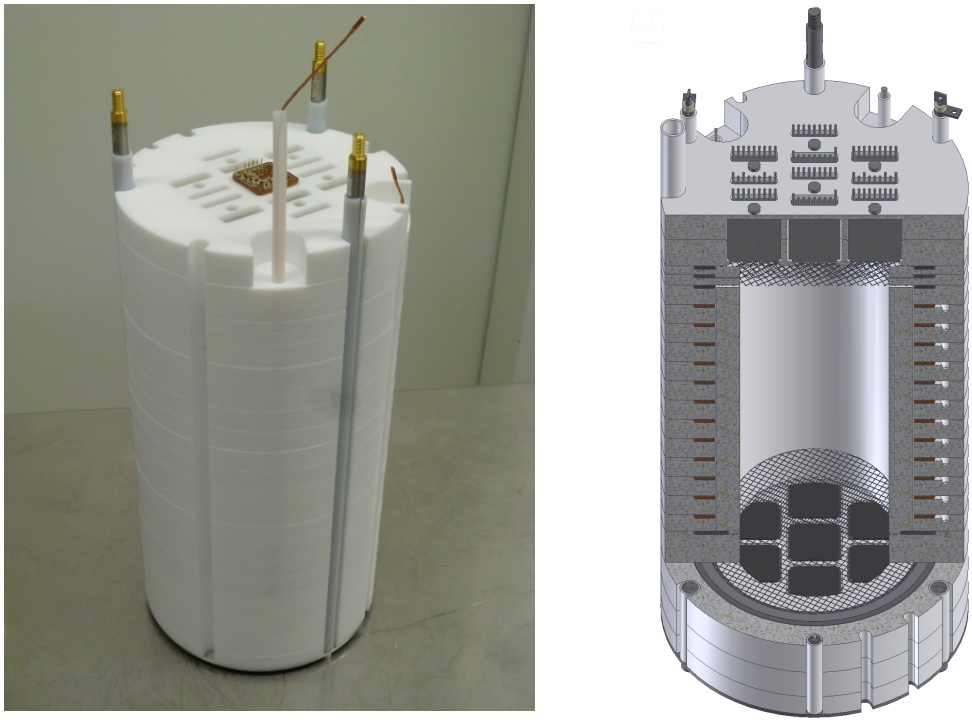

Figure 4.10.: *The two pictures show a photo of the assembled PTFE stack of the Münster TPC on the left hand side and a sectional view of the corresponding mechanical drawing on the right hand side.*

PTFE tube as well. The cathode line is visible in figure 4.10. The electrodes are fitted in gaps on top of the slices and for each resistor, a separate groove with a small hole through the Teflon piece was reamed. The resistor can be fitted in completely and one of its wires can contact the next layer above through the hole. In figure 4.8, a mounted resistor is visible.

The stack is mounted onto the top flange of the vessel which provides all feedthroughs into the cryostat. This is very helpful for assembling because it allows to connect everything before lowering the structure into the liquid containment. The mounting is realized by a stainless steel plate where the stack sits on and which is connected to three rods by screws. The rods are fitted into the already mentioned grooves and covered with PTFE tubes. Threads are machined at the top end of the rods to screw them into the flange. The three rods are visible on the left side of figure 4.10. The reason why the threads are gold plated will be explained in section 4.6.

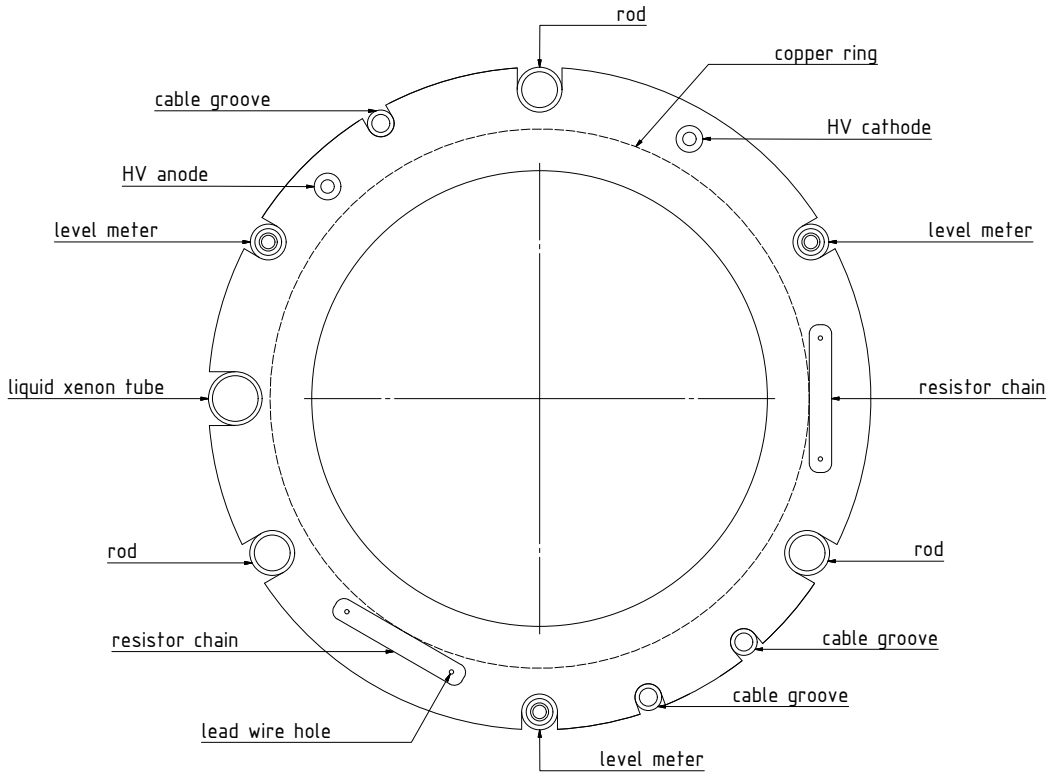

Figure 4.11.: *Top view scheme of the TPC support structure made of PTFE. Ten grooves are at the outer face, 3 for the supporting rods, 3 for the level sensors, 3 for the wires, and 1 for LXe. In addition, 2 holes are going through the slices for the high voltage lines. A gap for the copper ring and 2 grooves for the resistors are around the inner face. In the resistor grooves, there are small lead wire holes to connect the layers.*

4.5. Feedthroughs

All electrical installations in the liquid containment have to be connected to the outside. In the design of the Münster TPC setup, 61 lines are provided in total. The wide range of applications, as listed in table 4.1, requires different feedthroughs (FT).
Basically, the connections can be classified in four groups: signals and signal guards needing 42 lines, small high voltage needing 15 lines, anode high voltage, and cathode high voltage. The additional two ground lines for the screening meshes are handled together with the small high voltage lines. For each group, a separate FT is used because of the different requirements in voltage and number.

Table 4.1.: *Overview of all electrical lines guided out of the TPC cryostat.*

electrical component	**lines**	**guard lines**
PMT HV (<1 kV)	14	-
PMT signal	14	14
level meter signal	3	3
PT1000 signal	8	-
anode HV (4 kV)	1	-
cathode HV (20 kV)	1	-
screening mesh ground	2	-
screening mesh HV (800 V)	1	-
total		**61**

The following feedthroughs made by Hositrad are utilized. For the cathode high voltage, a 50 kV alumina ceramic isolated single pin bushing (21184-01-CF) is used. All 42 signal lines are handled with two 25 pin glass-ceramic sub-D FTs (21109-01-CF) providing eight spare pins. The multiple high voltage and ground lines are guided by a 1 kV FT with 19 pins (18853-01-W) and the anode HV is led in by a 10 kV alumina ceramic isolated single pin brushing. All of these parts are certified for a temperature range of −269 °C to +450 °C and at least up to 28 bar pressure at 20 °C.
To gain more flexibility in case of setup changes, these FTs are not welded directly in the top CF160 flange, but into smaller Conflat flanges, which are then mounted on the CF160. A CF160 flange does not provide enough space for direct realization. A workaround is necessary and flanged sockets are used in the Münster TPC to fit the FT flanges onto the chamber. The cathode bushing is welded in a CF40 whereas the two sub-D connectors need a CF63 to fit in. The anode high voltage FT is also welded in a CF40, but together with the small high voltage multi pin FT.
The ConFlat system is made for chambers with vacuum inside and air outside of a vessel. In the TPC, the situation is the other way round because gaseous xenon is next to the top flange inside the cryostat and an insulation vacuum is outside. Therefore, the manufacturer specifications for the electric strength have to be validated by measurements in a setup similar to the real conditions. Due to the low voltages on the sub-D connectors and on the multiple HV FT, only the other two parts were tested.
To simulate operation conditions, a Conflat chamber was equipped with a gas inlet and connected to a pump with a valve in between. As preparation, the setup was pumped

down and then closed by the valve before flushing it with 2 bar argon. Argon can be used for these simple test because its characteristics are similar and it is much cheaper than xenon. To check the cathode FT, a 45 kV resistor was connected to the feedthrough and the vessel side to enable a current like in the TPC. The high voltage is created by a FUG HCL 35-35000 power supply with a maximal output of $U_{max} = \pm 35\,kV$ and $I_{max} = 1\,mA$.

The two bushings were tested individually by applying high voltages ramped up to the break down voltage. First measurements with argon inside the chamber showed that the FTs could just be ramped up to 3.2 kV on the anode and −12 kV on the cathode.

In order to improve the cathode FT performance, an additional insulator made out of PEEK was machined which can be imposed on the ceramics. This modification provides a break down voltage of −28 kV which fulfills the requirements.

The problem with the anode FT could not be solved this way because of the small distance between the two FTs on the CF40. With applied high voltage, there was a breakdown on the gas side, which had been designed for vacuum. Thus, it was tried to use the FT upside down. In another test with a turned FT and PTFE tape around the pin on the vacuum side, it was shown that this allows to apply more than 5 kV on the anode FT. All test results are summarized in table 4.2. To actually realize this solution,

Table 4.2.: *High voltage tests of the anode and the cathode feedthrough.*

	FT vaccum side	FT air side	U_{max} (kV)
anode FT			
	argon	air	3.2
	vacuum	air	10
	air (with PTFE tape)	argon	>5
cathode FT			
	argon	air	−12
	argon (with PEEK insulator)	air	−28

the initial design was changed and the CF40 was mounted inside of the vessel on the top flange. This was possible by cutting a knife edge directly in the CF160. Figure 4.12 shows the top flange in the final state with anode FT installed on the inside and blind flanges on the outside. In addition to the electrical lines, two pipes have to go through

the flange, as an inlet and outlet for the xenon. This is realized with two half inch tubes welded directly in the flange. One is ending at the inner edge of the flange and the other one continues with a connector to a half inch PTFE tube which guides the xenon all the way down to the bottom. On the other ends of the tubes Swagelok VCR connectors are installed. With this design, it is possible to introduce liquid xenon to the bottom area of the TPC, whereas gaseous xenon can be taken out at the top flange. Compared to the method used in XENON100, which works with liquid-out and gas-in, this reduces the required cooling power (see also chapter 5).

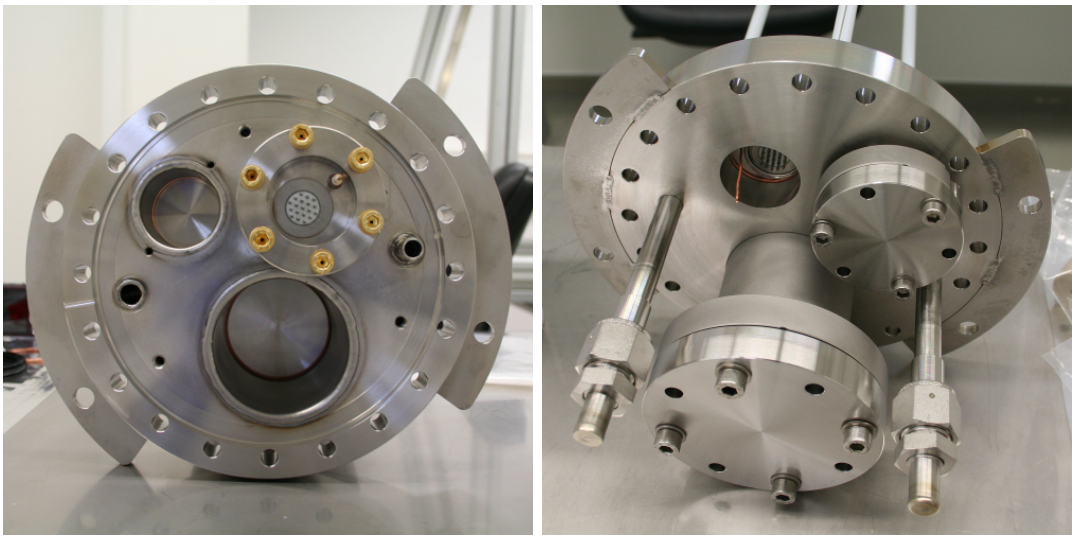

Figure 4.12.: *Top flange of the TPC cryostat. The anode feedthrough is mounted in place on the inside. The two flanged sockets outside are covered with blind flanges. Also visible are the two 1/2 inch tubes for xenon in- and outlet.*

4.6. Assembling

The high purity demands required the assembling in a dust free environment. Therefore, the whole construction work took place in Münster's ISO 7 class clean room. Beforehand, all steel and PTFE parts were cleaned in an ultra sonic bath to remove grease, dust, and residue from machining. For the steel parts, a special detergent called Almeco was used in the first cleaning step and then the parts were rinsed with deionized water. The PTFE components were just cleaned with the deionized water and ultrasound. All components were dried for several hours at about 120 °C after cleaning and for the storage time the

workpieces were single packaged in airtight foil. Right before the assembling of a piece, it was wiped with pure alcohol. The TPC was constructed from the bottom up, which means the bottom steel plate and the three holding rods were screwed together first and then the Teflon was stacked onto. For the first tests, only two PMTs were installed, one in the middle of the bottom holder and one in the middle of the top holder.
The PTFE bodywork was mounted on the top flange and the cabling was done in the last step before closing the containment. In figure 4.15, impressions from the assembling process are shown and another detailed technical drawing can be found in the appendix in figure A.2.
A screwed connection installed in an ultra pure environment is problematic because grease is not allowed. To avoid deformation of the threads, it is nevertheless necessary to use a lubricant and therefore the screws are gold plated. Pure gold is a very soft material and acts as slip additive at first tightening of the screws.

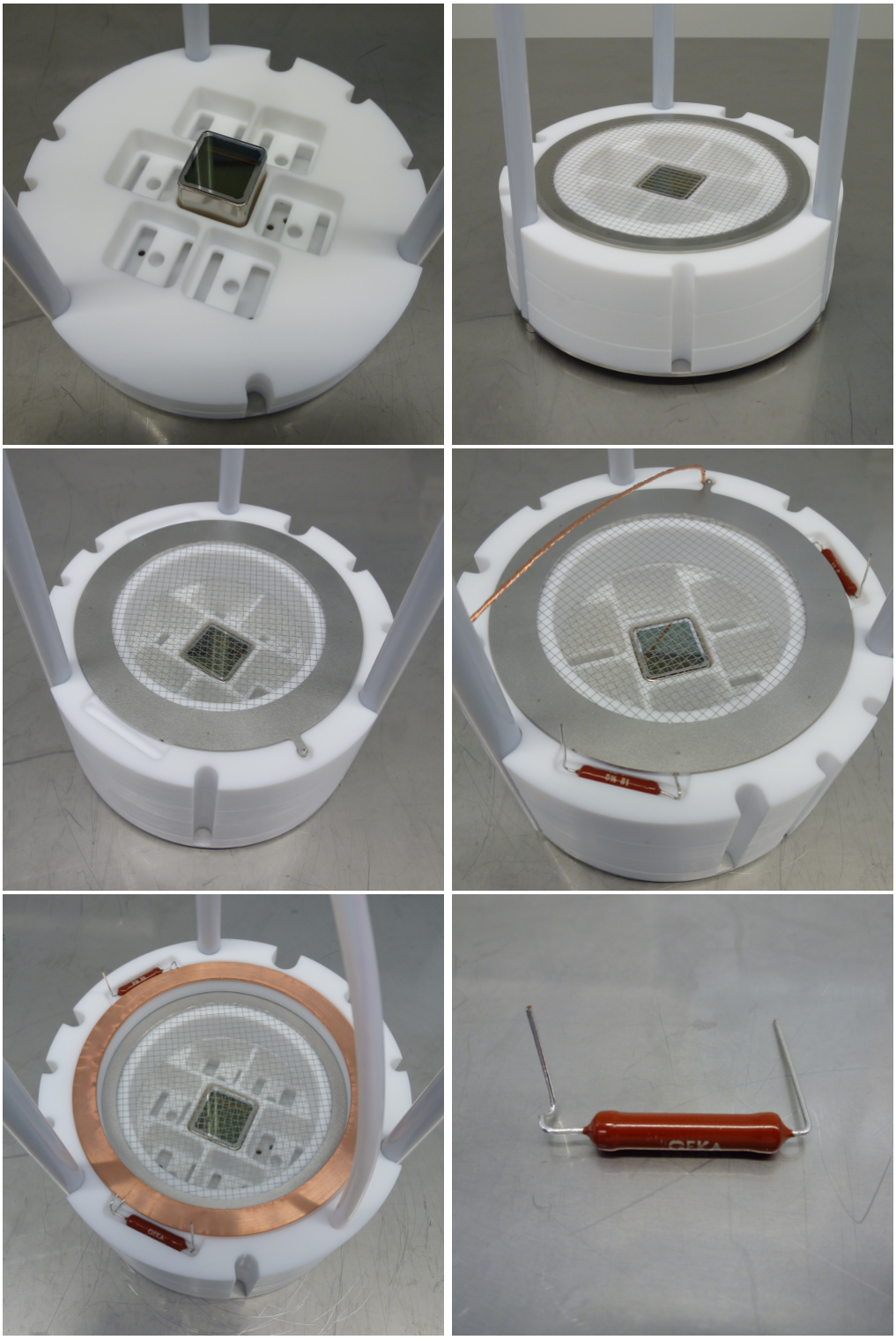

Figure 4.13.: *Impressions from TPC assembling. Shown is the setup of the bottom PMT-array holder, the bottom meshes, and one of the used resistors with bent wires.*

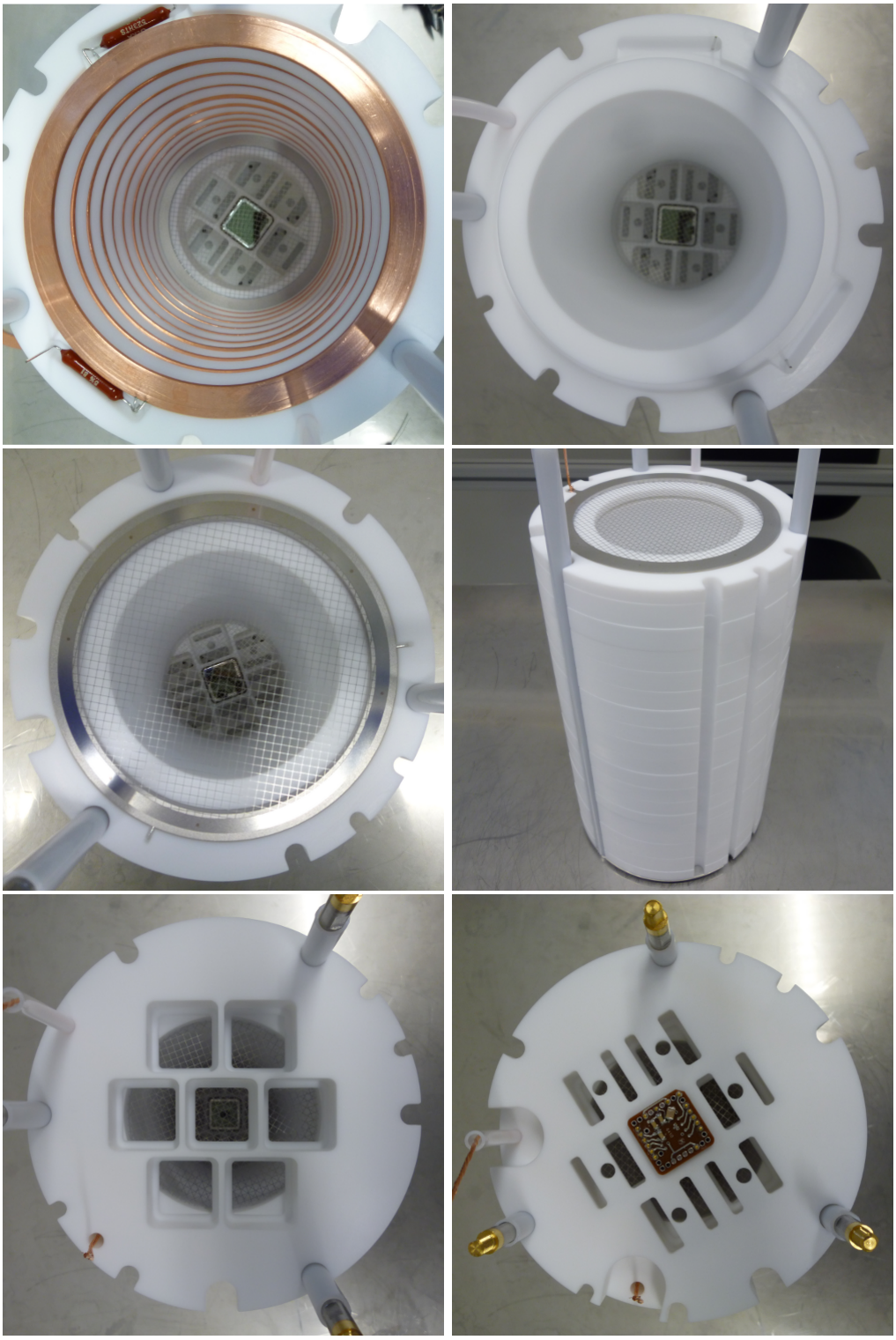

Figure 4.14.: *Impressions from TPC assembling. Shown is the setup of the TPC field cage including the PTFE reflector, the upper meshes, and the top PMT-array holder.*

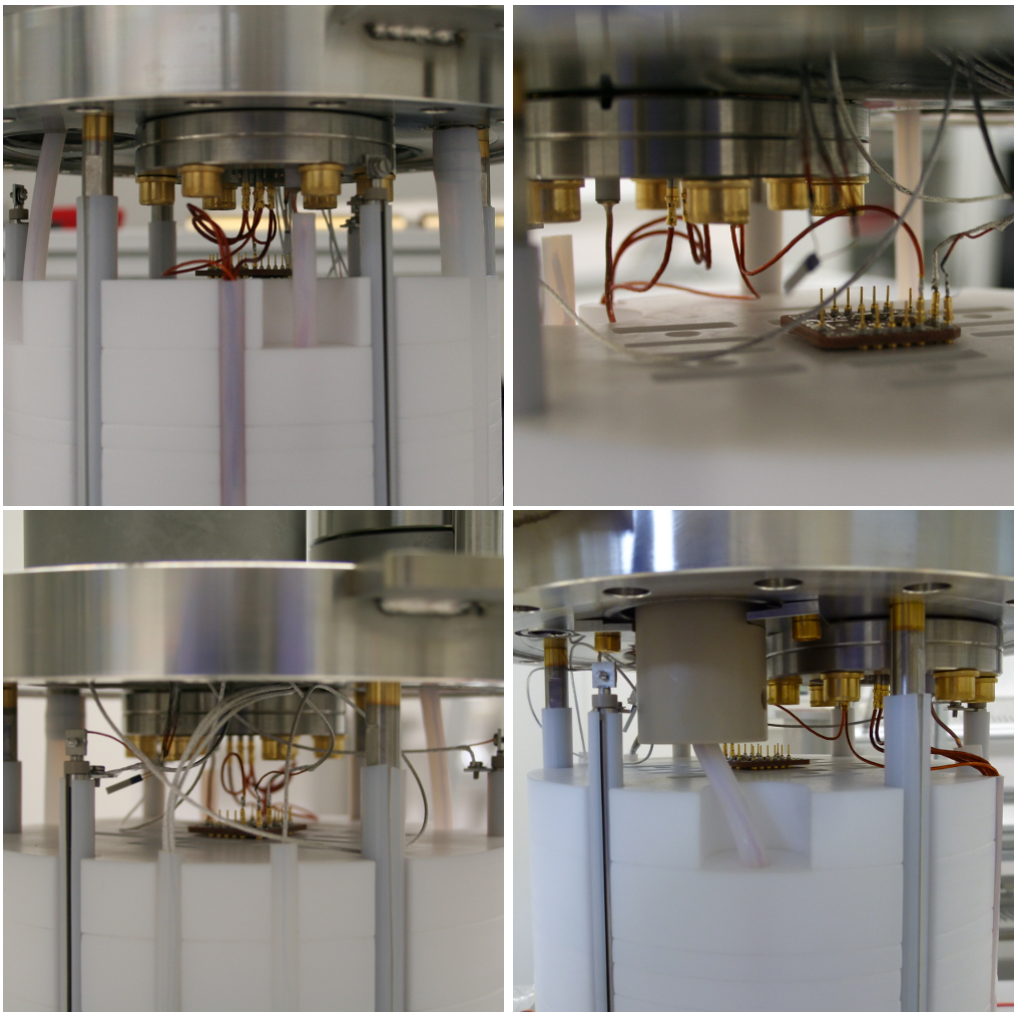

Figure 4.15.: *Shown in the figures 4.13, 4.14, and 4.15 are impressions from the TPC assembling process that took place in the clean room environment. Starting with the base plate, all Teflon slices were stacked one after another holding the electric installations like PMTs, meshes, ring electrodes, resistors, sensors, and cables in between. After the field shaping ring structure was completed, the PTFE reflector was inserted from above and the TPC was closed with the upper meshes and the top PMT-array holder. At the end, the complete TPC was mounted to the top flange and all the cabling was done under the limited conditions of space.*

5

The Cooling Tower

To fill the TPC with liquid xenon, an efficient cooling system is needed and for operation, a permanent liquefaction of xenon is essential. The purification of xenon is done by a SAES zirconium getter cleaning gaseous xenon. For that purpose, the xenon is taken out of the detector, pumped through the hot getter, and liquefied while filled back in. A stable long term operation of the setup requires an efficient and reliable cooling system that is designed for continuous operation without long maintenance and service periods.

5.1. General Aspects of Recirculation Modes

There are two modes to run the xenon recirculation. The first mode is the one used in XENON100. There, liquid xenon is taken out from the bottom of the cryostat, it vaporizes on the way through the gas purification system and the cleaned gaseous xenon is filled back into the TPC cryostat. The liquefaction process thereby takes place in a separate cycle, decoupled from the purification system. The second method is the other way round. Gaseous xenon is taken out from the top of the TPC cryostat where it is already vaporized. It is cleaned, liquefied and then filled back in at the bottom of the TPC cryostat.

For the Münster setup, it was decided to go for the liquid-in and gas-out procedure. This way, the cooling power consumption is lower and it has an advantage regarding purity. The power necessary to liquefy xenon is about 9.0 W/SLPM[1], which is a lot compared to the power required to cool down gaseous xenon from 293 K to 176 K at the same pressure of 0.180 MPa, which is 1.9 W/SLPM [Gib11]. Therefore, most of the expanded cooling power is required for the phase transition between gas and liquid. If gaseous xenon is taken out, it will only be necessary to liquefy this amount after the purification. If, in contrast, liquid xenon is taken out, it will have to be liquefied after putting the gas back into the TPC cryostat as well as the amount of xenon vaporized

[1] SLPM: Standard Liter Per Minute

inside the detector vessel due to the heat load of the system. This means, an additional heat load is created, which can be avoided if the already vaporized xenon is taken out of the cryostat. Furthermore, impurities contained in the TPC vessel move upwards to the gas phase by convection, therefore it is only natural to introduce clean xenon at the bottom of the cryostat and take out the impure xenon gas at the top.

5.2. Basic Design

In the realized design, the TPC itself is decoupled from the liquefaction unit, which is called the cooling tower, to have a flexible setup. This configuration allows to change the TPC cryostat with any other cryostat used for R&D measurements with liquid xenon. Therefore, the TPC and the cooling tower are housed in two separated ConFlat (CF) cryostat linked with two flexible lines for gas in- and outlet. The two cryostat vessels are arranged in one big vessel for vacuum insulation. Figure 5.1 shows a mechanical drawing of the vacuum vessel's interior, another technical drawing of the whole setup including the vacuum vessel is shown in the appendix in figure A.3.
The construction is made in a way that every part inside the vacuum vessel is fixed at the top flange. Therefore, it is possible to lift the whole setup out of the vessel for service and changes on the system. It is also very convenient for assembling because all electrical and mechanical connections can be installed at the naked setup before it is placed in the vacuum tube.

5.3. Cooling Tower

The heart of the cooling tower is a refrigerator cold head of Gifford-McMahon type (Leybold, Coolpower 50), which is connected to a self-produced cold finger machined of oxygen-free high thermal conductivity (OFHC) copper. To enlarge the surface of the cold finger, cooling fins were cut out of the copper. As visible in figure 5.2, the cold head is pressed onto the cold finger by clamps ensuring an optimal thermal contact. The cooler is housed in a small stainless steel vessel with a CF100 flange on top and cone like machined bottom. The edge of the cold finger allows the tightening of the vessel without an additional gasket, and its thickness gives the chance to remachine it after opening the system. For temperature control, a heater cartridge and a Si-diode temperature sensor are inserted into the copper at the rim. The cooling tower has two gas line connection. For gas inlet, a half inch tube is bent spirally around the vessel to avoid icing at the

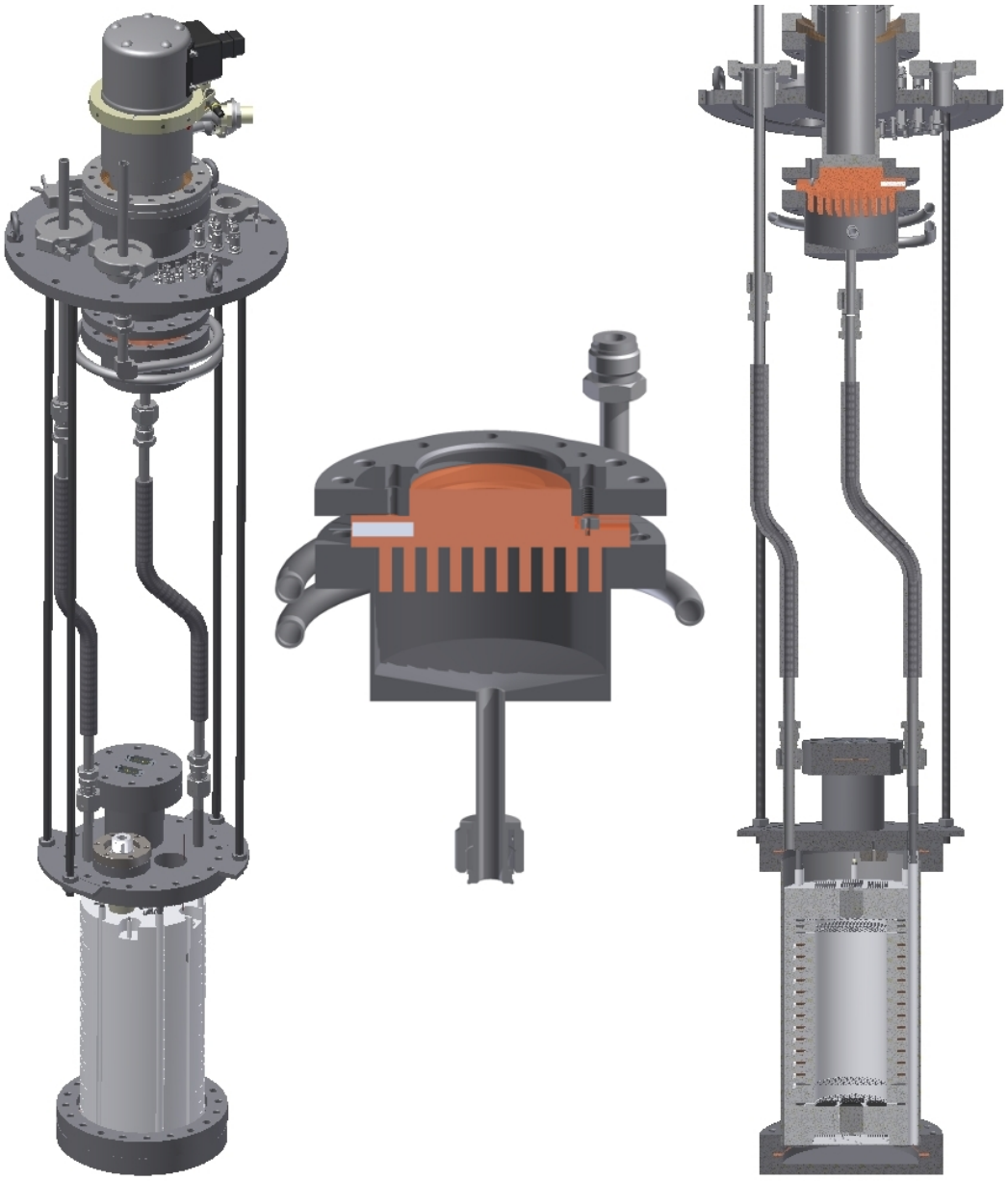

Figure 5.1.: *In this CAD-simulation, the inside of the vacuum cryostat is shown. The TPC cryostat tube is transparent and the PTFE structure becomes visible. On the right hand side, a sectional view of the setup shows the inner installations. In the center, a close-up sectional view of the cooling tower is shown.*

vacuum feedthrough. For the liquid outlet, a short half inch tube is welded to the lower surface and connects the cooling tower and the TPC vessel with a flexible line. Further information about the cooling tower are given in the appendix in figure A.1.

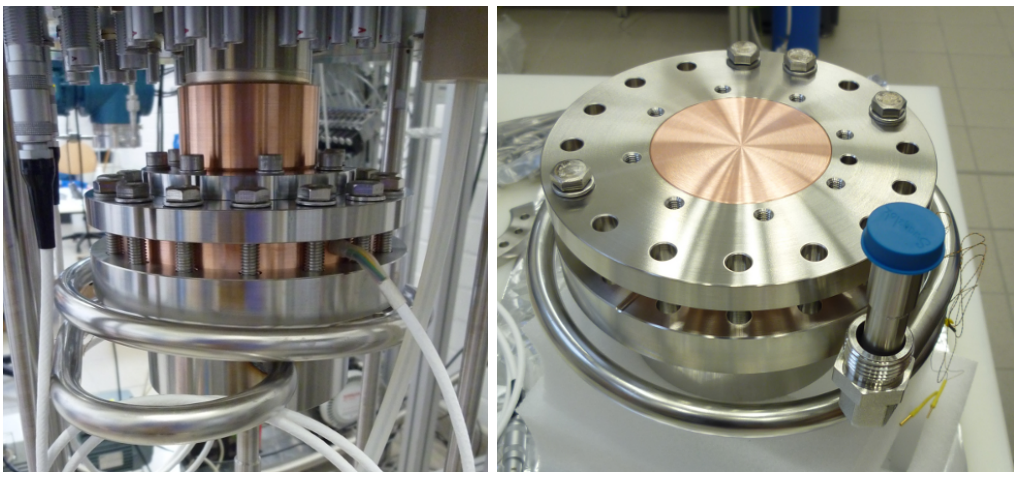

Figure 5.2.: *In these pictures, the connection between cold head and cold finger is shown. It is realized with two semi-circular clamps which press the cold head onto the cold finger providing a good thermal contact. Additionally, the clamps are used to suspend the whole cooling tower from the cold head. The spirally bent tube for the gas inlet is visible as well.*

5.3.1. Temperature Control

The used cold head has a constant cooling power depending on the operation temperature. The required cooling power of the system in contrast varies especially during the cooling stage. To regulate the temperature, a control unit is used which consists of a heater cartridge and a Si-diode connected to a Labview operated Lakeshore Cryogenic Temperature Controller (Model 336). The actual temperature regulation uses the heater to tune the net cooling power which depends on three terms:

$$\text{net cooling power} = \text{cold head cooling power - heater power - heat load.} \tag{5.1}$$

The used setup allows the performance of a very stable temperature control method, called proportional-integral-derivative control (PID-control).
In a temperature control test measurement, the stability of the temperature was investigated and the result is shown in figure 5.3. Over a long term run of 80 hours, the set point was fixed to $T_{set} = -100\,^{\circ}\mathrm{C}$ (green line) with a maximal deviation of

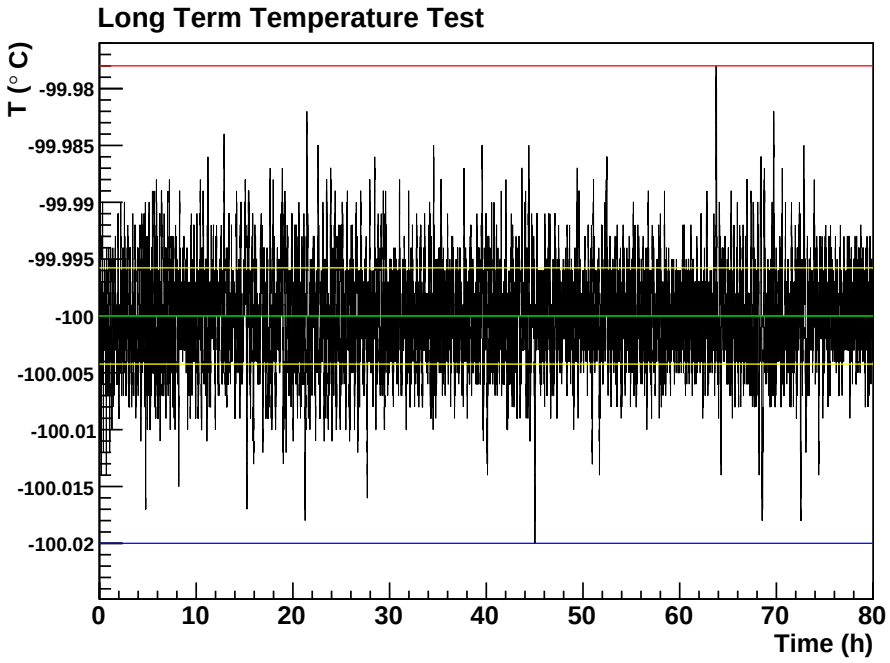

Figure 5.3.: *Long term measurement of the temperature for a set point of* $-100\,^{\circ}\mathrm{C}$ *shown by the green line. The red line indicates the highest and the blue line the lowest value measured. The fluctuations showed a maximal range of* $\Delta T_{fluc} = 0.042\,^{\circ}\mathrm{C}$ *(between blue and red line) and a standard deviation of* $\sigma = 0.004\,^{\circ}\mathrm{C}$ *(yellow lines).*

$\Delta T_{dev} = 0.022\,^{\circ}\mathrm{C}$ (between green and red line). The fluctuations showed a maximal range of $\Delta T_{fluc} = 0.042\,^{\circ}\mathrm{C}$ (between blue and red line) and a standard deviation of $\sigma = 0.004\,^{\circ}\mathrm{C}$ (yellow lines). The measurement was made during real operation and xenon was circulating through the system at all times. Because the fluctuations are sufficiently small, no tuning of the used PID-parameters is necessary.
This accurate temperature control allows to determine the cooling power as function of the temperature by a test measurement, where the temperature at the cold finger is set to different values and the cooling power is calculated by measuring the current flowing through the $25\,\Omega$ heater cartridge. The results are shown in figure 5.4.

5.4. Insulation Vacuum

The cold head cooling power is limited and the higher the heat input to the system is, the lower the net cooling power becomes (see equation 5.1). Therefore, an adequate

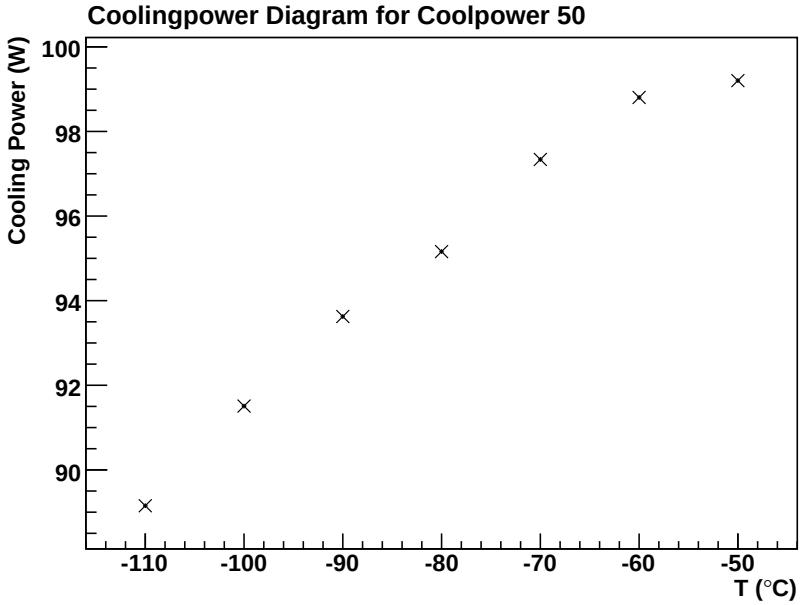

Figure 5.4.: *Cooling power as a function of the temperature at the end of the cold head for the MS-TPC setup. The power is calculated by measuring the current flowing through a 100 W heater for different temperature set-points. The error bars of this measurement are smaller than the symbols.*

insulation is necessary to keep the heat input by conduction and convection as low as possible. This can be achieved by keeping the cryostats in an insulation vacuum.
Thus, the TPC and the cooling tower are housed in a big steel vessel with a diameter of about 270 mm and a length of 1500 mm. For the vacuum purposes, a standard combination of a turbomolecular pump (Leybold TURBOVAC 361) and a rotary vane pump (Leybold TRIVAC D16B) is used.

Seals and Feedthroughs

The chamber is sealed by different kinds of gaskets which were chosen depending on the individual parts. Lemo single pin coaxial feedthroughs are used for the signals from PMTs and the PMT high voltages. The level meters, the temperature sensors and the heater are fed out by Lemo coaxial connectors with four lines. All Lemo parts use an elastomeric o-ring gasket. The gas in- and outlet are half inch tubes welded in two Klein flanges (KF40) mounted on flange sockets. The high voltage line for the cathode is

guided into the vacuum by the same feedthrough as used on the TPC flange, but welded in a KF40. For the anode, a KF25 5 kV SHV feedthrough is installed. In addition, two CF100 connections are required for the turbo pump and the cryocooler. The top and the bottom flange of the vacuum tube itself are sealed with ISO large flange gaskets. With all these elastomeric o-rings, a pressure of less than 9×10^{-7} mbar can be achieved in the vacuum vessel without cooling, which is much lower than the required vacuum for a good thermal insulation of about 10^{-4} mbar. The pressure is monitored by an Oerlikon Leybold Pennigvac PTR 90, which is installed on a KF25 T-piece together with the SHV feedthrough. In addition, an optical fiber connector (Vacom CF40-FCPC-50-1-DE-ZR) is installed on a T-piece tube of the gas outlet. A double fiber light guide is connected on the inside to bring low intensity light pulses inside the TPC. The fibers have a 300 µm synthetic fused silica core and a numerical aperture of 0.22 ± 0.02. With their length of 150 cm, they can be installed inside the TPC for PMT gain calibration during TPC operation, which will be discussed in chapter 6.

Heat Bridges

The TPC cryostat is mounted on the top flange with four steel rods of 10 mm diameter. For insulation aspects, these rods are thermal bridges leading to a cooling power loss due to heat coming into the system. The heat input $\dot{Q}_{rod}$ can be calculated by

$$\dot{Q}_{rod} = \frac{A}{L} \int_{T_1}^{T_2} \lambda(T) dT, \tag{5.2}$$

where A is the cross section area of the rod, L is the rod length, and $\lambda(T)$[2] is the thermal conductivity. The heat input for one of the used rods with a length of 860 mm at temperatures of 160 K inside and 300 K outside is

$$\dot{Q}_{rod} = \frac{7{,}85 \times 10^{-5}\,\mathrm{m}^2}{0.86\,\mathrm{m}} \cdot (3060 - 1170)\,\mathrm{W/m} = 0.17\,\mathrm{W}. \tag{5.3}$$

For four rods and the two gas lines, which have a smaller cross section than the rods, an overall heat input of less than 1 W can be estimated. The cables going through the insulation give an additional heat input, which is expected to be of the same size or less. Therefore, the estimated maximum heat load due to heat bridges is less than 2 W.

[2] Values for the integral are taken from [Hae81].

Heat Radiation

The absorbed heat input by radiation, $\dot{Q}_{rad}$, can be calculated with the Stefan-Boltzmann law [Hae81]

$$\dot{Q}_{rad} = f A_{ch} e_{ch} \sigma (T_w^4 - T_{ch}^4), \tag{5.4}$$

using the cryogenic surface A_{ch}, its emissivity e_{ch}, the Stefan-Boltzmann constant σ, the temperatures of the vacuum vessel's wall T_w and the chamber T_{ch}, and the geometry and emissivity dependence f. This dependence is given by:

$$f = \frac{1}{1 + A_{ch} e_{ch} (e_w^{-1} - 1)/A_w} \tag{5.5}$$

with the emissivity of the vacuum vessel wall e_w and its surface area A_w.
With the help of the values of the Münster setup, f and $\dot{Q}_{rad}$ can be calculated, whereas the values of the emissivities are estimations:

$$f = \frac{1}{1 + 0.2\,\mathrm{m}^2 \cdot 0.2 \cdot (0.2^{-1} - 1)/1.39\,\mathrm{m}^2} = 0.9 \tag{5.6}$$

$$\dot{Q}_{rad} = 0.89 \cdot 0.2\,\mathrm{m}^2 \cdot 0.2 \cdot 5.67 \times 10^{-8}\,\frac{\mathrm{W}}{\mathrm{m}^2\mathrm{K}^4}((295\,\mathrm{K})^4 - (175\,\mathrm{K})^4) = 13.22\,\mathrm{W} \tag{5.7}$$

Considering these two aspects, the total heat input is roughly 15 W at operation temperature, where the cooling power should be about 91.5 W as shown in figure 5.4. By analyzing data from a cold run with gaseous xenon inside the TPC, the calculated values can be tested. With 91.5 W cooling power just for the refrigerator and 15 W heat input by heat bridges and thermal radiation for the fully installed system, the usable power should be in the range of 76.5 W. Figure 5.5 shows the available cooling power for the running system filled with gaseous xenon. The measured data meets the expectations for the heat introduction very well. Regarding to [Gib11], the required power to cool down and liquefy xenon from room temperature is in the order of 11 W/SLPM. Therefore, the 76.5 W of net cooling power provided in Münster's setup allow a constant xenon liquefaction of 7 SLPM.

Some more information about the TPC filling and recuperation as well as the gas system design is given in chapter 7.

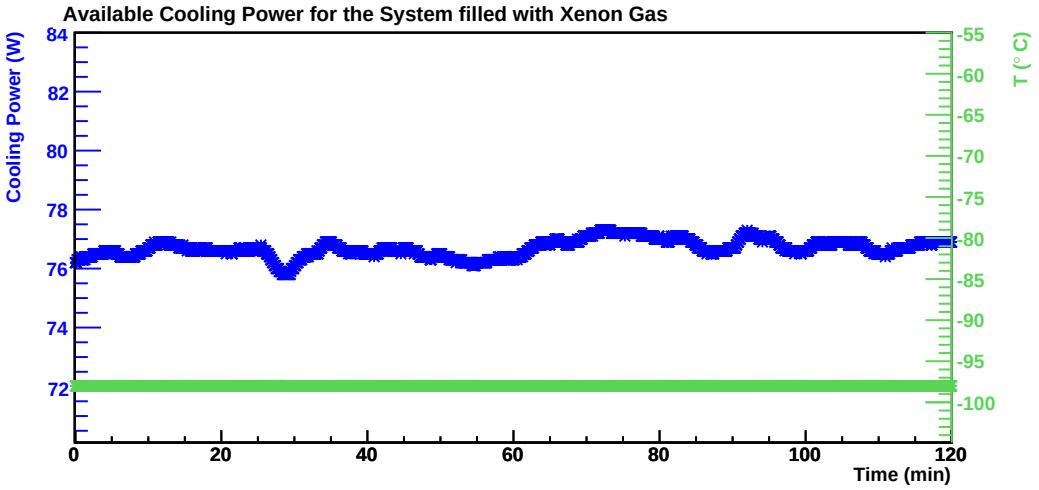

Figure 5.5.: *Cooling power available at run time for the setup filled with gaseous xenon. The temperature set point of this measurement was* $-98\,^{\circ}C$.

6

PMT Calibrations

The readout of the scintillation light signals inside the TPC is done by photomultiplier tubes. The PMT converts photons to charges and multiplies them by using a dynode structure. To be able to characterize the primary interaction by the number of detected photons, the gain of the PMT needs to be known. With knowledge of the gain and data from detector calibration measurements with radioactive sources the energy deposit of the interaction can be determined. Therefore, a gain calibration at room temperature of the PMTs was made before their installation in the TPC and they will be recalibrated in the LXe environment. The used PMT type, the procedure, and the results of the pre-installation calibrations are presented for one PMT (# LV1091) in the following sections.

6.1. Basic Working Principle of a PMT

In a PMT, the conversion of photons into electrons is caused by the photoelectric effect occurring in the photocathode. Because of the applied high voltage on the cathode and on a focusing electrode, the freed charge carrier is accelerated and focused onto a dynode, the first stage of an electron multiplier electrode chain. The dynode emits several secondary electrons for every incoming electron hitting the surface. The emitted electrons are accelerated to the following dynode because of a cascading potential from dynode to dynode. This procedure is repeated for each electrode with a snowballing number of electrons. At the end of the process, the electron avalanche hits the anode, which results in a sharp current pulse. Figure 6.1 shows a sketch of a PMT and the basic functional principle.

6.2. Hamamatsu R8520-06-AL

The XENON Dark Matter Project uses a special PMT developed by Hamamatsu, which is called R8520-06-AL. It is a one inch square detector with a very low radioactivity. The photocathode is made of a bialkali material with an effective area of $(20.5 \times 20.5)\,\mathrm{mm}^2$

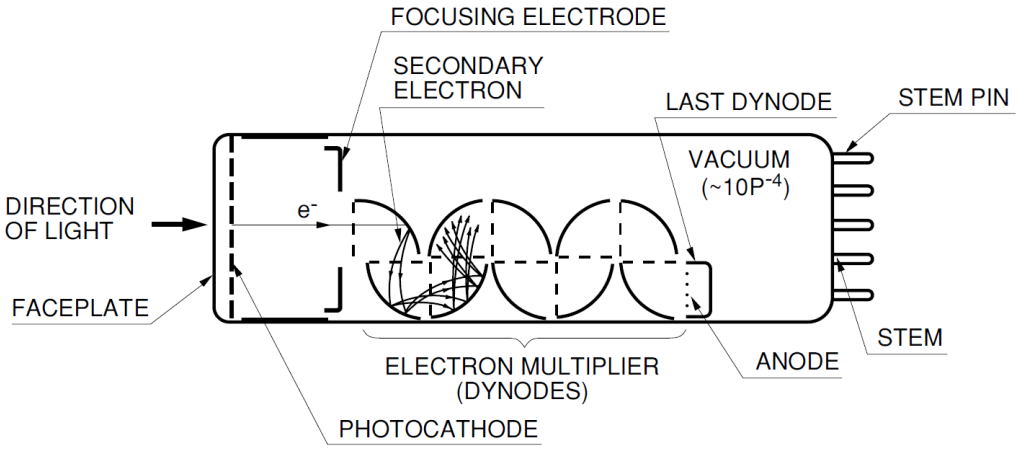

Figure 6.1.: *Sketch of a PMT showing the basic functional principle. Figure taken from [Ham06].*

covered by a synthetic silica glass window, which is transparent to the UV scintillation light from xenon. The photocathode has a spectral response from 160 nm to 650 nm and is optimized for xenon scintillation light at 178 nm with a quantum efficiency of about 30%. The multiplication of charges is done by ten metal channel dynode stages connected with a resistor chain. Concerning the use in a cryogenic system, the allowed environmental conditions are important. The PMTs have an operating temperature range of $(-110 \text{ to } +50)\,^{\circ}\text{C}$ and a maximum pressure resistance of 5 atm. The maximal operation voltage between cathode and anode is 900 V.
The high voltage and signal are connected by a base consisting of an external electronic circuit which sits on a custom made chip, as shown on the right hand side of figure 6.2, that can be mounted to the back of the PMT. In the tests made for this thesis, the base configuration and the applied voltages were negative.

6.3. PMT Gain Calibration

To perform a gain calibration, a PMT is placed in a dark box (see figure A.4 in the appendix) and illuminated with a LED which is used in pulsed operation. The period of light emission is limited to a time slot of only 20 ns and the data acquisition is triggered from the LED power supply. By lowering the light intensity, it is possible to adjust the charge input of the PMT. For the gain calibration, the light intensity is set to a low level where the PMT collects no photon for about 90 - 95% of all light pulses. The number of

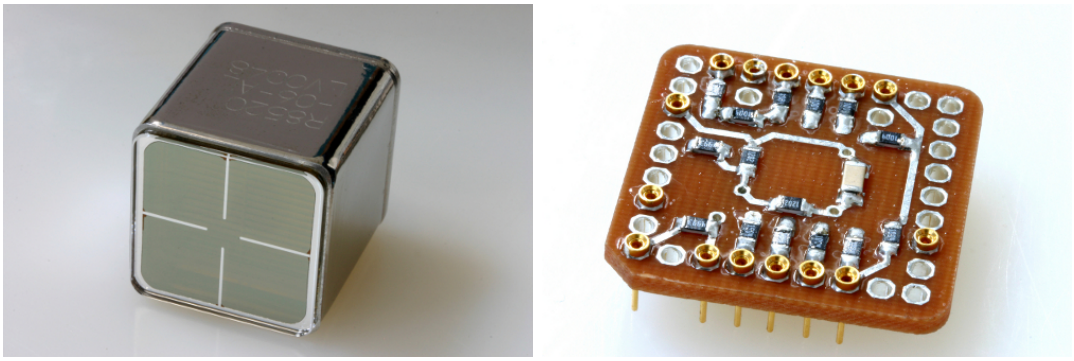

Figure 6.2.: *On the left hand side, the R8520-06-AL PMT is visible. It has a high quantum efficiency and was specially designed for the use in LXe. On the right hand side, there is a picture of the custom made electronic chip supporting the PMT.*

photoelectrons collected then follows a Poisson distribution

$$P_\lambda(k) = \frac{\lambda^k}{k!} e^{-\lambda}, \tag{6.1}$$

where P is the probability distribution of the value k concerning the expected number of occurrences λ. About 4.9 - 9.5% of the light pulses lead then to a single photoelectron event. The fraction of two or multiple photoelectron events is then lower than 0.1 - 0.5%. The data acquisition, which was performed by a Labview controlled Tektronix MDO4000 Oscilloscope, stores the values of the PMT output 200 ns before and after the LED pulse trigger with a frequency of 2.5 GHz. Figure 6.3 and 6.4 show waveforms with and without a photoelectron pulse.

By integrating $U(t)$ over the sample time dt from $t_i = 0$ ns to $t_f = 80$ ns and accounting for the 50 Ω input impedance of the oscilloscope, the charge output of the PMT can be calculated with

$$Q = \int_{t_i}^{t_f} \frac{U(t)}{R} dt. \tag{6.2}$$

This is equal to

$$Q = \sum_{i=1}^{f} \frac{U_i \Delta t}{R}, \tag{6.3}$$

where $f = 200$ is the number of samples considered after the light pulse and $\Delta t = 0.4$ ns is their width.

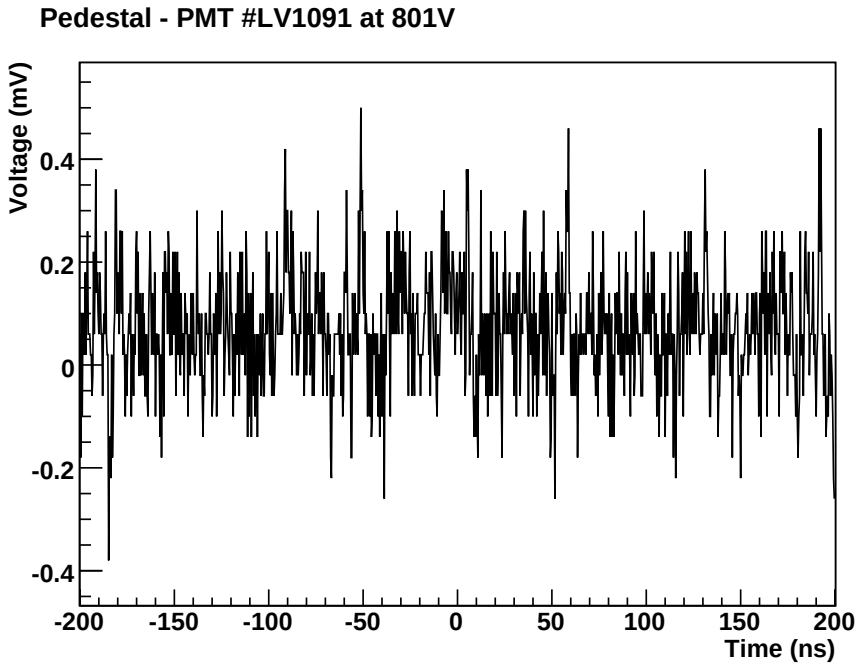

Figure 6.3.: *Waveform showing the voltage corresponding to the output of PMT #LV1091 at U=801 V with just the pedestal measured. The zero on the time scale is defined by the trigger.*

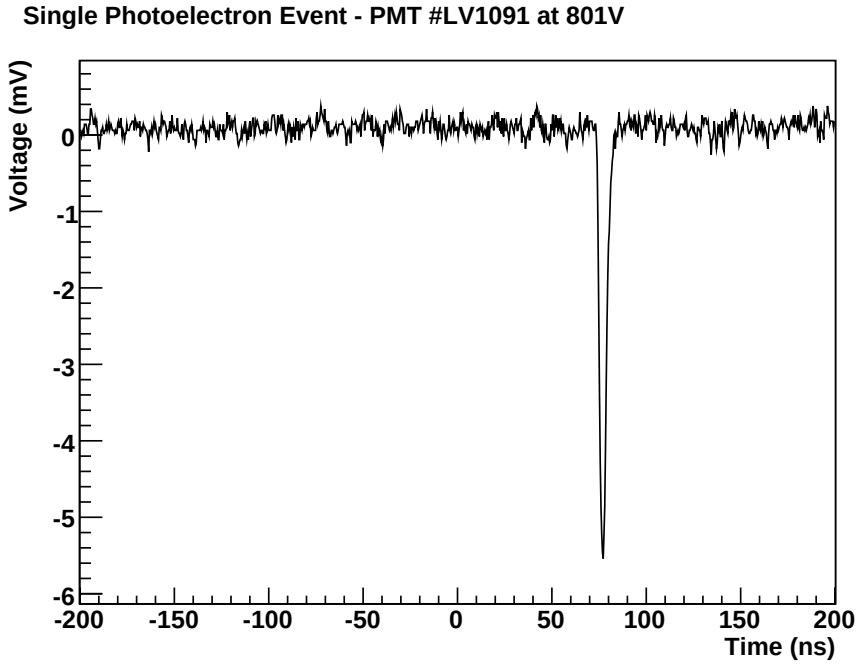

Figure 6.4.: *Waveform showing the voltage corresponding to the output of PMT #LV1091 at U=801 V for a single photoelectron event.*

The total charge output can then be expressed in number of electrons by

$$N_{el} = \frac{Q}{e}. \tag{6.4}$$

6.3.1. Baseline Subtraction

As visible in figure 6.4, the signal shows an offset which is most likely due to the data acquisition process by the oscilloscope. A baseline subtraction is performed for each waveform to remove this offset. For the baseline subtraction, the average electron output N_{el} is calculated over a time window of 200 samples before the trigger. By subtraction of the average value from the whole waveform, the baseline is fixed to zero. This procedure is repeated for each waveform individually to eliminate fluctuations in the baseline offset during the measurement.
The resulting histogram for the electron output of the PMT is shown in figure 6.5. The three peaks for the pedestal where no photoelectron is present and the single (1pe) and double (2pe) photoelectron events are visible.

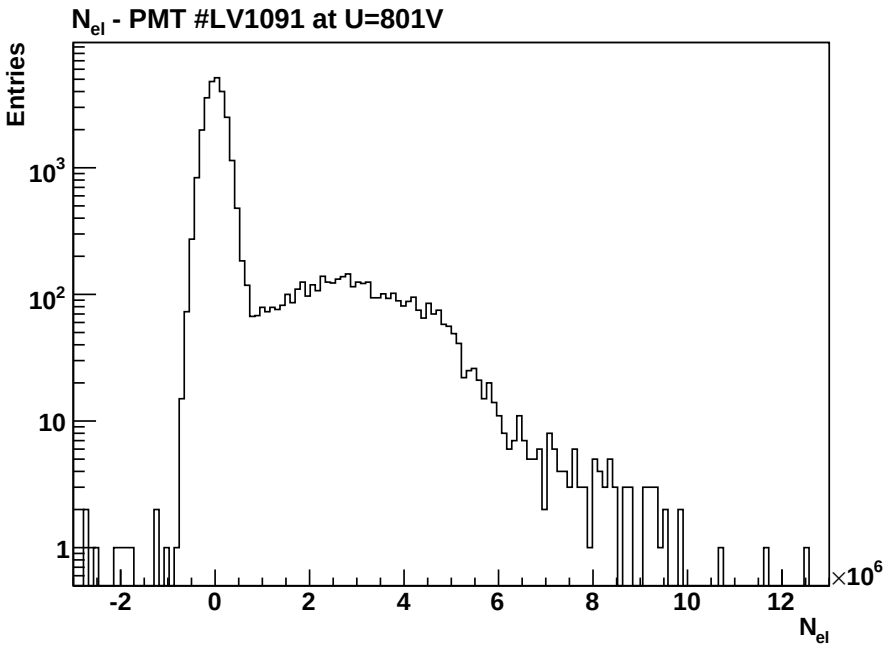

Figure 6.5.: *Histogram for the electron output N_{el} just calculated with the formulas 6.3 and 6.4 considering more than 29,000 raw waveform data sets. The three visible peaks are due to the pedestal, to single photoelectron events, and to two photoelectron events (from left to right). Before plotting, a baseline subtraction was performed.*

The actual gain is then the mean value of the 1pe peak because this is the number of electrons created in the avalanche induced by one photoelectron and it can be obtained by fitting the spectrum with the single electron response (SER) function.

6.3.2. Single Photoelectron Fit

The form of the SER function is assumed to be a sum of Gaussian functions, one for the pedestal and one for each photoelectron concentration. A simplified SER function ignores the small component from two or more photoelectrons and is given by

$$g_2(x) = a_n \cdot \exp\left(-\frac{(x-x_n)^2}{2\sigma_n^2}\right) + a_{1pe} \cdot \exp\left(-\frac{(x-x_{1pe})^2}{2\sigma_{1pe}^2}\right), \tag{6.5}$$

where a_i is the amplitude, x_i is the mean, and σ_i is the width.
Figure 6.6 shows the result of fitting the spectrum with equation 6.5, yielding a gain of $(2.6885 \pm 0.0346) \times 10^6$ for PMT #LV1091 at U=801 V. A lower bound on the error is obtained from the error estimated by the fitting routine.

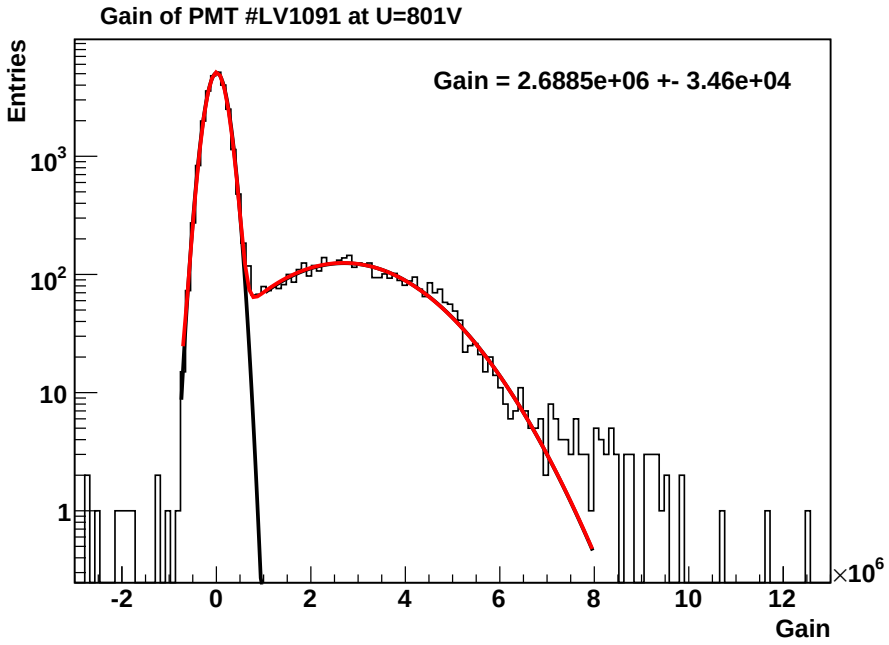

Figure 6.6.: *Histogram showing the simplified SER function fit used to determine the gain. The two initial fits are shown in black, they offer the initial parameters for the double Gaussian fit shown in red. The mean value of the 1pe peak is the gain.*

6.3.3. Single and Double Photoelectron Fit

For high statistics or a rather high light intensity, the 2pe peak becomes more important for the gain calibration. Due to an overlap of the 1pe with the 2pe peak, the gain will be shifted to higher values if equation 6.5 is used in this case.
The influence of the 2pe peak can be included using the more general SER function given by

$$g_3(x) = a_n \exp\left(\frac{(x-x_n)^2}{-2\sigma_n^2}\right) + a_{1pe} \exp\left(\frac{(x-x_{1pe})^2}{-2\sigma_{1pe}^2}\right) + a_{2pe} \exp\left(\frac{(x-x_{2pe})^2}{-2\sigma_{2pe}^2}\right), \quad (6.6)$$

where a third Gaussian function is added to the sum. Fitting a spectrum with this three Gauss SER function is not trivial because of the nine free parameters. If a fit routine has too many free parameters, it can produce fits with a very small χ^2, but with parameters in regions without physical meaning. Therefore, constraints are used to set limits on the parameter space assuring physically reasonable results.
Because of the linearity of the PMT, the means of the 1pe and the 2pe peaks are related by

$$x_{2pe} = 2\ x_{1pe}, \quad (6.7)$$

and the widths of the two peaks are linked by Gaussian statistic like

$$\sigma_{2pe} = \sqrt{2}\ \sigma_{1pe}. \quad (6.8)$$

With these constraints, the SER function becomes

$$g_3(x) = a_n \exp\left(\frac{(x-x_n)^2}{-2\sigma_n^2}\right) + a_{1pe} \exp\left(\frac{(x-x_{1pe})^2}{-2\sigma_{1pe}^2}\right) + a_{2pe} \exp\left(\frac{(x-2x_{1pe})^2}{-4\sigma_{1pe}^2}\right), \quad (6.9)$$

and only seven free parameters are left over. Figure 6.7 shows the result of fitting the same spectrum as before with equation 6.9, yielding a gain of $(2.6538 \pm 0.0360) \times 10^6$, which is 1.3% smaller than the value determined with the simplified SER function.

As an intermediate result of this investigation, a systematic error of 1.3% will appear in the gain calculation if the 2pe peak is not considered for high statistics of 30,000 waveforms. The systematic error and the impact of statistics is discussed in the following section in more detail.

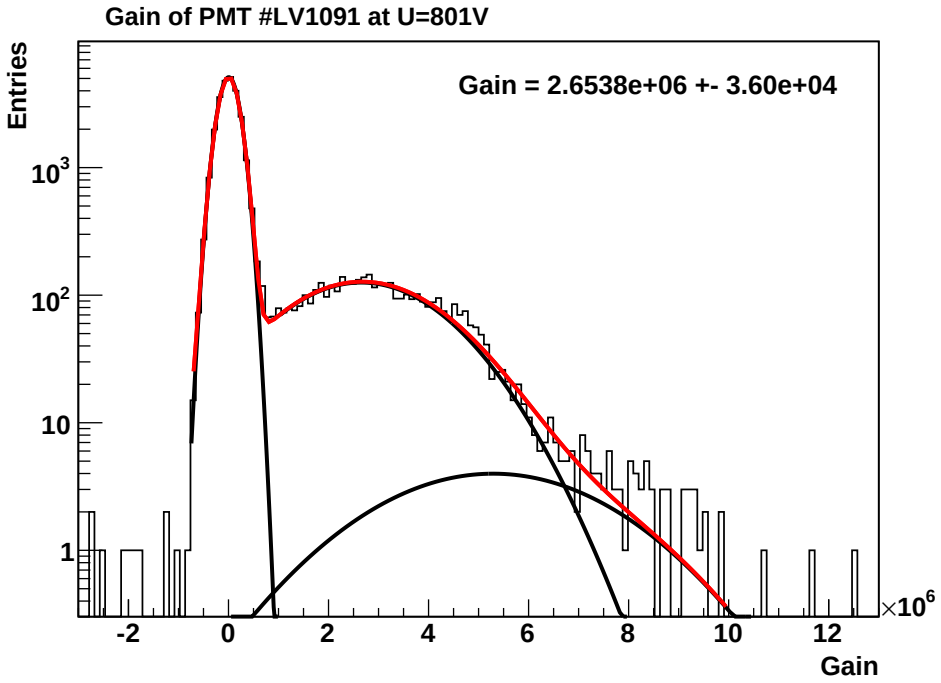

Figure 6.7.: *Histogram showing the SER function fit used to determine the gain considering the 2pe peak. The three initial fits are shown in black, they offer the initial parameters for the triple Gaussian fit shown in red. The mean value of the 1pe peak is the gain.*

6.3.4. Discussion of Systematic Errors

In addition to the results from section 6.3.3, it is investigated if the gain has a dependence on the number of events measured. Therefore, parts of the data set used in the previous analysis are taken to determine the gain for different amounts of statistics. Figure 6.8 shows the results for both fit methods taking 5,000 to 30,000 waveforms into account. The observed behavior is similar for both fit methods. The gain is relatively low for 5,000 events, increases than to the maximal measured value for 10,000 events and decreases then slightly again, settling at a stable value for 15,000 events and more. The uncertainties decrease with higher statistics from step to step. All determined gain values are in agreement within their errors and no major dependence of the number of waveforms is observed. Nevertheless, it can be stated that the number of events should be greater than 15,000 to achieve an uncertainty given by the Gaussian fits of smaller than 2%.

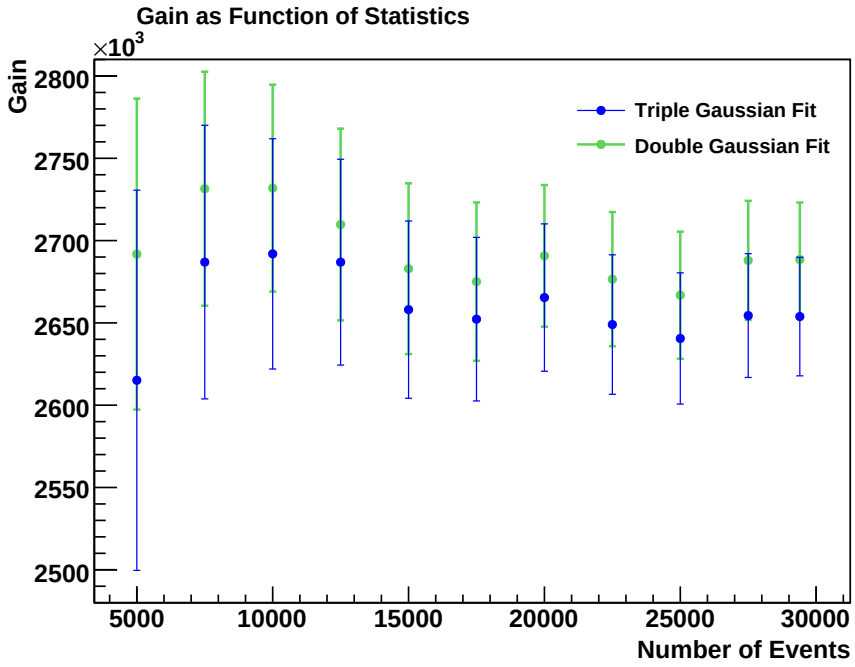

Figure 6.8.: *Plot of the gain, determined with both fit methods, as function of the number of events. The shown uncertainties are the uncertainties of the mean of the 1pe peak given by the SER function.*

Next, the systematic error introduced by using equation 6.5 compared to equation 6.9 for the SER function is investigated. The systematic error from using equation 6.5 is taken as

$$\text{systematic error} = \frac{|\text{gain}(3\,\text{Gaussian}) - \text{gain}(2\,\text{Gaussian})|}{\text{gain}(3\,\text{Gaussian})} \cdot 100\,. \tag{6.10}$$

Figure 6.9 shows this estimation of the systematic error as a function of the number of events acquired. The systematic error is independent of the number of events, with the exception of the 5,000 event data point, which, while the deviation is slightly higher, still agrees within the error bars. The mean value for the systematic error for 10,000 and more events is 1.1%. In further gain calibrations, equation 6.5 was used for the SER function, but with this systematic error included.

6.3.5. Gain versus High Voltage

The knowledge of the gain of each PMT for one high voltage setting is enough to calculate the number of photoelectrons from its charge output individually for each tube.

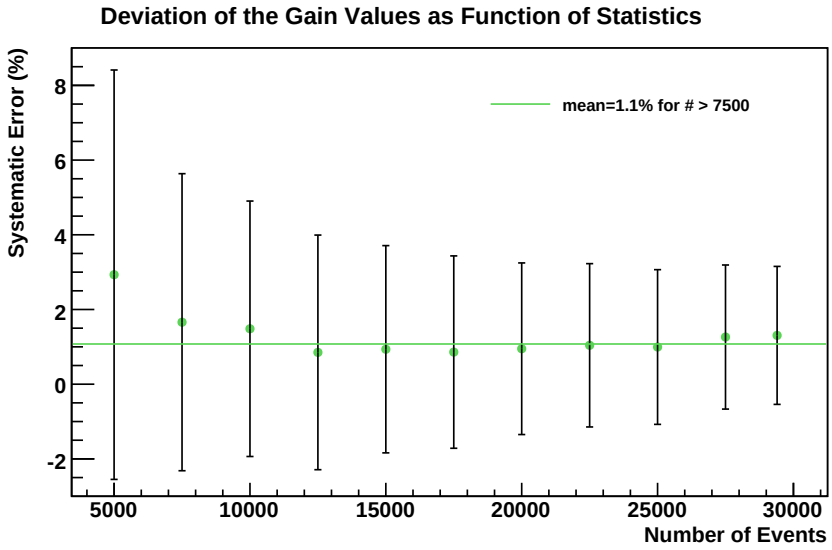

Figure 6.9.: *Plot of the deviation of the gain determined by simplified and normal SER function fits as function of statistics. The shown uncertainties are calculated from the uncertainties of the gain values and for the mean value the deviations for 10,000 and more events are taken into account.*

Nevertheless, it is useful for the operation of a detector with several PMTs to set all of them to the same gain value, which can be achieved by applying different voltages to the tubes. Therefore, the response of the gain as function of the supplied voltage is measured and fitted with a power law as shown in figure 6.10. The resulting fit function can be used to find the high voltage value that is related to a certain gain as

$$\text{gain} = A \cdot V^{kn}, \tag{6.11}$$

where A is a constant, V is the applied voltage, n is the number of dynode stages, and k is a constant determined by the structure and material of the dynodes.

A common gain has the advantage to be able to define a dynamic range that is similar for all PMTs. The lower limit of this range is given by the requirement to resolve single photoelectrons, the upper limit is given by the appearance of non-linear response of the PMT for large currents. Known by the results of former research and experiences from XENON100, a common gain value of 2×10^6 is reasonable.

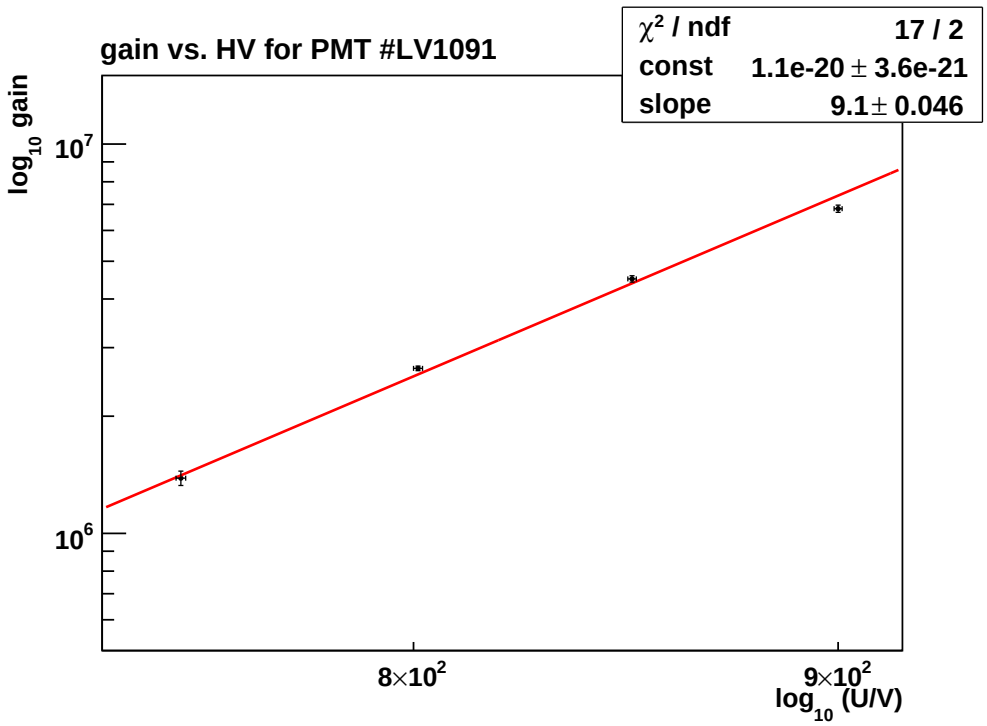

Figure 6.10.: *Plot of the gain as function of supplied high voltage. The data points are fitted with a power law (see equation 6.11) and the applied voltages were 750 V, 800 V, 850 V, and 900 V. All gains were determined by calibration using more than 15,000 single waveforms.*

6.4. Dark Counts

If a PMT is used for the detection of events with a very low rate, the dark counts of the PMT will become an issue. Dark counts are event-like outputs of the PMT where no initial photon from the observed source hit the tube. The main source of dark counts is thermionic emission of electrons from the photocathode.

The number of dark counts can be measured by operating the PMT in a dark box without any light source. Because of time constraints, the data from the gain calibrations were reused, as opposed to performing a dedicated measurement. The pre-trigger region, before the LED is turned on, was analyzed to look for dark counts. The number of dark counts identified divided by the whole time taken into account for the analysis gives the dark count rate. In this examination, 35 dark counts were found in a total time of 5.88 µs giving a dark count rate of 5.95 kHz, which is likely a cross over estimation. Therefore, a dedicated measurement for the dark count rate should be performed soon.

In addition to measuring the absolute dark count rate, it is possible to determine the rate as function of the corresponding number of photoelectrons. This just requires a peak finding algorithm that is able to determine the number of electrons produced by the event as it is done in the equations 6.3 and 6.4.

7

Functional Demonstrations

After the assembling process, performance tests were made to demonstrate the functional capability of the TPC and the infrastructure. Two different kinds of checks were performed, one concerning aspects related to the gas handling, the other one dealing with the actual proof of detector operation.
The conclusion of the gas handling trails are included in a brief presentation of Münster's gas system and the three basic operation modes. For the functional demonstration of the TPC, waveforms showing S_1 and S_2 signals in delayed coincidence are cited as evidences.

7.1. Gas Handling

As outlined in chapter 4, the Münster TPC is integrated in a gas system including a purification cycle. These two structures are used for the filling and recuperation of xenon into and from the TPC. The gas system itself and how it is ran for TPC filling, recuperation, and xenon purification is briefly discussed in the following sections. A detailed description of the gas system and its parts as well as the maintenance of the TPC can be found in [Ros11].

7.1.1. Gas System

The central element of the gas supply unit is a piping system to which all other components are connected. The pipes are basically arranged like a big P, equipped with automatic (PV) and hand valves (MV), flow controllers (FC), pressure sensors (P), vacuum pump ports (V), and a KNF gas pump, as shown in figure 7.1. The gas storage facility is at the straight end of the P, and the TPC, the getter, and the planned krypton removal column are connected to the ring by bypasses, whereas the quadrupole mass spectrometer is installed on a single line. The bypasses allow to activate or deactivate parts separately without effecting each other. Because of a valve between the lines of the bypasses (e.g. PV8 in case of the getter), it is possible to guide the whole gas through the components if necessary. For purity reasons, the inner surface of the tubes is electropolished and all welded connections are performed by orbital welding. To adapt the

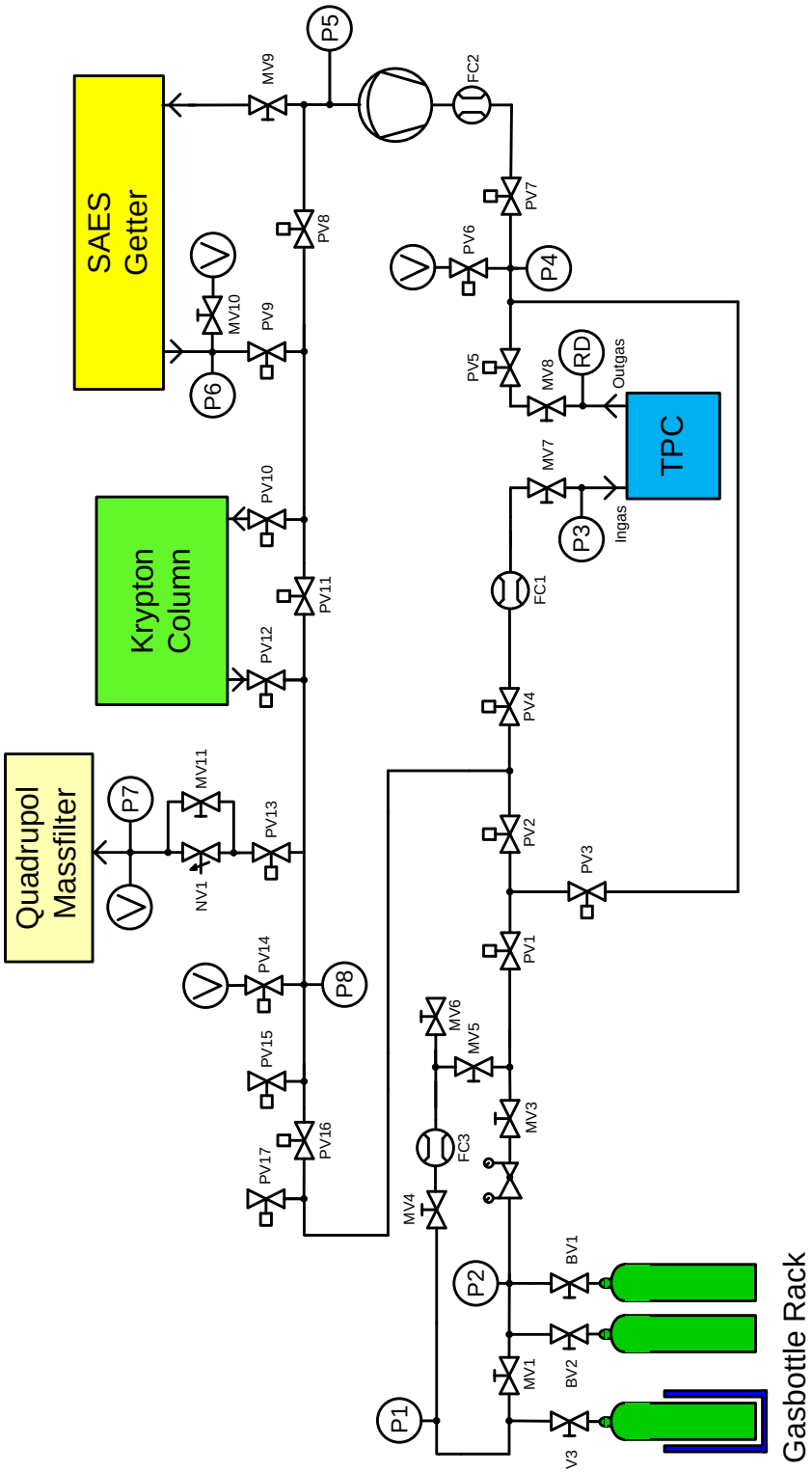

Figure 7.1.: *Sketch of Münster's xenon gas system including the five big components which are the gas bottle rack, the TPC, the getter, the planned krypton distillation column and a quadrupole mass spectrometer. These main parts are connected by gas lines, which are shown as well as all valves, sensors, controllers, and vacuum ports. Figure taken from [Ros11].*

system to high flow rates, 1/2 inch tubes are used.
The system is controlled by a Labview based software installed on an autarkic National Instruments CompactRIO embedded control and acquisition system which can be operated automatically with installed programs, or manually over a control panel.
Before xenon gas is introduced, the system is pumped out by a turbo molecular pump over several pump ports. Nevertheless, a considerable quantity of impurities remains in the pipes and vessels on the surfaces and in the residual gas. To remove this residual contamination the whole system would have to be baked out during the pumping process. Due to the limited heat resistance of the PMTs (50 °C), this is not possible for the TPC. Therefore, the pipes are baked out and the TPC is only evacuated without heating and filled with xenon afterwards. Getting in contact with xenon, the impurities mix up with it and can be filtered out of the xenon by the hot getter. To reach the necessary purity, the xenon has to be cleaned for several days after each detector opening in advance of proper operation.

7.1.2. TPC Filling

To fill the TPC with liquid xenon, it is gaseously introduced into the system and then cooled down and liquefied in the cooling tower.
Before the filling process starts, the cold finger is pre-cooled to about -98 °C. When this temperature is reached, the valves on the way from the bottle rack to the TPC are opened and the pressure regulator is set to about 2.7 bar. With help of the flow controllers FC1 and FC2, it is then possible to define the flow rate of the xenon gas streaming into the chamber to be 2 SLPM higher than the one of the outflow. This means that gas has to stay inside the cooling tower, where it is cooled down and liquefied at some point. With the liquid xenon produced in the cooling tower, the TPC itself is cooled by drops which run down the tube where they vaporize again and suck heat out of the system. The gaseous xenon is liquefied at the cold finger again and heat is transported out of the system by this procedure.
When the TPC is cold enough, the liquid starts to fill up the TPC vessel and when the cold liquid touches the temperature sensor near the bottom of the Teflon stack, a temperature drop is registered there. At the position, where the temperature sensor is mounted, the level sensors start. Therefore, they register an increasing level after this drop. Figure 7.2 shows the temperature at the bottom of the TPC and the level sensor output when the liquid reached the sensors. The drop on the TPC temperature sensor

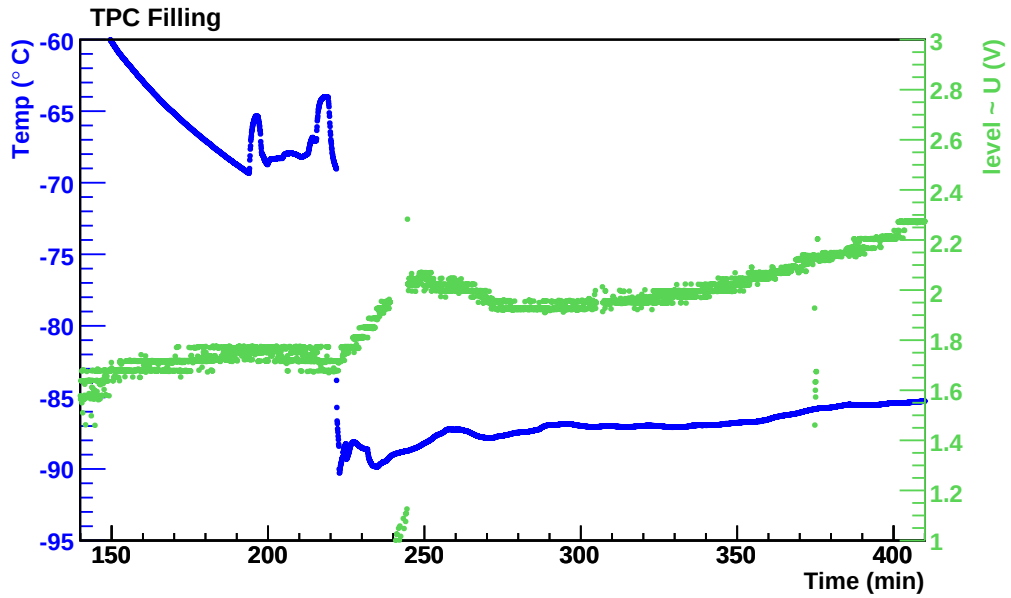

Figure 7.2.: *Temperature and level measurement during the filling process. The TPC bottom sensor registers a drop in temperature when it gets in contact with the liquid and the level sensor indicates an increasing level.*

is clearly visible. The small bump in the level measurement right after the temperature dip is most likely due to a change in capacitance of the level sensors because of different thermal contraction of the two electrodes when they come in contact with the liquid.
At the moment of the dip, the pressure inside the TPC was 2.67 bar, which corresponds to a liquefaction temperature of $-89.15\,^{\circ}\mathrm{C}$. During the remainder of the filling process, the pressure inside the TPC increased together with the xenon liquefaction temperature explaining the slowly increasing temperature.
The two pressures P3 and P4 were uncritical over the whole filling process and it was possible to stabilize them after the filling was completed. As discussed in chapter 3, the TPC has to be filled until the liquid level is between the gate mesh and the anode, which can be monitored by the level sensors. After a short run-in period, it was possible to control the filling procedure accurately, whereas the determination of the precise level still has to be fine tuned. One proposal for that would be to add an additional temperature sensor at the height right between the two meshes so that the sharp temperature drop will identify when the liquid has reached the correct level.

7.1.3. Xenon Recuperation

An efficient xenon recuperation procedure is required to be able to empty the chamber in an adequate space of time. This can be necessary for service on the chamber or the gas system and it is indispensable in case of an emergency, e.g. a failure of the cryocooler. The basic principle of recuperation is to create an underpressure in the gas bottle that sucks the xenon out of the TPC. Therefore, the bottle is cooled down by placing it in liquid nitrogen, pictured by the blue bucket around the left bottle in figure 7.1.
In addition to the normal recirculation, the valves back to the gas bottle rack are opened using the way though the flow controller FC3, which is set to 5 SLPM. During the recuperation process, the pressure and therefore the temperature inside the TPC decreases and it has to be monitored to avoid freezing inside the TPC. When the temperature drops, the heat load to the system has to be increased, which can be done by an additional heater inside the TPC bottom flange or by breaking the insulation vacuum. At some point, the pressures inside the bottle and the TPC are nearly equalized and the xenon flow is no longer driven properly. Therefore, a small amount of xenon remains in the chamber.
The procedure of recuperation was tested a few times before long term operation to investigate conceptional problems which could have dramatical consequences in case of an emergency. At the end, a reliable routine was established which allows to empty the TPC on a reasonable time scale.

7.1.4. Normal Operation and Xenon Purification at Run Time

For normal detector operation, the xenon is cleaned at run time to guarantee a constant low impurity level in the TPC. For the purification process, gaseous xenon is taken out of the cryostat, pumped through the getter, fed into the cooling tower, liquefied, and filled back into the Chamber.
To run the purification, the xenon is pumped around the main cycle and in addition the whole flow is guided through the getter. By starting the pump and the getter, the purifying process begins.
This is the standard operation mode while the TPC is filled and was performed stably over several weeks to reach an adequate low level of impurities for TPC test purposes.

7.2. TPC Operation Test

In preparation of the TPC operation test, the chamber was filled with liquid xenon to a level between the central screening mesh and the anode. To be able to drift electrons, the purity of the xenon had to be increased dramatically and therefore a continuous purification was performed by pumping the gas through the hot getter for about two weeks.

For the actual test, the TPC was equipped with two PMTs, one on top, one at the bottom of the TPC. Both PMTs were placed in the central spots and supplied with $-800\,\mathrm{V}$. The electric fields were created by applying a voltage of $-8\,\mathrm{kV}$ to the cathode and $+4\,\mathrm{kV}$ (max. output of the used power supply) to the anode, which gives a drift field of E_d=471 V/cm and an extraction field of E_{ex}=8 kV/cm. To generate a reasonable number of events, the detector was exposed to electron recoils from a ^{60}Co source, which provides gamma rays of 1.17 MeV and 1.33 MeV .

For the data taking process, a trigger was set to about $-20\,\mathrm{mV}$ which is lower than a typical one photoelectron signal. In addition, it was linked to both PMTs, which means if one PMT produces a signal bigger than the trigger value, the output of both PMTs will be stored on hard drive.

Figure 7.3 shows a typical event where the interaction took place in the liquid phase. The small S_1 signal, which is most likely produced by an electron recoil event, is clearly visible on both PMTs. Normally, it would be expected to see most of the prompt scintillation light on the bottom PMTs because around eighty percent of the light is reflected at the liquid surface due to total reflection. Whereas, in a system with a high impurity level, the attenuation length for light is small and if the event happens in the region next to the surface, much light will be absorbed on the way through the TPC. After the drift time, the electrons were extracted and accelerated causing a proportional scintillation light signal S_2 while moving through the gaseous xenon to the anode mesh. This signal is much higher than the S_1 signal because in the primary interaction several electrons were produced, especially if it was an electron recoil event. Furthermore, the S_2 signal is much broader because the electrons produce light as long as they are traveling through the gas phase until they reach the anode.

The shown waveforms corresponds to the expectation for an electron recoil event happening in a dual phase xenon TPC. Therefore, this and similar waveforms taken during the test run can be seen as **the proof of a successfully designed and installed dual-phase time projection chamber**.

Considering the waveforms in figure 7.3, the drift length can be calculated by the time between the S_1 and the S_2 signal. In this case, it is in the order of 20 ns, which corresponds to a drift length of about 4 cm with a drift velocity of roughly $v = 2\,\mathrm{mm/\mu s}$ [Apr09].

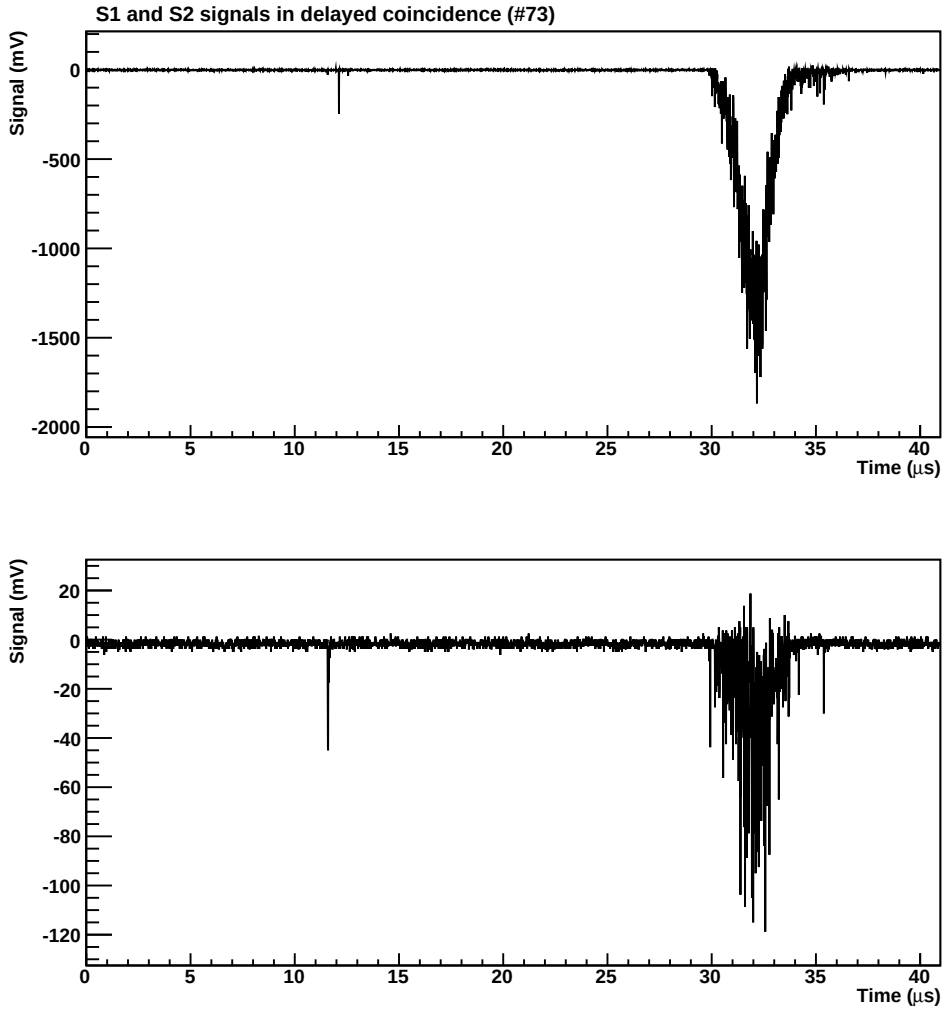

Figure 7.3.: *Waveforms taken during the detector test measurement. The top plot shows the output of the top PMT, the bottom plot the output of the bottom PMT. The waveforms show the S_1 and S_2 signal in delayed coincidence on both PMTs which is typical for waveforms acquired in a dual phase TPC.*

One of the longest drifts observed in this measurement is shown in figure 7.4. With a drift time of about 30 µs, a drift length of 6 cm can be estimated for this event, which is already 1/3 of the total possible drift length.

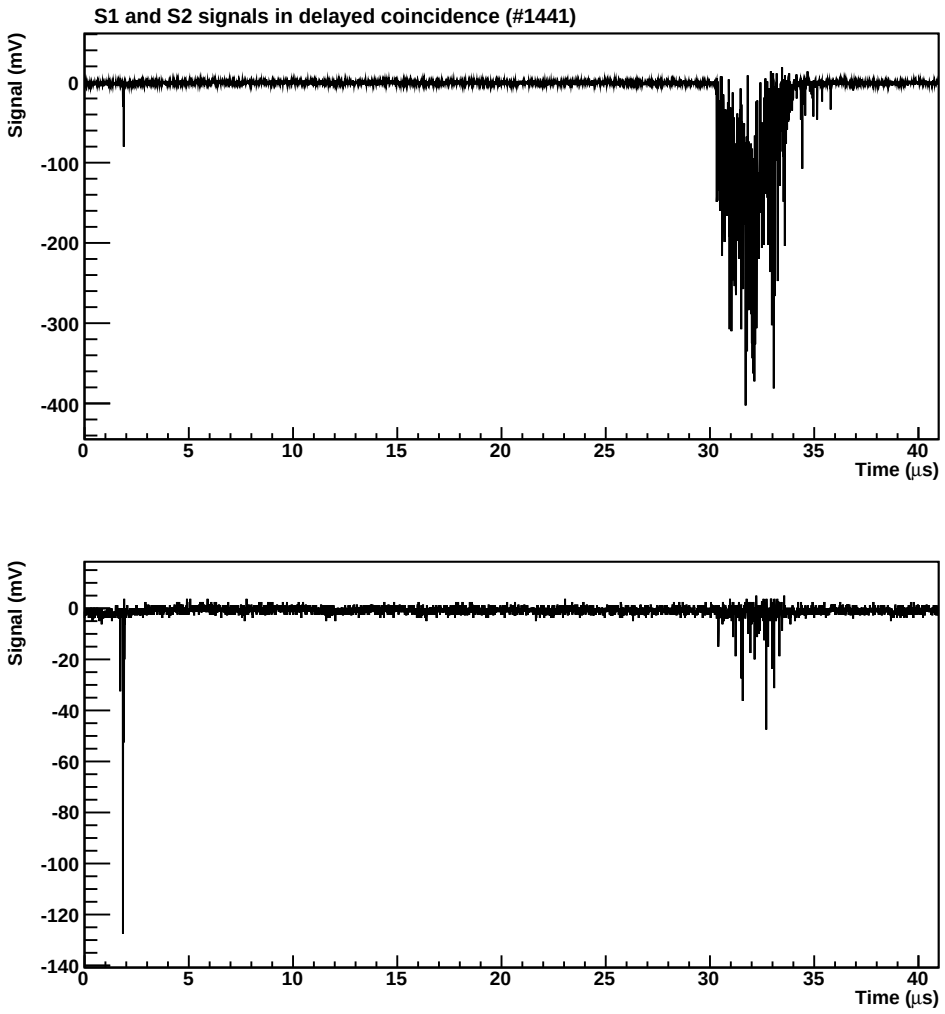

Figure 7.4.: *Analog to figure 7.3, the waveforms of S_1 and S_2 signals in delayed coincidence are shown. The delay appearing in the waveform is one of the longest measured during the test and corresponds to an electron drift length of about 6 cm.*

The results of this first functional check are very promising with regard to the detector design as well as the cleaning capability of the purification cycle.

Conclusion and Outlook

The mechanical and electrical design of a TPC is challenging because many aspects that are crucial for proper operation have to be considered during the planning phase. Mainly the requirements of ultra high purity, low radioactivity, high voltages, and low temperatures constrain the design and raise problems from the mechanical and electrical point of view. Nevertheless, answers to all of these problems were found during the work for this thesis.

The basic design frame was adapted from the working detectors of the XENON Project, but everything had to be conformed and resized to the specific setup. At the end, a 2.6 kg containing TPC with a height of 170 mm and 80 mm diameter was realized which is housed inside a stack of 23 mainly unique Teflon slices. These slices make up the whole bodywork with all installations (PMTs, meshes, electrodes, resistors, temperature, and level sensors) integrated in grooves and cavities to reduces the dead volume in the TPC cryostat to a minimum.

Special importance was given to the electric field design which was optimized by simulations. A simulation was used to fine tune the drift field homogeneity and in addition the results of a field simulation around the cathode mesh were adapted to the hardware design avoiding spark discharging which is a limiting factor for XENON100 detector operation.

Equipped with two arrays of 7 UV-sensitive PMTs each, the detector will be able to perform a 3D position reconstruction of the interaction position. For the first test measurement, only two of these PMTs were installed in the TPC and before that, calibration measurements were performed in a dark box to determine the gain as function of the applied HV. This allows to set the gain of all installed PMTs to a common value simplifying recoil energy determination of the events.

To reduce the heat input to the system from conduction and convection from the surrounding medium, the TPC is installed in an insulation vacuum vessel. In addition to the TPC cryostat, the cooling tower where the xenon is liquefied is also housed in this vessel. Various tests showed that the cooling works sufficiently. The provided cooling power allows liquefaction at run time and the temperature control is very stable.

Integrated in Münster's gas system, the three important procedures in context of TPC operation which are filling, purification, and recuperation were demonstrated in repro-

ducible processes.
The actual functional proof of the detector itself was given by taking electron recoil data with gamma rays from a ^{60}Co source where the waveforms showed the typical characteristics of events acquired inside of a dual phase TPC.

Based on the results of this thesis, the work will be continued to fully build up, understand, and characterize the detector and to be able to operate it in the desired way.
First of all, the number of PMTs should be increased to 14 total as this is essential for proper 3D event localization. In the next step, these 14 PMTs will be re-calibrated in the liquid xenon environment with help of the integrated light guide to set them to a common gain value. In case of TPC opening, it could be worthwhile to integrate an additional temperature sensor for leveling purposes. The fully equipped TPC has then to be calibrated in different procedures where mainly two calibration measurements are required for further operation. One is an energy calibration of the detectors response to gamma- and neutron-radiation which can be performed with radioactive calibration sources. The other one is a position reconstruction calibration that is needed to perform the demanded 3D event localization.
When the TPC is ready for real operation, it will be used as a purity monitor by measuring the electron drift length. Integrated in the gas system, these measurements will be an important indicator for the efficiency of the purification process.
Another field of operation will be testing the performance of the planned krypton distillation column. For this, the TPC can be used as an detector for decays of ^{83m}Kr that is mixed into the xenon.
In addition to these main tasks, a lot of R&D for XENON1T and other future dark matter detectors can be performed and a fully working dual phase TPC is certainly an interesting tool for research in other fields like medical imaging.

Zusammenfassung und Ausblick

Aus technischer Sicht ist die Planung einer TPC eine Herausfordeung, da unterschiedlichste Faktoren für ihre Funktionsweise maßgeblich sind. Außerdem schränken die Forderungen nach extremer Reinheit, geringer Radioaktivität, hoher Spannung und niedriger Temperatur die Konstruktionsmöglichkeiten ein und führen zu Schwierigkeiten hinsichtlich der meachnischen und elektrischen Umsetzbarkeit. Dennoch wurden im Rahmen dieser Diplomarbeit Lösungen für alle auftretenden Probleme gefunden.
Die Grundkonstruktion, der bereits existierende Detektoren des XENON Projektes als Vorbild dienten, wurde mit individuell entwickelten Bauteilen ausgebaut und durch Detaillösungen vervollständigt. Schlussendlich wurde ein 2,6 kg Xenon fassendes Detektorvolumen mit 170 mm Höhe und 80 mm Durchmesser realisiert. Die Driftkammer ist dabei in einem zylindrischen Körper aus Teflon integriert, der aus 23 Scheiben zusammengesetzt ist. Mit Hilfe des Teflons wird einerseits eine hohe Reflektivität an den Wänden der Kammer gewährleistet, andererseits dient es auch zur Reduzierung des Totvolumens innerhalb des Detektorkryostaten. Alle mechanischen und elektrischen Bauteile, die zum Betrieb der TPC benötigt werden, sind in Nuten und Aussparungen untergebracht.
Besonderer Wert wurde während der Planungsphase auf Form und Stärke der elektrischen Felder gelegt, die durch Simulationen optimiert werden konnten. Eine dieser Simulationen diente der Geometrieanpassung um ein möglichst homogenes Driftfeld zu erzeugen. Außerdem wurde in einer zweiten Simulation der Bereich um die Kathode hinsichtlich der maximal auftretenden elektrischen Feldstärke untersucht und die Konstruktion ensprechend angepasst um Funkenbildung, wie sie im XENON100 Detektor auftritt, zu verhindern.
Ausgestattet mit zwei Detektorfeldern bestehend aus je sieben Photomultipliern wird die TPC in der Lage sein die Position eines Ereignisses im Detektorvolumen dreidimensional zu rekonstruieren. Für die erste Testphase wurden nur zwei Photomultiplier eingebaut, die zuvor kalibriert wurden um ihren jeweiligen Verstärkungsfaktor und dessen Abhängigkeit von der angelegten Versorgungsspannung zu ermitteln. Durch die Bestimmung dieser Abhängikeit für jeden einzelnen PMT ist es möglich, alle PMTs auf einen gemeinsamen Verstärkungsfaktor zu setzen, was spätere Auswertungen erheblich erleichtert.

Da jeder Wärmeeintrag ins System die für die Xenon Kondensation zur Verfügung stehende Kühlleistung verringert, ist der TPC-Kryostat zusammen mit der Verflüssigungseinheit in einem Isoliervakuum eingeschlossen. Verschiedene Tests des Kühlsystems ergaben, dass dieses genug Leistung bietet um Xenon während des laufenden Betriebs zu verflüssigen. Außerdem konnte eine sehr gute Temperaturstabilität im Langzeitbetrieb gezeigt werden.
Die TPC wird in Münster in Kombination mit dem Prototypen für das XENON1T-Gassystem betrieben und die drei Hauptfunktionen Füllen, Reinigen und Rückführen konnten erfolgreich und reproduzierbar vorgeführt werden.
Der Nachweis der vollständigen Detektorfunktion wurde schließlich durch Messungen mit einer ^{60}Co Quelle erbracht, bei denen die für zwei-Phasen TPCs charakteristischen Signalformen aufgenommen werden konnten.

In dieser Arbeit wurde eine funktionsfähige zwei-Phasen TPC gebaut, die im Weiteren noch vervollständigt und weitergehend charakterisiert werden sollte um ihr volles Potenzial auszuschöpfen.
Als erstes ist es sinnvoll die Anzahl der PMTs auf 14 zu erhöhen, um dreidimensionale Positionsrekonstruktionen durchführen zu können. In diesem Zusammenhang werden alle 14 Photomultiplier einer Rekalibrierung unterzogen, um bei jedem eine einheitliche Verstärkung einstellen zu können. Im Zuge des Ausbaus könnte zusätzlich noch ein Temperatursensor auf Höhe des erforderlichen Füllstands eingesetzt werden.
Die vollständig aufgebaute TPC muss dann zum einen mit γ-Strahlung und Neutronen bezüglich der Energien kalibriert werden, zum anderen muss auch eine Kalibration zur Positionsbestimmung durchgeführt werden.
Schlussendlich soll die TPC als Monitor für die Reinheit des Xenons benutzt werden. Die Messung des Anteils an elektronegativen Verunreinigungen wird dabei über die Bestimmung der Driftlänge erfolgen.
Als zweites Einsatzgebiet ist die Effizienzkontrolle der geplanten Krypton-Destillationssäule vorgesehen, bei der die TPC als Detektor für Zerfälle von ^{83m}Kr genutzt wird.
Zusätzlich zu diesen beiden Hauptaufgaben wird die TPC als Forschungs- und Entwicklungsaufbau für XENON1T und weitere Projekte zur Suche nach Dunkler Materie dienen. Außerdem ist eine voll funktionsfhige TPC ein interessantes Instrument für Forschung in anderen Bereichen wie z.B. medizinische Bildgebung.

A

Technical Drawings

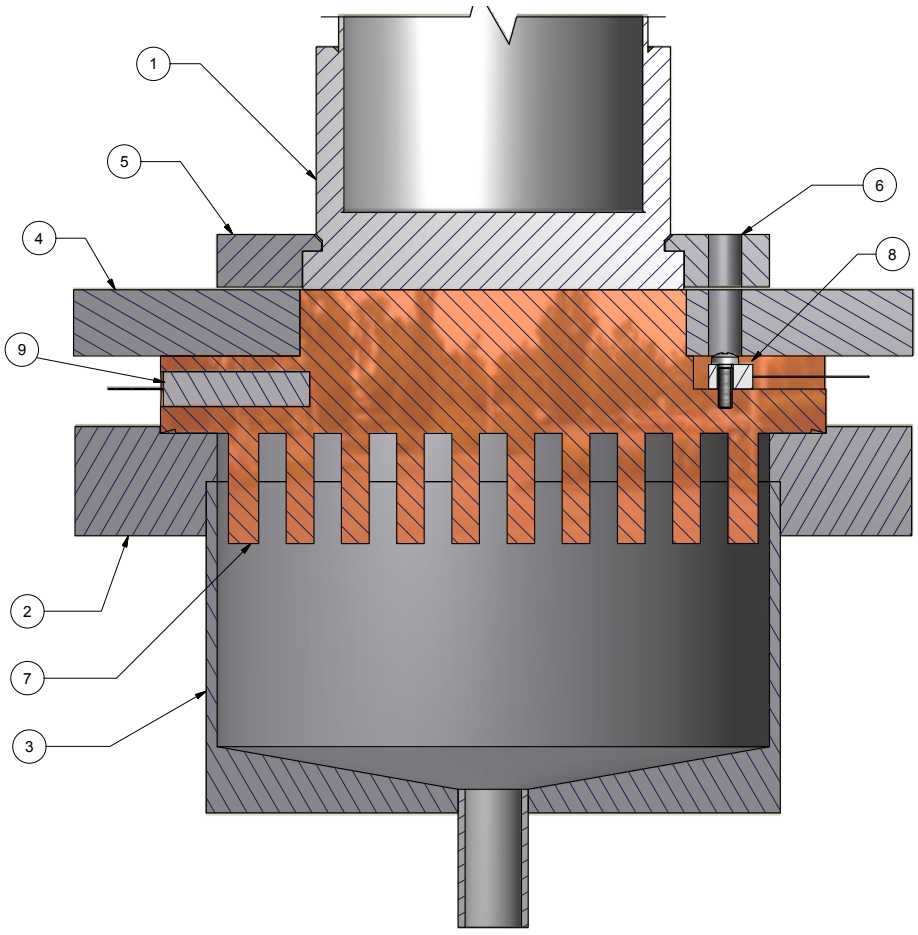

Figure A.1.: *Sectional view of the cooling tower CAD drawing allowing a close look to the individual parts described in chapter 5. The main parts, except for the spiral gas inlet tube, are visible: 1. cryocooler, 2. CF100 weld in flange, 3. cryostat with integrated funnel, 4. top flange, 5.&6. cryocooler holding clamps (6. with an extra hole to screw the diode), 7. cold finger, 8. Si-diode, 9. heater cartridge. Drawing made by C. Huhmann (WWU Münster).*

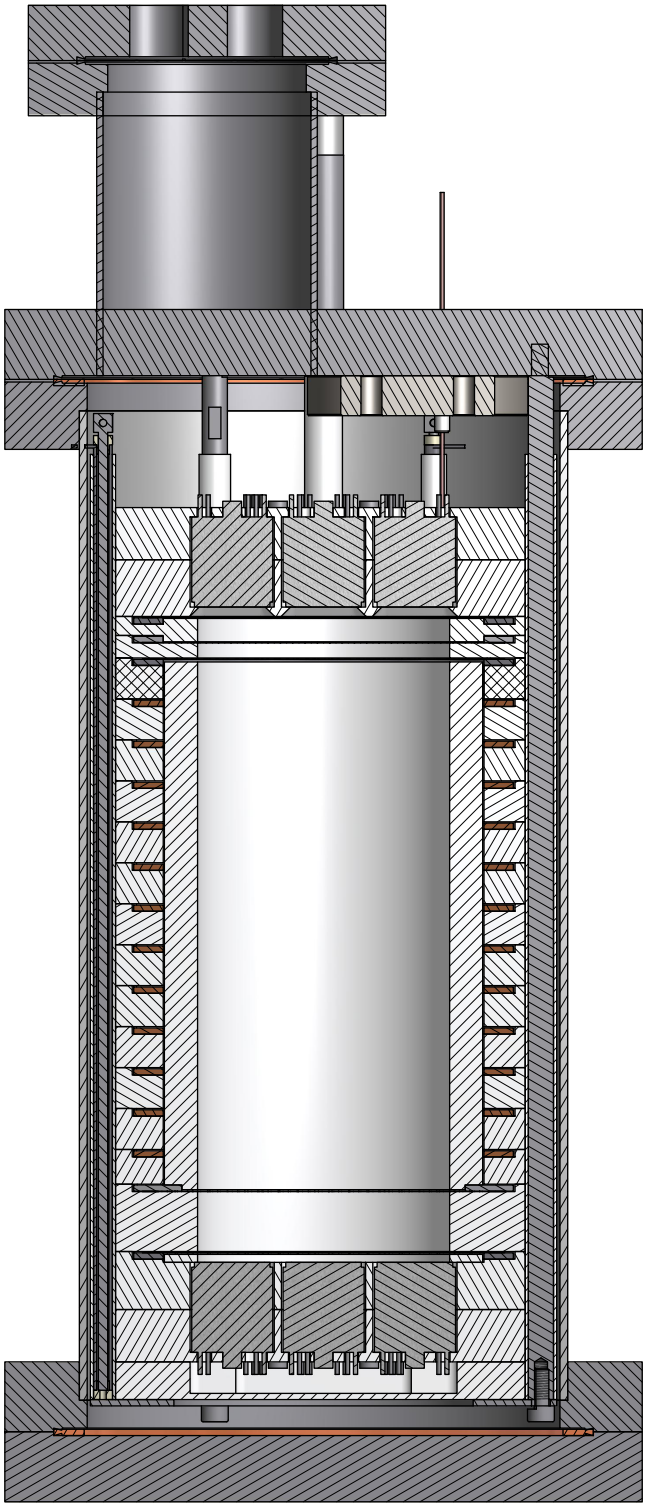

Figure A.2.: *Sectional view of the technical drawing which shows the TPC housed in the LXe cryostat as described in chapter 4.*

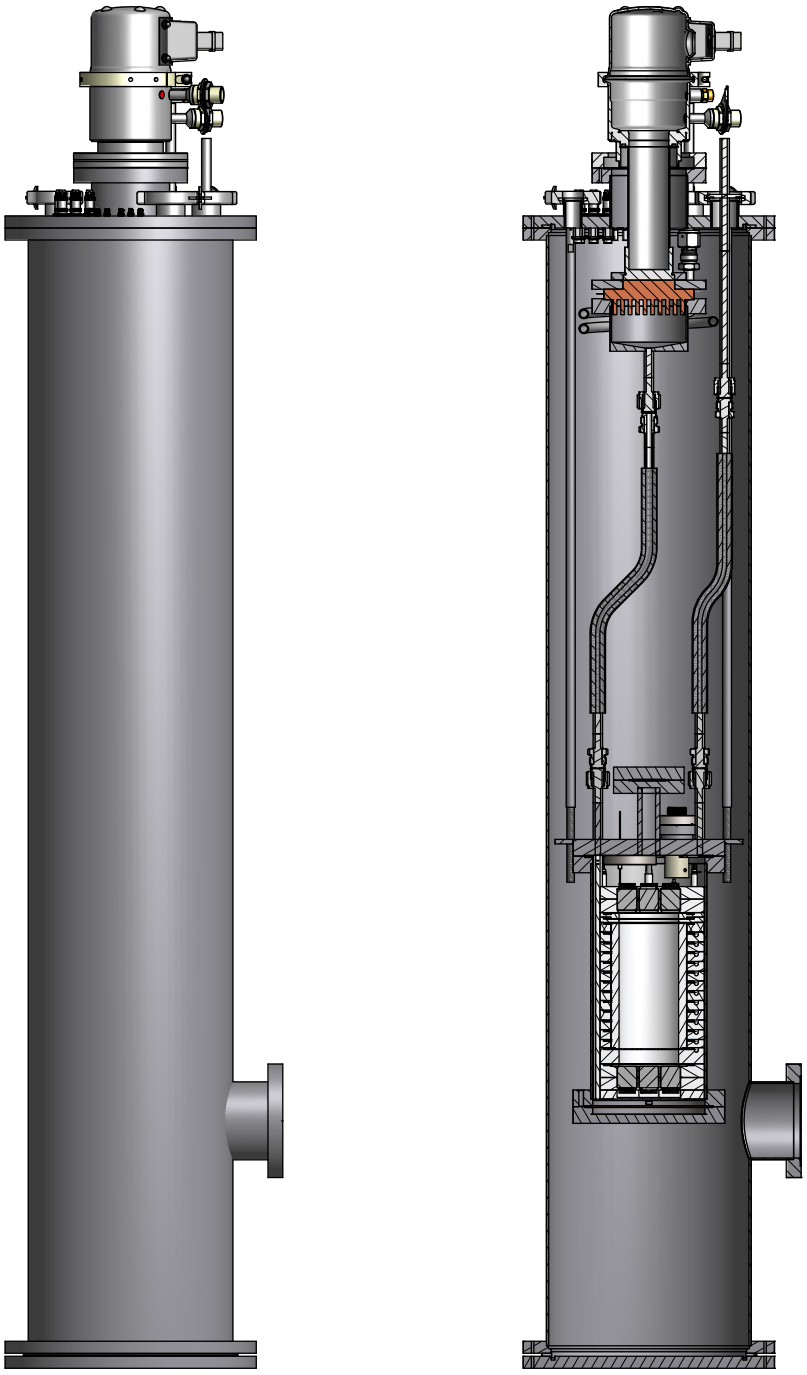

Figure A.3.: *Mechanical drawing of the TPC mounted in the vacuum cryostat. On the left hand side of the figure, the basic setup as it looks like in the XENON lab is shown. On the right hand side, the inner parts of the vacuum cryostat are shown and how they are installed as discussed in chapter 5. Also visible is the CF100 vacuum pump port on the vacuum vessel. Drawing made in cooperation with C. Huhmann (WWU Münster).*

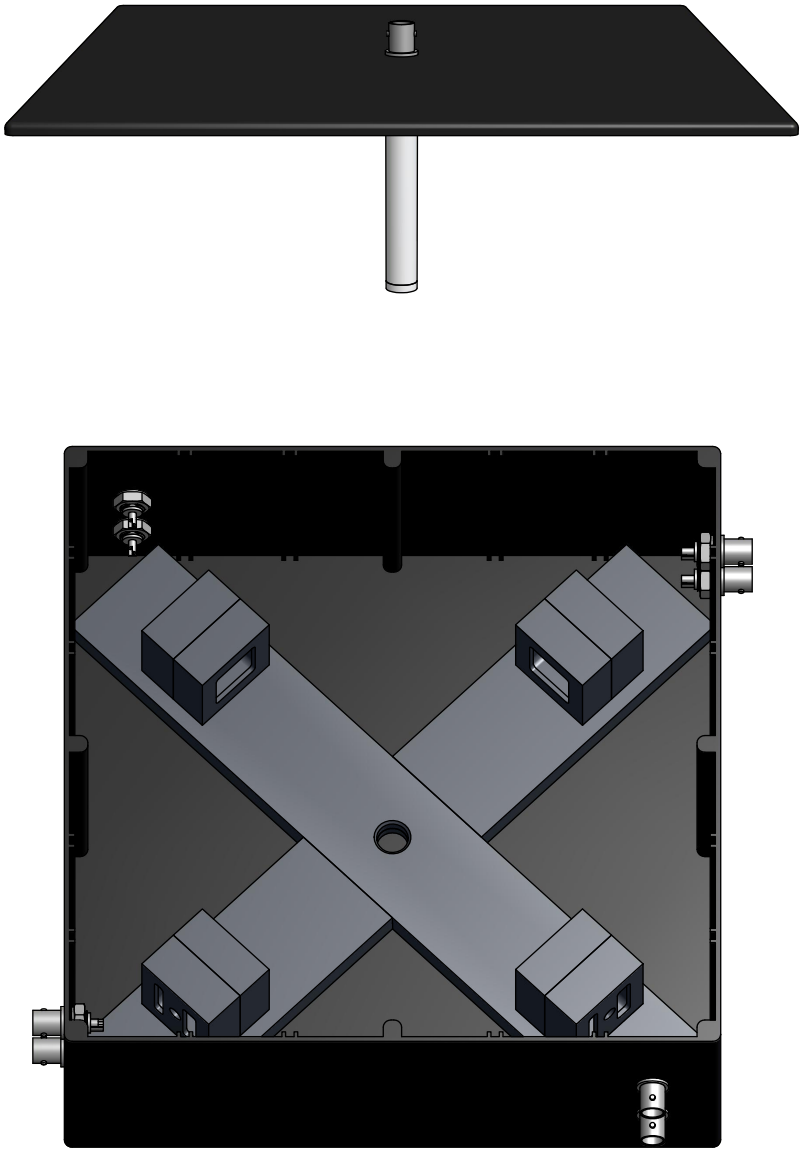

Figure A.4.: *Dark box for PMT calibration measurements (see chapter 6). The box is light-tight due to a neoprene sealing. Internal reflections are reduced by a black powder coating. Four PMTs can be fixed inside the box in special holders, guaranteeing an unitary distance to the LED which sits in the center of the box. The LED is mounted on the lid of the box with a Teflon tube around it which acts as a light diffusor. All electrical contacts are provided individually for each PMT by light-tight feedthroughs.*

List of Figures

List of Tables

Bibliography

[Ahm10] Z. Ahmed et al., Dark Matter Search Results from the CDMS II Experiment, Science 327, 1619, (2010)

[Ang11] G. Angloher et al., Results from 730 kg days of the CRESST-II Dark Matter Search, arXiv:1109.0702v1, (2011)

[Ang11] G. Angloher et al., Limits on WIMP dark matter using scintillating $CaWO_4$ cryogenic detectors with active background suppression, Astropart.Phys.23:325-339, arXiv:astro-ph/0408006v3, (2005)

[Apr09] E. Aprile and T. Doke, Liquid Xenon Detectors for Particle Physics and Astrophysics, Rev.Mod.Phys.82:2053-2097,2010, arXiv:0910.4956v1, (2009)

[Apr10] E. Aprile et al., XENON1T at LNGS, Technical Design Report, (2010)

[Apr11] E. Aprile et al., Dark Matter Results from 100 Live Days of XENON100 Data, Phys.Rev.D84:061101, arXiv:1104.2549v3, (2011)

[Bak76] G. Bakale, U. Sowada, and F. Schmidt, Effect of an Electric Field on Electron Attachment to SF_6, N_2O, and O_2 in Liquid Argon and Xenon, The Journal of Physical Chemistry, Vol. 80,No. 23, 7976, (1976)

[Ber10] R. Bernabei et al., New results from DAMA/LIBRA, Eur. Phys. J. C, 67: 39-49 arxiv:1002.1028v1, (2010)

[Ber08] R. Bernabei et al., The DAMA/LIBRA apparatus, Nucl. Instrum. Meth. A592:297-315, arxiv:0804.2738v1, (2008)

[Ber04] G. Bertone, D. Hooper, and J. Silk, Particle dark matter: evidence, candidates and constraints, FERMILAB-Pub-04/047-A, (2005)

[Bro10] E. Brown, PhD thesis
Search for Low Mass Dark Matter with the XENON100 Experiment and Simulations for 1 ton and 10 ton Dark Matter Detectors, University of California, Los Angeles, (2010)

[Buc11] O. Buchmueller et al., arXiv:1102.4585, (2011)

[Clo06] D. Clowe et al., A direct empirical proof of the existence of dark matter, Astrophys.J.648:L109-L113, (2006)

[CRC06] CRC Handbook of Chemistry and Physics, 87th ed, CRC Press, Boca Raton, FL, (2006)

[Eds97] J. Edsj, PhD thesis
Aspects of Neutrino Detection of Neutralino Dark Matter, Uppsala University, (1997)

[Ell83] J. Ellis and J.S. Hagelin, Supersymmetric Relics from the Big Bang*, Nuclear Physics, B238, 453-476, (1984)

[Gib11] K. Giboni et al., Xenon Recirculation-Purification with a Heat Exchanger, JINST 6 P03002, arXiv:1103.0986v1, (2011)

[Gru05] C. Grupen, Astroparticle Physics, Springer Verlag, (2005)

[Hae81] R. A. Haefer, Kryo-Vakuumtechnik, Springer, Berlin, Heidelberg, New York, (1981)

[Ham06] Photomultiplier Tubes, Basics and Applications, Hamamatsu Photonics K. K., (2006)

[Hel56] R. H. Helm, Inelastic and elastic scattering of 187-mev electrons from selected even-even nuclei, Phys. Rev., 104(5):14661475, (1956)

[Jar11] N. Jarosik et al., Seven-year wilkinson microwave anisotropy probe (WMAP*) observations: sky maps, systematic errors, and basic results, The Astrophysical Journal Supplement Series, 192:14 (15pp), (2011)

[Jun96] G. Jungman, M. Kamionkowski and K. Griest, Supersymmetric dark matter, Phys. Rept., 267:195373, (1996)

[Kol89] E. W. Kolb and M.S. Turner, The Early Universe, Addison-Wesley, Redwood City, (1989)

[Kom11] E. Komatsu et.al., Seven-Year Wilkinson Microwave Anisotropy Probe (WMAP) Observations: Cosmological Interpretation, ApJS, 192, 18, (2011)

[Kub78] S. Kubota, M. Hishida, and J.Ruan, J. Physics, Vol.11, 2645, (1978)

[Lew96] J. D. Lewin and P. F. Smith, Review of mathematics, numerical factors, and corrections for dark matter experiments based on elastic nuclear recoil, Astroparticle Physics, 6(1):87 112, (1996)

[NDS91] Nuclear Data Sheets 62, 271, (1991), National Nuclear Data Center, homepage www.nndc.bnl.gov

[NIST] National Institute of Standards and Technology, homepage www.nist.gov

[Ros11] S. Rosendahl, PhD thesis (in prep.) Institut für Kernphysik, Westfälische Wilhelms-Universität Münster, (2011)

[Tak75] T. Takahashi et al., Average energy expended per ion pair in liquid xenon*, 10.1103/PhysRevA.12.1771, (1975)

[Tro08] R. Trotta et al., J. High Energy Phys. 12, 024, (2008)

[Zwi37] F. Zwicky, Astrophys. J. 86, 217, (1937)

Eigenständigkeitserklärung

Ich versichere, dass ich diese Arbeit selbständig verfasst, keine anderen als die angegebenen Quellen und Hilfsmittel benutzt und Zitate kenntlich gemacht habe.

Münster, 21. Dezember 2011

Johannes Schulz

Danksagung

Ich möchte allen danken, ohne deren Unterstützung diese Arbeit nicht möglich gewesen wäre.

Mein großer Dank gilt Prof. Weinheimer, der mir trotz aller Hindernisse die Möglichkeit gegeben hat an diesem Projekt mitzuarbeiten. Ich habe während der Zeit in seiner Arbeitsgruppe unglaublich viel gelernt und mich fachlich weiter entwickelt.

A special thanks goes to Ethan Brown for all the time he spend with me, to explain stuff, to work in the Lab, to correct talks, and of course to correct this thesis.

Prof. Wessels danke ich vielmals für die Übernahme der Zweitkorrektur dieser Arbeit.

Ein großes Dankeschön auch an Christian Klein-Bösing, für die Korrektur meiner Arbeit.

Allen XENONlern danke ich für die tolle Atmosphäre in unserem Projekt. Cecilia, Christian H., Ethan, Hans, Karen und Stephan, ihr habt mir immer mit Rat und Tat zur Seite gestanden, wobei ich sagen kann, dass auch der Spaß nie zu kurz gekommen ist.

Natürlich danke ich auch allen anderen Mitgliedern der AG Weinheimer und des Instituts für Kernphysik, die immer für Fragen offen waren und auf fast alles eine Antwort wussten.

Besonders möchte ich hier den technischen Mitarbeitern des Instituts und den Mitgliedern der feinmechanischen Werkstatt und der Elektronikwerkstatt danken. Ohne euren Einsatz wäre diese Arbeit nicht möglich gewesen. Danke Christian, für all die Hilfe bei Zeichnungen und Laborarbeiten. Im Speziellen möchte ich noch Georg Bourichter, Daniel und Rainer danken, die mir viele technische Aspekte näher gebracht haben.

Trotz aller fachlichen Unterstützung wäre diese Arbeit niemals ohne die vielen tollen Menschen in meinem Leben möglich gewesen, denen ich hier danken möchte.

Hans und Rike danke ich für echte Freundschaft während des ganzen Studiums.
Furthermore I would like to thank Ethan and Cecilia for all the nice evenings together, the BBQ and the Italian cuisine.
Karen, Marcus und Adrijana, danke für die tolle Nachbarschaft!
Esco, Jonas, Tine, Nina, Anna, Sven, Martin, Vroni, Jenny, Tim. Danke für all die gemeinsamen Stunden und den Spaß den wir zusammen hatten, es tut gut mit euch befreudet zu sein. Esco, was mach ich bloß ohne dich?!
Söan und Alex, ihr seid die besten, danke!

Ich möchte außerdem allen danken, die mich in der besonders schweren Phase meines Lebens begeleitet haben.
Danke Detmar, danke Volker, dass ihr eine unerträgliche Zeit ein wenig erträglicher gemacht habt.

Zum Schluss möchte ich mich bei meiner Familie bedanken.
Jürgen und Manuela, Jürgen und Ulla, Irmi und Kevin, danke für all den Rückhalt.
Friederike, es ist großartig eine Schwester wie dich zu haben.
Omi, du bist die beste Großmutter der Welt.
Mama und Papa, danke für eure immerwährende Unterstützung und Liebe. Ihr habt all das möglich gemacht, ich bin euch unendlich dankbar.
Abschließend kann ich nur schwer ausdrücken wie froh und dankbar ich bin, dass es einen Menschen gibt, der jeden Tag für mich da ist, mich in schweren Zeiten aufmuntert, die schönen Momente mit mir genießt und immer hinter mir steht. Wir haben so viel erlebt! Danke, Jenni!